DISS. ETH NO. 25841

Data Assimilation in Computational Hemodynamics

A thesis submitted to attain the degree of

DOCTOR OF SCIENCES of ETH ZURICH

(Dr. sc. ETH Zurich)

presented by

TAHA SABRİ KOLTUKLUOĞLU

Dipl.-Inf. Univ., Technische Universität München

born on 12.07.1984

citizen of Germany

accepted on the recommendation of

Prof. Dr. Ralf Hiptmair, examiner

Prof. Dr. Patrick Jenny, co-examiner

Prof. Dr. Cristóbal Bertoglio, co-examiner

2019

Abstract

Analysis of hemodynamics shows great potential to provide indications for the risk of cardiac malformations and is essential for diagnostic purposes in clinical applications. Although medical imaging techniques such as phase-contrast magnetic resonance imaging (also known as 4D flow MRI) deliver useful information about the flow patterns in the lumen of large arteries, they cannot provide sufficient information at near-wall regions especially due to the noise in the observed signals, coarse resolution and partial volume effects.

As an alternative providing noise-free solution, computational fluid dynamics (CFD) has been established as a valuable tool for the detailed characterization of volumetric blood flow and its effects on the arterial wall. However, CFD requires awareness of boundary conditions and initial flow, which is usually not known beforehand. Besides, the flow is heavily influenced by the dynamic nature of the heart beat, which results in unsteady and periodic flow phenomena. This work aims to combine the superiority of CFD with the advantages of 4D flow MRI by introducing a novel approach for variational data assimilation and at the same time taking into account the dynamic nature of the heart beat.

Phase-contrast MRI is utilized for the prescription of the initial flow and boundary conditions. Due to the noisy nature of these observations, the velocity components are controlled at the boundaries through a mathematical optimization of flow patterns at the inlets. The adjustment is supported by the more reliable flow measurements in the middle of the lumen, where a least-squares flow-matching is considered. The norm of the control and the control surface gradient are augmented by Tikhonov regularization terms, which result (along with the flow-matching term) in the final objective function.

The minimization is performed under the constraint that the Navier-Stokes equations are satisfied. In addition, the time-periodic heart beat is captured by a set of harmonically balanced equations. The latter is achieved by a temporal discretization using a Fourier-spectral collocation approach, where the collocation points are aligned with 4D flow MRI measurements. Compared to the raw measurements, the proposed approach significantly improves the reconstructed flow field at the aortic root, which is one of the most important clinically relevant locations where flow disturbances can easily lead to pathological modifications of the arterial wall. Thus the new method has a great potential for revealing clinically relevant hemodynamic phenomena.

Zusammenfassung

Die Untersuchung der Hämodynamik könnte wichtige Hinweise über das Risiko des Entstehens von Herzfehlbildungen liefern. Gleichzeitig spielt es für diagnostische Zwecke eine wesentliche Rolle in klinischen Anwendungen. Medizinische Bildgebungstechniken wie die Phasenkontrast-Kernspintomographie (auch bekannt als 4D-Fluss-MRI) liefern nützliche Informationen über die Flussmuster im Lumen der Hauptschlagader. Aufgrund des Rauschens der beobachteten Signale, der groben Auflösung und der Teilvolumeneffekte, können die Bildgebungsverfahren jedoch keine ausreichende Informationen in wandnahen Bereichen bereitstellen.

Als Alternative für eine geräuschfreie Lösung hat sich die numerische Strömungsmechanik (english Computational Fluid Dynamics, CFD) als eine wertvolle Technik etabiliert, die für die detaillierte Charakterisierung des volumetrischen Blutflusses und seiner Auswirkungen auf die Arterienwand eine wichtige Rolle spielt. Jedoch erfordert CFD das Wissen über die Randbedingungen und des anfänglichen Volumenstroms, die in den meisten Fällen nicht vorhanden sind. Desweiteren wird der Fluss stark durch die dynamische Natur des Herzschlags beeinflusst, was zu instationären und periodischen Flussphänomenen führt. Das Ziel dieser Arbeit besteht darin, die Überlegenheit von CFD mit den Vorteilen der 4D-Fluss-MRT zu kombinieren, indem ein neuer Ansatz für die Anpassung von Variationsdaten vorgestellt und gleichzeitig die dynamische Natur des Herzschlags berücksichtigt wird.

Die Phasenkontrast-Kernspintomographie Bilder werden verwendet um die Anfangsströmung und die Randbedingungen vorzuschreiben. Aufgrund dessen, dass diese Beobachtungen verrauscht sind, werden die Geschwindigkeitskomponenten an den Einlässen so angepasst, dass die Strömungsmuster gesteuert und mathematisch optimiert werden. Die Assimilierung wird durch zuverlässigere Flussmessungen in der Mitte des Lumens unterstützt, wobei eine Flussanpassung unter der Berücksichtigung der kleinsten Quadrate angestrebt wird. Die Norm der Kontrolle und der Kontrolloberflächengradient werden durch Tikhonov-Regularisierungsterme ergänzt, welche (zusammen mit dem Flussanpassungsterm) die endgültige Zielfunktion liefern.

Die Minimierung wird unter der Nebenbedingung durchgeführt, dass die Navier-Stokes-Gleichungen erfüllt sind. Zusätzlich wird der zeitlich-periodische Herzschlag von einer Reihe harmonisch ausgeglichener Gleichungen erfasst. Letzteres wird durch eine zeitliche Diskretisierung unter Verwendung eines Fourier-Spektral-Kollokationsansatzes erreicht, bei dem die Kollokationspunkte mit 4D-Fluss-MRI-Messungen registriert sind. Verglichen mit den Rohmessungen, wird durch den vorgeschlagenen Ansatz eine erhebliche Verbesserung des rekonstrukturierten Flussfeldes an der Aortenwurzel erreicht. Dies ist einer der wichtigsten klinisch

relevanten Stellen, an denen Flussstörungen leicht zu pathologischen Veränderungen der Arterienwand führen können. Somit bietet die neue Methode ein mächtiges Potenzial, um klinisch relevante hämodynamische Phänomene aufzudecken.

Contents

1 Clinical Motivation

1.1 Impact of Cardiovascular Flow on Endothelium

The cardiovascular system, consisting of the heart connected with a network of blood vessels, is a mechanism which circulates the blood in the network. The heart is made of a specific tissue, which allows it to act like a pump and triggers the circulation of blood flow in the network of vessels. The main purpose of this mechanism is to provide necessary nutrients to the cells and organs of the body by delivering the oxygenated blood. In addition, unnecessary waste materials are carried away during the circulation process.

The arterial walls of the blood vessels are made up of three layers of tissue denoted as tunica intima, tunica media and tunica externa. The innermost layer, tunica intima, consists of endothelial cells and internal elastic membrane. The endothelial cells form an interior surface to the blood vessels, which is referred to as the endothelium, and have several critical functions [Mic03]. The endothelium imitates a barrier interface between the circulating blood in the lumen and the soft muscle tissue in the middle layer of the arterial walls. The endothelial cells control the exchange of substances into and out of the blood flow.

The heart periodically pumps blood into the aorta with a high velocity and the blood flow induces frictional forces at the arterial walls. The endothelial cells are constantly exposed to these frictional forces, which cause internal stresses on the endothelium. These internal stresses are conventionally known as the wall shear stresses (WSSs). Over time, the frictional forces experience alterations which might be caused by many factors. The build-up of fatty material due to high cholesterol levels, the presence of toxic substances related to smoking, hyperglycemia caused by the lack of physical activity or an underlying condition and hypertension caused by stress or another underlying condition just to name a few of these important factors, which lead to such potential alterations. As a result of this, the endothelial surface undergoes unusual deformations, either in the direction of blood flow or in any direction, depending on the severity of the present conditions and on the alterations in the frictional forces. This causes alterations of endothelial cell functions potentially resulting in endothelial dysfunction. The latter is an indication for vascular diseases such as atherosclerosis, thrombosis, hypertension, inflammatory diseases and aneurysm.

1.2 Importance of Wall Shear Stresses

WSSs in arterial vessels have long been hypothesised to play a major role in the onset and progress of endothelial disorders. The dependence of endothelial cell function under different flow conditions and the impact of WSSs in the development of atherosclerosis have been described in earlier studies [Tex65; Ku85; Zar87; Zan91; Wal93; Mal99]. A brief review of the underlying hypotheses for hemodynamic theories of atherogenesis was given by Gessner [Ges73]. More recent studies have explored the processes at the molecular, cellular and vascular levels, and supported the role of low WSSs in the generation of coronary atherosclerosis and vascular remodelling [Cha07; Chi11]. The effects of hemodynamic forces were discussed by Yoshida *et al.* [Yos90] considering the differences in the biological fine structures of arterial walls in the human aorta and the endothelial morphology at bifurcations in rabbit aorta. Moreover, characterization of blood flow near the aortic wall plays an important role in the diagnosis of aortic aneurysms and their risk of rupture [Vor96; Vor05].

1.3 Imaging Modalities for Assesment of Wall Shear Stresses

Due to the reasons provided in the previous sections, the evaluation of shear stresses over the arterial wall has attracted increasing interest in the cardiovascular research field. For this purpose, different computational strategies have been developed to either simulate or reconstruct blood flow. A basic approach to this problem consists of using anatomical data extracted from medical images to construct patient-specific vascular models and to perform computational fluid dynamic (CFD) simulations of blood flow in these geometric models. The major drawback in such approaches lies in the lack of flow data to correctly set up boundary conditions (BCs) for the isolated arterial districts of interest. Rapidly, the patient-specificity is lost when using generic criteria to prescribe such BCs in CFD simulations.

A further step relies on using advanced image acquisition techniques in an attempt to retrieve flow field measurements and merge them into the CFD simulations, thus providing more accurate patient-specific predictions. In this context, different methods exist to reconstruct the velocity field in a certain region of interest. Several works have been reported that address this problem using particle image velocimetry (PIV), ultrasound and 4-D phase-contrast magnetic resonance imaging (4-D flow MRI). A comprehensive review of several methods for flow reconstruction and the assessment of WSSs is presented by Katritsis *et al.* [Kat07].

The use of PIV is known to be limited to in-vitro studies and cannot be applied to the study of blood flow in in-vivo conditions [Hoc04]. On the other hand, ultrasound imaging allows the extraction of 2-D information, thus requiring a 3-D flow reconstruction process, which is prone to inaccuracy in view of the incomplete nature of the data. Another limitation of ultrasound is that the WSSs can only be estimated with acceptable accuracy in relatively straight arteries [Ren06]. Conversely, 4-D flow MRI offers the advantage of three-directional

blood flow quantification with three-dimensional spatial encoding. Image reconstruction from the MRI data acquisition yields 3-D *CINE* (time-resolved) magnitude images representing the anatomical data and three phase difference images representing the velocity data corresponding to the components of the 3-D velocity field. Moreover, MRI can be used in in-vivo scenarios noninvasively. Recent advances in MRI have revealed great diagnostic potential in hemodynamics applications [Mar12; Kol16]. Nevertheless, 4-D flow MRI also suffers from important limitations for the accurate quantification of blood flow in regions close to the arterial walls (near-wall regions), which is of the utmost importance for patient-specific estimation of the WSS field. Due to the limited image resolution, the acquired signals within the voxels at boundaries are obtained partially by the moving spins in the flowing blood and partially by the steady behavior of the arterial tissue. This artifact is known as the partial-volume-effect [Tha95; Sha00; Bou18].

1.4 Motivation and Summary of Present Research Work

Oscillatory behaviour or elevated levels of wall shear stresses are factors of great significance in the onset and development of a range of cardiovascular diseases. Unphysiological WSSs are inconsistent or not compatible with normal functioning of the endothelial cells and trigger serious diseases such as inflammation or atherosclerosis. This finally threatens the integrity of the elastic lamina, which is responsible for maintaining the stability of the vessel wall. One of the aftereffects is vessel dilatation, potentially followed by rupture with fatal consequences.

In the presence of ascending aortic aneurysms, decisions for a potential surgery are made depending on the aortic dimensions and diameter of the aneurysm. However, catastrophic events such as aortic dissection or rupture can actually occur at any stage of the diameter. Hence, in the interest of improving early diagnosis and the accuracy of interventional decision making, additional factors (other than the diameter alone) need to be determined. For this purpose, it is extremely important to understand the fluid dynamics and WSSs in the ascending aorta and at the aortic root. Apart from the laboratory markers, diagnostic imaging tools have become essential for probing local changes of morphology and function during all stages of the disease. While a number of important parameters can be quantified using these techniques, a range of key parameters including WSSs are difficult to assess based on the spatial resolution that can be obtained in a clinical setting. Owing to such limitations, it has been necessary to investigate alternative approaches such as computational methods of fluid dynamics.

When performing CFD simulations of blood flow, correct definition of the flow problem requires knowledge of the initial conditions and BCs, as well as the flow properties, i.e. blood density and blood viscosity. However, due to the limitations of the aforementioned imaging techniques, in particular the BCs are usually not available or cannot be measured accurately. Especially, the problem of a correct assessment of the BCs for such inadequate and crude data has been the point of attention for a long time. Several studies have been reported on

the effects of idealised versus measured inflow BCs for patient-specific simulations of carotid bifurcation or human aorta [Cam12; Mor13]. Additionally, a sensitivity analysis with respect to different BCs was reported by Cito *et al.* [Cit14]. Furthermore, a recent report provided by Pirola *et al.* [Pir17] discussed the importance of the choice of BCs on the final results.

As a result of the aforementioned advantages and limitations of current imaging technologies, 4-D flow MRI procedures have been frequently considered (and mostly preferred) towards the improvement of patient-specific CFD simulations. Classical CFD methods (supported by MRI) usually apply fixed BCs at the inlet of the arterial domain based on the noisy measurements extracted from the 4-D flow MRI data [Har13; Pir17]. This is why recent studies have concentrated on optimal control strategies to alter BCs in such a way that the flow in the lumen matches the observations according to certain criteria. Optimal control supported by observations has been referred to as data assimilation (DA). Such studies were first and mainly applied in meteorology, physical oceanography and atmospheric flows [Cou91; Ide97]. Due to the shortcomings in the classical CFD approach (employing noisy data as BCs), DA has received increased attention in the cardiovascular research field over the last decade.

Optimal control studies rely on adjoint equations for efficiently computing the state gradient with respect to the control. The adjoint equations are differential equations requiring the availability of state variables from the original (direct) problem. This makes it to a challenge, especially for time-dependent problems. In such a case, the adjoint equations posses a backward-in-time nature, thus, they usually need to be solved following a path starting from the last time and ending at the initial time of the considered problem. At the same time, solutions of the direct state variables at each infinitesimal time step are required. Hence, in order to solve for the adjoint state variables, all the trajectories of the direct state variables must be solved and stored in the memory. This process also needs to be repeated as many times as the number of iterations required by the optimisation algorithm to arrive at the optimum state. Hence, due to enormous memory requirements and the excessive computational burden in the case of large convection dominated flow problems, conventional DA studies are currently limited to steady-state cases.

In the present work, a novel approach is proposed for transient data assimilation in computational hemodynamics following the variational formulation. In contrast to currently existing DA studies, the proposed method relies on a harmonic balance strategy by employing Fourier-spectral collocation method to perform dynamic data assimilation. This work enables accurate characterisation of the dynamic flow field in quite feasible wall clock times, which are otherwise difficult or impossible to achieve using currently available DA strategies relying on traditional time-stepping schemes. In addition, the work addresses the limited resolution of MR velocity encoding in shear layers and aims to interlace 4D flow MRI with CFD to enable accurate quantification of WSSs. Compared to the raw measurements, the proposed approach significantly improves the reconstructed flow field at the aortic root, which is one of the most important clinically relevant locations where flow disturbances can easily lead to pathological

modifications of the arterial wall. Thus the new method has a great potential for revealing clinically relevant hemodynamic phenomena.

2 Boundary Control in Computational Hemodynamics

Parts of this chapter have been published in the Journal of Fluid Mechanics (2018) by Koltukluoğlu and Blanco [Kol18].

Abstract

In this work, an adjoint-based variational data assimilation method is proposed following an optimise-then-discretise approach, and is applied in the context of computational hemodynamics. The methodology aims to make use of phase-contrast magnetic resonance imaging to perform optimal flow control in computational fluid dynamic simulations. Flow matching between observations and model predictions is performed in luminal regions, excluding near-wall areas, improving the near-wall flow reconstruction to enhance the estimation of related quantities such as wall shear stresses. The proposed approach significantly improves the flow field at the aortic root and reveals a great potential for predicting clinically relevant hemodynamic phenomenology. This work presents model validation against an analytical solution using the standard 3-D Hagen-Poiseuille flow, and validation with real data involving the flow control problem in a glass replica of a human aorta imaged with a 3T magnetic resonance scanner. In vitro experiments consist of both a numerically generated reference flow solution, which is considered as the ground truth, as well as real flow MRI data obtained from phase-contrast flow acquisitions. The validation against the in vitro flow MRI experiments is performed for different flow regimes and model parameters including different mesh refinements.

2.1 Introduction

Data assimilation procedures in hemodynamics were anticipated a decade ago for the prescription of flow rates in rigid and compliant domains [For08; For10]. Additional preliminary results of DA in tubular structures were reported by D'Elia *et al.* [DEl10b] based on 2-D Stokes flow simulations. The convergence rate and noise sensitivity were investigated based on artificially generated noisy data. In D'Elia *et al.* [DEl10a], their work was extended to the Oseen problem. This strategy was employed in combination with a fixed point method to solve the Navier-Stokes equations and to perform flow matching in synthetically generated datasets using different mesh refinements. In a further study, these authors extended their tests to

an axis-symmetric cylinder and a 2-D geometry resembling a carotid artery [DEl12b]. These studies were based on a discretise-then-optimise (DO) approach, where the equations are first discretised and the optimisation is performed thereafter. Numerical results were mostly based on 2-D simplified geometries or on problems with rotational symmetry. These works were some of the first attempts to perform DA in blood flow simulations. However, real flow MRI measurements were not available in these studies.

In a recent work, DA was performed using more realistic vascular geometries [Tia16]. First, a comparison between Dirichlet and Neumann boundary control was reported with the validation based on an idealised 2-D geometry with known solution. Second, numerical results were presented using a realistic 3-D geometry of a saccular brain aneurysm. The application of velocity control (Dirichlet BC) was claimed to recover the flow field better than the application of pressure control (Neumann BC). However, the flow data were synthetic and experiments with real 4-D flow MRI measurements were not available. Furthermore, they also applied the DO approach as a solution strategy. In Collis *et al.* [Col02], however, the authors concluded that the optimise-then-discretise (OD) approach (where the mathematical optimisation is first performed at the continuum level and the resulting set of equations are then discretised thereafter) has better asymptotic convergence properties and leads to better adjoint approximations.

In general, data assimilation methods can be divided into two categories being the sequential methods and the variational formulations. Some overviews about the different assimilation methods in computational hemodynamics have been provided by D'Elia *et al.* [DEl10b] and Chapelle *et al.* [Cha13]. The sequential methods are based on statistical estimates mostly relying on Kalman filtering for linear problems [Bel14]. In the recent decades, generalisations to Kalman filtering have been developed (and applied in computational hemodynamics for nonlinear problems), which are also known as the extended or unscented Kalman filter [Fri10; Hu12; Cin15; Pan17; Lal17]. In contrast, the variational data assimilation methods can be considered as inverse problems including an objective function, which needs to be minimised under the constraints that some partial differential equations (in this case the Navier-Stokes equations) are satisfied. To establish this, the gradient of the objective function with respect to control has to be evaluated. This can be usually achieved by two different approaches which are known as either the sensitivity-based or adjoint-based methods. In the sensitivity based approach, the gradient of the objective function is evaluated by the application of finite differences with the aim to compute the derivative with respect to each single component of the control. In such a case, small perturbations are performed on each component of the control and the forward solution is computed for each of these perturbations [Gun02]. This is a very time consuming process and, hence, is usually not applied in practical studies. The adjoint-based methods rely on a backwards solution of the so-called adjoint equations which are a consequence of optimality conditions [DEl12b; DEl12a; Gue14; Tia16]. In adjoint-based methods, the solution of the forward problem is incorporated into the adjoint-equations. As

a result of this, there is no longer need for computations of as many forward solutions as the number of control parameters.

In this work, we propose an adjoint-based variational data assimilation method for 3-D steady state blood flow simulations following the OD approach and using true data acquisitions from 4-D flow MRI. The optimisation procedure is driven by the gradient of a given cost functional, computed within a variational framework. A Lagrangian method is employed for the calculation of the sensitivities from which the adjoint problem is derived. Further, the proposed approach considers cost functionals in the flow-matching formulation including the inlet and outlet boundaries (in addition to flow-matching in the volume of the domain). While previous studies mostly count on validations with known numerical solutions in simplified 2-D geometries, in this work we perform 3-D validation studies relying on both an analytical solution based on the Hagen-Poiseuille flow and a numerical solution generated using the physical phantom aorta. We also present a sensitivity analysis with respect to changes in the optimisation parameters. Considering the noisy nature of 4-D flow MRI measurements, a universal outlier detection scheme is applied prior to the mapping of the flow field in the computational domain. Besides, a projection onto divergence-free space is employed to recover back the solenoidal property of the measured flow field. An additional sensitivity analysis with respect to changes in the flow-matching domain is developed, which is important in determining the region-of-interest for the DA procedure. The optimisation solver was tested for different initial flow guesses demonstrating the sensitivity in the numerical results. Finally, the boundary flow control formulation and the preprocessing pipeline are combined to reconstruct the flow field in near-wall regions in a glass replica of the human aorta. For the latter, the methodology was tested for different flow regimes characterised by Reynolds numbers (Re) up to 2100, and mesh analysis was performed with different numbers of cells. The proposed strategy remarkably improves the flow field at the aortic root and reveals a great potential for predicting clinically relevant hemodynamic phenomenology.

2.2 Mathematical Formulation

2.2.1 Optimisation Problem

Let us define a bounded Lipschitz domain $\Omega \subset \mathbb{R}^3$ along with its boundary $\partial\Omega = \Gamma_i \cup \Gamma_o \cup \Gamma_w$, where $\Gamma_i, \Gamma_o, \Gamma_w \subset \mathbb{R}^3$ stand for the inlet, outlet and arterial wall boundaries respectively. Figure 2.1(a) illustrates such a domain resembling an aortic vascular geometry (to be used later in section 2.5). We further define a contracted subdomain $\Omega_s \subset \Omega$ with boundary $\partial\Omega_s = \Gamma_{si} \cup \Gamma_{so} \cup \Gamma_{sw}$, where $\Gamma_{si} \subset \Gamma_i$ and $\Gamma_{so} \subset \Gamma_o$ (see figure 2.1(b)). The incompressible steady flow of a Newtonian fluid is considered in Ω. The inflow at Γ_i is prescribed by the function $\boldsymbol{g} = \boldsymbol{g}(\boldsymbol{x}) : \Gamma_i \to \mathbb{R}^3$, whereas the density and dynamic viscosity of the fluid are represented by ρ and μ respectively. At the outflow, Γ_o, a traction free boundary (i.e. a

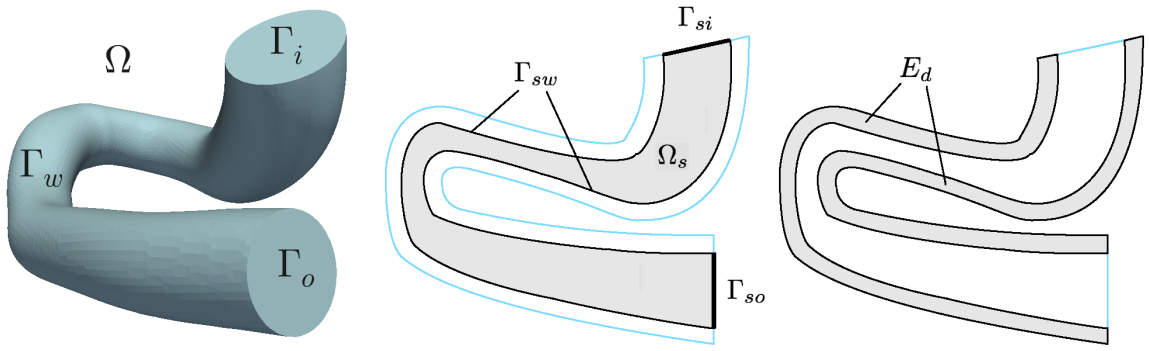

(a) (b) (c)

Figure 2.1: Computational domain. (a): Ω along with boundaries Γ_i : Inlet, Γ_o : Outlet and Γ_w : Wall. (b): Flow-matching domain $\Omega_s \subset \Omega$ with boundaries $\partial\Omega_s = \Gamma_{si} \cup \Gamma_{so} \cup \Gamma_{sw}$, which is at a distance s (mm) from Γ_w. (c): Error measurement domain E_d, which is within d (mm) distance from Γ_w.

homogeneous Neumann BC) is considered. This hypothesis is exact when the flow is fully developed, and it is physiologically reasonable in the present context. We highlight the fact that the function $\boldsymbol{g}$ is such that $\boldsymbol{g}|_{\gamma_i} = 0$, where γ_i is the boundary of surface Γ_i. In what follows, $L^2(\Omega)$ stands for the space of square integrable scalar functions in Ω, while $\boldsymbol{H}^1(\Omega)$ is the space of square integrable vector functions whose first derivatives are also square integrable functions in Ω. The blood flow velocity, $\boldsymbol{u} \in \boldsymbol{\mathcal{U}}^*$, with

$$\boldsymbol{\mathcal{U}}^* = \left\{ \boldsymbol{v} \in \boldsymbol{H}^1(\Omega) \mid \operatorname{div} \boldsymbol{v} = 0,\ \boldsymbol{v}|_{\Gamma_w} = \boldsymbol{0},\ \boldsymbol{v}|_{\Gamma_i} = \boldsymbol{g} \right\} \quad , \tag{2.2.1}$$

is solution of the steady state Navier-Stokes equations, which are written in variational form as follows:

$$\text{Find } \boldsymbol{u} \in \boldsymbol{\mathcal{U}}^* \text{ such that, } \int_\Omega \left[\rho(\nabla \boldsymbol{u})\boldsymbol{u} \cdot \hat{\boldsymbol{u}} + 2\mu \nabla^s \boldsymbol{u} \cdot \nabla^s \hat{\boldsymbol{u}} \right] d\Omega = 0 \quad \forall\, \hat{\boldsymbol{u}} \in \widehat{\boldsymbol{\mathcal{U}}}^* \quad , \tag{2.2.2}$$

where the strain rate tensor is defined as $\nabla^s(\cdot) = [\nabla(\cdot) + (\nabla(\cdot))^T]/2$, and

$$\widehat{\boldsymbol{\mathcal{U}}}^* = \left\{ \hat{\boldsymbol{v}} \in \boldsymbol{H}^1(\Omega) \mid \operatorname{div} \hat{\boldsymbol{v}} = 0,\ \hat{\boldsymbol{v}}|_{\Gamma_w} = \boldsymbol{0},\ \hat{\boldsymbol{v}}|_{\Gamma_i} = \boldsymbol{0} \right\} \quad . \tag{2.2.3}$$

The constraints $\operatorname{div} \boldsymbol{u} = 0$ and $\boldsymbol{u}|_{\Gamma_i} = \boldsymbol{g}$ can be relaxed using Lagrange multipliers p and $\boldsymbol{r}$. Further, we introduce the space $\boldsymbol{\mathcal{U}} = \left\{ \boldsymbol{v} \in \boldsymbol{H}^1(\Omega) \mid \boldsymbol{v}|_{\Gamma_w} = \boldsymbol{0} \right\}$ and the space $\boldsymbol{H}^{-\frac{1}{2}}(\Gamma_i)$, which is the dual space of $\boldsymbol{H}^{\frac{1}{2}}_{00}(\Gamma_i) = \left\{ \boldsymbol{g} \in \boldsymbol{H}^{\frac{1}{2}}(\Gamma_i) \mid \boldsymbol{g}|_{\gamma_i} = 0 \right\}$ (in the sense given by the pairing $\langle \mathbf{r}, \mathbf{u} \rangle_{\boldsymbol{H}^{-\frac{1}{2}}(\Gamma_i) \times \boldsymbol{H}^{\frac{1}{2}}(\Gamma_i)} = \int_{\Gamma_i} \boldsymbol{r} \cdot \boldsymbol{u}\, d\Gamma$). The problem (2.2.2) now becomes

$$\begin{aligned} &\mathscr{P}_\Omega : \text{find } (\boldsymbol{u}, p, \boldsymbol{r}) \in \boldsymbol{\mathcal{U}} \times L^2(\Omega) \times \boldsymbol{H}^{-\frac{1}{2}}(\Gamma_i), \text{ such that} \\ &\int_\Omega \left[\rho(\nabla \boldsymbol{u})\boldsymbol{u} \cdot \hat{\boldsymbol{u}} + 2\mu \nabla^s \boldsymbol{u} \cdot \nabla^s \hat{\boldsymbol{u}} - p \operatorname{div} \hat{\boldsymbol{u}} - \hat{p} \operatorname{div} \boldsymbol{u} \right] d\Omega \end{aligned} \tag{2.2.4}$$

$$= \int_{\Gamma_i} \hat{\boldsymbol{r}} \cdot (\boldsymbol{u} - \boldsymbol{g})\, d\Gamma + \int_{\Gamma_i} (\boldsymbol{r} \cdot \hat{\boldsymbol{u}})\, d\Gamma \quad \forall\, (\hat{\boldsymbol{u}}, \hat{p}, \hat{\boldsymbol{r}}) \in \boldsymbol{\mathcal{U}} \times L^2(\Omega) \times \boldsymbol{H}^{-\frac{1}{2}}(\Gamma_i) \ .$$

For the control flow problem, assume that some observations $\tilde{\boldsymbol{u}}^t \in \Omega$ are available. We want to find a velocity field $\boldsymbol{u}$, such that it better matches the observations and, at the same time, is constrained to be a solution of Problem $\mathscr{P}_\Omega$. In what follows, $\nabla_{\boldsymbol{\tau}}$ denotes the surface gradient, whereas β and β_1 are arbitrary parameters for a Tikhonov regularization, and α is a positive real number. The parameters α, β and β_1 will often be denoted as optimisation parameters. Based on a user-defined cost function, $\mathscr{O}$, the aforementioned flow-matching problem can be cast as a mathematical optimisation problem, which reads

$$\begin{aligned}
&\mathscr{P}_M: \text{ Find } \boldsymbol{g} \text{ which minimises } \mathscr{O}(\boldsymbol{g}) = \mathscr{O}^*(\boldsymbol{u}(\boldsymbol{g}), \boldsymbol{g}, \tilde{\boldsymbol{u}}^t) \text{ such that } \mathscr{P}_\Omega \text{ holds, where} \\
&\mathscr{O}(\boldsymbol{g}) = \frac{\alpha}{2}\left(\int_{\Omega_s} |\boldsymbol{u}(\boldsymbol{g}) - \tilde{\boldsymbol{u}}^t|^2\, d\Omega + \int_{\Gamma_{si}} |\boldsymbol{u}(\boldsymbol{g}) - \tilde{\boldsymbol{u}}^t|^2\, d\Gamma + \int_{\Gamma_{so}} |\boldsymbol{u}(\boldsymbol{g}) - \tilde{\boldsymbol{u}}^t|^2\, d\Gamma\right) + \\
&\quad + \frac{\beta}{2}\int_{\Gamma_i} |\boldsymbol{g}|^2\, d\Gamma + \frac{\beta_1}{2}\int_{\Gamma_i} |\nabla_{\boldsymbol{\tau}}\, \boldsymbol{g}|^2\, d\Gamma \ .
\end{aligned} \tag{2.2.5}$$

The flow-matching metric is defined on Ω_s, Γ_{si} and Γ_{so}, which are considered as the trust region of experimental observations (see figure 2.1(b)). The well-posedness of the problem $\mathscr{P}_M$ has been addressed by Guerra *et al.* [Gue15]. The user-defined cost function contains two types of terms, those to enforce the matching between the model prediction and the available observations, and those to deliver a regularized mathematical problem. Concerning (2.2.5), the first three terms are responsible for the flow matching, while the latter two terms provide a penalization for the control function not to grow unboundedly, and, at the same time, to force a certain regularity over the control. The choices of these terms were also motivated by Gunzburger *et al.* [Gun00].

2.2.2 Optimality Conditions

To obtain the necessary optimality conditions for the optimisation problem $\mathscr{P}_M$, and to avoid the calculation of the derivative of the velocity field with respect to the function $\boldsymbol{g}$, it is convenient to recast the problem of constrained optimisation as a saddle point problem. Correspondingly, we then construct the Lagrangian functional to relax the dependence of $\boldsymbol{u}$ on $\boldsymbol{g}$ as follows:

$$\begin{aligned}
\mathscr{L}(\boldsymbol{g}, \boldsymbol{u}, p, \boldsymbol{r}, \boldsymbol{\lambda_u}, \lambda_p, \boldsymbol{\lambda_r}) = \mathscr{O}^*(\boldsymbol{u}, \boldsymbol{g}, \tilde{\boldsymbol{u}}^t) - \int_{\Gamma_i} \boldsymbol{\lambda_r} \cdot (\boldsymbol{u} - \boldsymbol{g})\, d\Gamma - \int_{\Gamma_i} \boldsymbol{r} \cdot \boldsymbol{\lambda_u}\, d\Gamma \\
+ \int_\Omega \left[\rho(\nabla \boldsymbol{u})\boldsymbol{u} \cdot \boldsymbol{\lambda_u} + 2\mu \nabla^s \boldsymbol{u} \cdot \nabla^s \boldsymbol{\lambda_u} - p\, \mathrm{div}\, \boldsymbol{\lambda_u} - \lambda_p\, \mathrm{div}\, \boldsymbol{u}\right] d\Omega \ ,
\end{aligned} \tag{2.2.6}$$

with $(\boldsymbol{g}, \boldsymbol{u}, p, \boldsymbol{r}, \boldsymbol{\lambda_u}, \lambda_p, \boldsymbol{\lambda_r}) \in \boldsymbol{H}_0^1(\Gamma_i) \times \boldsymbol{\mathcal{U}} \times L^2(\Omega) \times \boldsymbol{H}^{-\frac{1}{2}}(\Gamma_i) \times \boldsymbol{\mathcal{U}} \times L^2(\Omega) \times \boldsymbol{H}^{-\frac{1}{2}}(\Gamma_i)$, where $\boldsymbol{H}_0^1(\Gamma_i)$ is the space of traces over Γ_i of $\boldsymbol{H}^1(\Omega)$ functions that are zero over γ_i, the boundary

of surface Γ_i. Further, let us consider the perturbations $\hat{(\cdot)}$ to the fields $(\cdot)$ above, as $(\cdot)+\tau\hat{(\cdot)}$ (where τ is a real number that aids in the calculation of the Gâteaux derivative but that is ultimately immaterial for the result), that is,

$$\boldsymbol{g} \to \boldsymbol{g} + \tau\hat{\boldsymbol{g}} \qquad \boldsymbol{g}, \hat{\boldsymbol{g}} \in \boldsymbol{H}_{00}^{\frac{1}{2}}(\Gamma_i) \ , \tag{2.2.7}$$

$$\boldsymbol{u} \to \boldsymbol{u} + \tau\hat{\boldsymbol{u}} \qquad \boldsymbol{u}, \hat{\boldsymbol{u}} \in \boldsymbol{\mathcal{U}} \ , \tag{2.2.8}$$

$$p \to p + \tau\hat{p} \qquad p, \hat{p} \in L^2(\Omega) \ , \tag{2.2.9}$$

$$\boldsymbol{r} \to \boldsymbol{r} + \tau\hat{\boldsymbol{r}} \qquad \boldsymbol{r}, \hat{\boldsymbol{r}} \in \boldsymbol{H}^{-\frac{1}{2}}(\Gamma_i) \ , \tag{2.2.10}$$

$$\boldsymbol{\lambda_u} \to \boldsymbol{\lambda_u} + \tau\hat{\boldsymbol{\lambda}}_{\boldsymbol{u}} \qquad \boldsymbol{\lambda_u}, \hat{\boldsymbol{\lambda}}_{\boldsymbol{u}} \in \boldsymbol{\mathcal{U}} \ , \tag{2.2.11}$$

$$\lambda_p \to \lambda_p + \tau\hat{\lambda}_p \qquad \lambda_p, \hat{\lambda}_p \in L^2(\Omega) \ , \tag{2.2.12}$$

$$\boldsymbol{\lambda_r} \to \boldsymbol{\lambda_r} + \tau\hat{\boldsymbol{\lambda}}_{\boldsymbol{r}} \qquad \boldsymbol{\lambda_r}, \hat{\boldsymbol{\lambda}}_{\boldsymbol{r}} \in \boldsymbol{H}^{-\frac{1}{2}}(\Gamma_i) \ . \tag{2.2.13}$$

The Gâteaux derivative of the Lagrangian functional is denoted as follows:

$$\left\langle \frac{\partial \mathscr{L}}{\partial a}, \hat{a} \right\rangle = \frac{d}{d\tau} \mathscr{L}(\ldots, a + \tau\hat{a}, \ldots)\Big|_{\tau=0} \ . \tag{2.2.14}$$

Our goal is to compute the Gâteaux derivative of $\mathscr{O}$ with respect to perturbation in $\boldsymbol{g}$,

$$\left\langle \frac{\partial \mathscr{O}}{\partial \boldsymbol{g}}, \hat{\boldsymbol{g}} \right\rangle = \frac{d}{d\tau} \mathscr{O}(\boldsymbol{g} + \tau\hat{\boldsymbol{g}})\Big|_{\tau=0} \ . \tag{2.2.15}$$

The critical points of the Lagrangian (2.2.6) contain information on the aforementioned Gâteaux derivative (2.2.15), and are characterised by the following variational equations

$$\left\langle \frac{\partial \mathscr{L}}{\partial(\boldsymbol{\lambda_u}, \boldsymbol{\lambda}_p, \boldsymbol{\lambda_r})}, \begin{pmatrix} \hat{\boldsymbol{\lambda}}_{\boldsymbol{u}} \\ \hat{\boldsymbol{\lambda}}_p \\ \hat{\boldsymbol{\lambda}}_{\boldsymbol{r}} \end{pmatrix} \right\rangle = \boldsymbol{0} \quad \forall\, \hat{\boldsymbol{\lambda}}_{\boldsymbol{u}} \in \boldsymbol{\mathcal{U}},\ \hat{\lambda}_p \in L^2(\Omega),\ \hat{\boldsymbol{\lambda}}_{\boldsymbol{r}} \in \boldsymbol{H}^{-\frac{1}{2}}(\Gamma_i) \ , \tag{2.2.16}$$

$$\left\langle \frac{\partial \mathscr{L}}{\partial(\boldsymbol{u}, p, \boldsymbol{r})}, \begin{pmatrix} \hat{\boldsymbol{u}} \\ \hat{p} \\ \hat{\boldsymbol{r}} \end{pmatrix} \right\rangle = \boldsymbol{0} \quad \forall\, \hat{\boldsymbol{u}} \in \boldsymbol{\mathcal{U}},\ \hat{p} \in L^2(\Omega),\ \hat{\boldsymbol{r}} \in \boldsymbol{H}^{-\frac{1}{2}}(\Gamma_i) \ , \tag{2.2.17}$$

$$\left\langle \frac{\partial \mathscr{L}}{\partial \boldsymbol{g}}, \hat{\boldsymbol{g}} \right\rangle = 0 \quad \forall\, \hat{\boldsymbol{g}} \in \boldsymbol{H}^{\frac{1}{2}}(\Gamma_i) \ . \tag{2.2.18}$$

The equations (2.2.16) and (2.2.17) describe the direct and the so-called adjoint equations to solve for the state variables $(\boldsymbol{u}, p, \boldsymbol{r})$ and the adjoint variables $(\boldsymbol{\lambda_u}, \boldsymbol{\lambda}_p, \boldsymbol{\lambda_r})$ respectively. Finally, the equation (2.2.18) provides the optimality condition of the cost functional with respect to perturbations in $\boldsymbol{g}$. In particular, it also follows that

$$\left\langle \frac{\partial \mathscr{O}}{\partial \boldsymbol{g}}, \hat{\boldsymbol{g}} \right\rangle = \left\langle \frac{\partial \mathscr{L}}{\partial \boldsymbol{g}}, \hat{\boldsymbol{g}} \right\rangle \Bigg|_{\substack{(\boldsymbol{u},p,\boldsymbol{r}) \text{ solution of direct problem} \\ (\boldsymbol{\lambda_u},\lambda_p,\boldsymbol{\lambda_r}) \text{ solution of adjoint problem}}} \ . \tag{2.2.19}$$

Let us now compute the Gâteaux derivatives (2.2.16)–(2.2.18). We first obtain the direct problem by taking the derivative with respect to the variables $(\boldsymbol{\lambda_u}, \lambda_p, \boldsymbol{\lambda_r})$. Then, the following variational problem is obtained:

$$\mathscr{P}_{\text{sta}}(\boldsymbol{g}): \text{ For } \boldsymbol{g} \in \boldsymbol{H}_{00}^{\frac{1}{2}}(\Gamma_i), \text{ determine } (\boldsymbol{u}, p, \boldsymbol{r}) \in \boldsymbol{\mathcal{U}} \times L^2(\Omega) \times \boldsymbol{H}^{-\frac{1}{2}}(\Gamma_i) \text{ such that}$$

$$\left\langle \frac{\partial \mathscr{L}}{\partial \boldsymbol{\lambda_u}}, \hat{\boldsymbol{\lambda}}_{\boldsymbol{u}} \right\rangle = \int_\Omega \left[\rho(\nabla \boldsymbol{u})\boldsymbol{u} \cdot \hat{\boldsymbol{\lambda}}_{\boldsymbol{u}} + 2\mu \nabla^s \boldsymbol{u} \cdot \nabla^s \hat{\boldsymbol{\lambda}}_{\boldsymbol{u}} - p \operatorname{div} \hat{\boldsymbol{\lambda}}_{\boldsymbol{u}}\right] d\Omega - \int_{\Gamma_i} \boldsymbol{r} \cdot \hat{\boldsymbol{\lambda}}_{\boldsymbol{u}} \, d\Gamma = 0 \qquad \forall\, \hat{\boldsymbol{\lambda}}_{\boldsymbol{u}} \in \boldsymbol{\mathcal{U}} \ , \tag{2.2.20}$$

$$\left\langle \frac{\partial \mathscr{L}}{\partial \lambda_p}, \hat{\lambda}_p \right\rangle = -\int_\Omega \hat{\lambda}_p \operatorname{div} \boldsymbol{u} \, d\Omega = 0 \qquad \forall\, \hat{\lambda}_p \in L^2(\Omega) \ , \tag{2.2.21}$$

$$\left\langle \frac{\partial \mathscr{L}}{\partial \boldsymbol{\lambda_r}}, \hat{\boldsymbol{\lambda}}_{\boldsymbol{r}} \right\rangle = -\int_{\Gamma_i} \hat{\boldsymbol{\lambda}}_{\boldsymbol{r}} \cdot (\boldsymbol{u} - \boldsymbol{g}) \, d\Gamma = 0 \qquad \forall\, \hat{\boldsymbol{\lambda}}_{\boldsymbol{r}} \in \boldsymbol{H}^{-\frac{1}{2}}(\Gamma_i) \ . \tag{2.2.22}$$

The Euler-Lagrange equations associated with (2.2.20)-(2.2.21)-(2.2.22) are the classical Navier-Stokes equations, which read as follows:

$$\rho(\nabla \boldsymbol{u})\boldsymbol{u} - \mu \Delta \boldsymbol{u} + \nabla p = \boldsymbol{0} \qquad \text{in } \Omega \ , \tag{2.2.23}$$

$$\operatorname{div} \boldsymbol{u} = 0 \qquad \text{in } \Omega \ , \tag{2.2.24}$$

$$\boldsymbol{u} = \boldsymbol{0} \qquad \text{on } \Gamma_w \ , \tag{2.2.25}$$

$$\boldsymbol{u} = \boldsymbol{g} \qquad \text{on } \Gamma_i \ , \tag{2.2.26}$$

$$(-p\boldsymbol{I} + 2\mu \nabla^s \boldsymbol{u})\boldsymbol{n} = \boldsymbol{r} \qquad \text{on } \Gamma_i \ , \tag{2.2.27}$$

$$(-p\boldsymbol{I} + 2\mu \nabla^s \boldsymbol{u})\boldsymbol{n} = \boldsymbol{0} \qquad \text{on } \Gamma_o \ . \tag{2.2.28}$$

Second, we obtain the adjoint problem by taking the derivative of the Lagrangian (2.2.6) with respect to the state variables $(\boldsymbol{u}, p, \boldsymbol{r})$. The adjoint problem then reads as

$$\mathscr{P}_{\text{adj}}(\boldsymbol{u}, \tilde{\boldsymbol{u}}^t): \text{ For } \tilde{\boldsymbol{u}}^t, \text{ and } \boldsymbol{u}, \text{ solution of (2.2.23)–(2.2.28)},$$
$$\text{determine } (\boldsymbol{\lambda_u}, \lambda_p, \boldsymbol{\lambda_r}) \in \boldsymbol{\mathcal{U}} \times L^2(\Omega) \times \boldsymbol{H}^{-\frac{1}{2}}(\Gamma_i), \text{ such that}$$

$$\left\langle \frac{\partial \mathscr{L}}{\partial \boldsymbol{u}}, \hat{\boldsymbol{u}} \right\rangle = \int_{\Gamma_o \cup \Gamma_i} \left[\alpha \left(\chi_{\Gamma_{so}} + \chi_{\Gamma_{si}}\right)(\boldsymbol{u} - \tilde{\boldsymbol{u}}^t) \cdot \hat{\boldsymbol{u}}\right] d\Gamma - \int_{\Gamma_i} \left(\boldsymbol{\lambda_r} \cdot \hat{\boldsymbol{u}}\right) d\Gamma + \int_\Omega \left[\alpha \, \chi_{\Omega_s}(\boldsymbol{u} - \tilde{\boldsymbol{u}}^t) \cdot \hat{\boldsymbol{u}} + \rho(\nabla \hat{\boldsymbol{u}})\boldsymbol{u} \cdot \boldsymbol{\lambda_u} + \rho(\nabla \boldsymbol{u})\hat{\boldsymbol{u}} \cdot \boldsymbol{\lambda_u} + 2\mu \nabla^s \hat{\boldsymbol{u}} \cdot \nabla^s \boldsymbol{\lambda_u} - \lambda_p \operatorname{div} \hat{\boldsymbol{u}}\right] d\Omega = 0 \qquad \forall\, \hat{\boldsymbol{u}} \in \boldsymbol{\mathcal{U}} \ , \tag{2.2.29}$$

$$\left\langle \frac{\partial \mathscr{L}}{\partial p}, \hat{p} \right\rangle = -\int_\Omega \hat{p} \operatorname{div} \boldsymbol{\lambda_u} \, d\Omega = 0 \qquad \forall\, \hat{p} \in L^2(\Omega) \ , \tag{2.2.30}$$

$$\left\langle \frac{\partial \mathscr{L}}{\partial \boldsymbol{r}}, \hat{\boldsymbol{r}} \right\rangle = -\int_{\Gamma_i} \hat{\boldsymbol{r}} \cdot \boldsymbol{\lambda_u} \, d\Gamma = 0 \qquad \forall\, \hat{\boldsymbol{r}} \in \boldsymbol{H}^{-\frac{1}{2}}(\Gamma_i) \ , \tag{2.2.31}$$

where we considered the following indicator functions:

$$\chi_{\Omega_s} = \begin{cases} 1 & \text{in } \Omega_s \ , \\ 0 & \text{in } \Omega \setminus \Omega_s \ , \end{cases} \qquad \chi_{\Gamma_{si}} = \begin{cases} 1 & \text{in } \Gamma_{si} \ , \\ 0 & \text{in } \Gamma_i \setminus \Gamma_{si} \ , \end{cases} \qquad \chi_{\Gamma_{so}} = \begin{cases} 1 & \text{in } \Gamma_{so} \ , \\ 0 & \text{in } \Gamma_o \setminus \Gamma_{so} \ . \end{cases} \tag{2.2.32a–c}$$

Applying standard variational arguments for (2.2.29)-(2.2.30)-(2.2.31) delivers the associated Euler-Lagrange equations, as follows:

$$\alpha\, \chi_{\Omega_s}(\boldsymbol{u} - \tilde{\boldsymbol{u}}^t) - \rho(\nabla \boldsymbol{\lambda_u})\boldsymbol{u} + \rho(\nabla \boldsymbol{u})^T \boldsymbol{\lambda_u} - \mu \Delta \boldsymbol{\lambda_u} + \nabla \lambda_p = \boldsymbol{0} \qquad \text{in } \Omega \ , \tag{2.2.33}$$

$$\operatorname{div} \boldsymbol{\lambda_u} = 0 \qquad \text{in } \Omega \ , \tag{2.2.34}$$

$$\boldsymbol{\lambda_u} = \boldsymbol{0} \qquad \text{on } \Gamma_w \ , \tag{2.2.35}$$

$$\boldsymbol{\lambda_u} = \boldsymbol{0} \qquad \text{on } \Gamma_i \ , \tag{2.2.36}$$

$$\alpha\, \chi_{\Gamma_{si}}(\boldsymbol{u} - \tilde{\boldsymbol{u}}^t) + (-\lambda_p \boldsymbol{I} + 2\mu \nabla^s \boldsymbol{\lambda_u})\boldsymbol{n} = \boldsymbol{\lambda_r} \qquad \text{on } \Gamma_i \ , \tag{2.2.37}$$

$$\alpha\, \chi_{\Gamma_{so}}(\boldsymbol{u} - \tilde{\boldsymbol{u}}^t) + \rho(\boldsymbol{u} \cdot \boldsymbol{n})\boldsymbol{\lambda_u} + (-\lambda_p \boldsymbol{I} + 2\mu \nabla^s \boldsymbol{\lambda_u})\boldsymbol{n} = \boldsymbol{0} \qquad \text{on } \Gamma_o \ . \tag{2.2.38}$$

Finally, let us compute the optimality condition, which states

$$\mathscr{P}_{\text{opt}}(\boldsymbol{\lambda_r}) : \text{ For } \boldsymbol{\lambda_r}, \text{ solution of (2.2.33)–(2.2.38), determine } \boldsymbol{g} \in \boldsymbol{H}_0^1(\Gamma_i), \text{ such that}$$
$$\left\langle \frac{\partial \mathscr{L}}{\partial \boldsymbol{g}}, \hat{\boldsymbol{g}} \right\rangle = \int_{\Gamma_i} \left[\beta \boldsymbol{g} \cdot \hat{\boldsymbol{g}} + \beta_1 \nabla_{\boldsymbol{\tau}} \boldsymbol{g} \cdot \nabla_{\boldsymbol{\tau}} \hat{\boldsymbol{g}} + \boldsymbol{\lambda_r} \cdot \hat{\boldsymbol{g}} \right] d\Gamma = 0 \quad \forall\, \hat{\boldsymbol{g}} \in \boldsymbol{H}_0^1(\Gamma_i) \ . \tag{2.2.39}$$

The Euler-Lagrange equations associated with (2.2.39) are the following:

$$\beta \boldsymbol{g} - \beta_1 \triangle_{\boldsymbol{\tau}} \boldsymbol{g} = -\boldsymbol{\lambda_r} \qquad \text{on } \Gamma_i \ , \tag{2.2.40}$$

$$\boldsymbol{g} = \boldsymbol{0} \qquad \text{on } \gamma_i \ , \tag{2.2.41}$$

where $\boldsymbol{\lambda_r}$ is solution of the adjoint problem $\mathscr{P}_{\text{adj}}$.

The well-posedness of the fully coupled non-linear system of necessary conditions given by (2.2.20)-(2.2.21)-(2.2.22), (2.2.29)-(2.2.30)-(2.2.31) and (2.2.39) has not yet been yet addressed in the literature to the best of the authors' knowledge. In this regard, we rely on the well-posedness result reported by Guerra *et al.* [Gue15] for the minimization problem (2.2.5).

2.2.3 Gradient Descent Algorithm

The procedure to solve the optimality conditions at once amounts to solving the nonlinear system of coupled variational equations $\mathscr{P}_{\text{sta}}$, $\mathscr{P}_{\text{adj}}$ and $\mathscr{P}_{\text{opt}}$ (or their corresponding Euler-Lagrange equations (2.2.23)–(2.2.28), (2.2.33)–(2.2.38) and (2.2.40)–(2.2.41)). This problem is nonlinear and a possible way to find the stationary point for the optimisation problem $\mathscr{P}_M$ is to evaluate the Gâteaux derivative (2.2.19) to drive a descent-like iterative algorithm. In this case, first, given a guess $\boldsymbol{g}$, the forward problem, $\mathscr{P}_{\text{sta}}$, is solved to obtain the state variables,

$(\boldsymbol{u}, p, \boldsymbol{r})$. Second, the adjoint problem, $\mathscr{P}_{\text{adj}}$, is evaluated using the solution, $\boldsymbol{u}$, from the direct problem. Then, using the adjoint variable, $\boldsymbol{\lambda_r}$, obtained from the adjoint problem, the gradient of the objective function with respect to the parameter $\boldsymbol{g}$ can be calculated from (2.2.39) as follows:

$$\frac{D\mathscr{O}(\boldsymbol{g})}{D\boldsymbol{g}} = \beta\boldsymbol{g} - \beta_1 \triangle_{\boldsymbol{\tau}} \boldsymbol{g} + \boldsymbol{\lambda_r} \quad \text{on } \Gamma_i \ . \tag{2.2.42}$$

To ensure an acceptable converging solution of the algorithm, it is usual to start by solving the forward problem based on some initial guess, $(\boldsymbol{u})_0$, for the flow field. Therefore, we introduce a proper linearisation, $\mathscr{P}^{\text{lin}}_{\text{sta}}$, of the forward problem, $\mathscr{P}_{\text{sta}}$, as

$\mathscr{P}^{\text{lin}}_{\text{sta}}(\boldsymbol{u}^*, \boldsymbol{g}^*)$: For $\boldsymbol{u}^*$ and $\boldsymbol{g}^*$, determine $(\boldsymbol{u}, p, \boldsymbol{r})$ such that

$$\int_\Omega \left[\rho(\nabla \boldsymbol{u})\boldsymbol{u}^* \cdot \hat{\boldsymbol{\lambda}}_{\boldsymbol{u}} + 2\mu \nabla^s \boldsymbol{u} \cdot \nabla^s \hat{\boldsymbol{\lambda}}_{\boldsymbol{u}} - p \operatorname{div} \hat{\boldsymbol{\lambda}}_{\boldsymbol{u}}\right] d\Omega -$$

$$- \int_{\Gamma_i} \boldsymbol{r} \cdot \hat{\boldsymbol{\lambda}}_{\boldsymbol{u}} \, d\Gamma = 0 \qquad \forall\, \hat{\boldsymbol{\lambda}}_{\boldsymbol{u}} \in \boldsymbol{\mathcal{U}} \ , \tag{2.2.43}$$

$$- \int_\Omega \hat{\lambda}_p \operatorname{div} \boldsymbol{u} \, d\Omega = 0 \qquad \forall\, \hat{\lambda}_p \in L^2(\Omega) \ , \tag{2.2.44}$$

$$- \int_{\Gamma_i} \hat{\boldsymbol{\lambda}}_{\boldsymbol{r}} \cdot (\boldsymbol{u} - \boldsymbol{g}^*) \, d\Gamma = 0 \qquad \forall\, \hat{\boldsymbol{\lambda}}_{\boldsymbol{r}} \in \boldsymbol{H}^{-\frac{1}{2}}(\Gamma_i) \ . \tag{2.2.45}$$

The optimality condition, (2.2.39), ensures that the derivative of the objective functional with respect to the control parameters vanishes at the critical point. In the gradient descent algorithm, however, the optimality condition is not satisfied until the algorithm converges. That procedure is described in algorithm 1 below. The fields $(\cdot)^k$ correspond to the fields $(\cdot)$ at the k-th iteration. The parameter σ represents the step size, which is adjusted dynamically. To test convergence, a small parameter ξ is prescribed as a tolerance to potentially exit the algorithm, if necessary.

2.2.4 Numerical Methods

The direct and adjoint problems were approximated using the finite volume method. The linearised problem, $\mathscr{P}^{\text{lin}}_{\text{sta}}$, was solved using the SIMPLE algorithm described by Patankar *et al.* [Pat72]. According to this, the momentum equation (2.2.23) is solved (after proper linearisation and discretisation) starting with an initial guess for pressure. In addition, a pressure correction equation is derived from the continuity equation (2.2.23) obtaining the pressure correction field, which is then used to update both the pressure and the velocity. To solve the discretised momentum equation, we applied the Gauss-Seidel method. Then, the discretised pressure correction equation was solved using a generalised geometric-algebraic multi-grid (GAMG) solver using Gauss-Seidel iterations. The adjoint equations (2.2.33)–(2.2.38) were discretised and solved in a similar way, following the SIMPLE algorithm and

using the same solvers as described for the solution of the direct problem. That is, Gauss-Seidel iterations were used to solve the adjoint momentum equation (2.2.33) (after its corresponding discretisation) and GAMG was used to solve the discretised adjoint pressure correction derived from the adjoint continuity equation (2.2.34). The entire optimisation algorithm including the direct and adjoint solvers was implemented using OpenFOAM [Wel98].

Algorithm 1 Steepest descent with dynamic step size

Given: $\alpha, \beta, \beta_1 > 0$ ▷ Set optimisation parameters
Input : $\boldsymbol{u}^0, \boldsymbol{g}^0, \tilde{\boldsymbol{u}}^t$ ▷ Provide initial guess and target flow
Output : $\boldsymbol{u}^k$ ▷ Flow field at last iteration k

procedure DataAssimilation($\boldsymbol{u}^0, \boldsymbol{g}^0, \tilde{\boldsymbol{u}}^t$)
  $\sigma \leftarrow 1$, $\xi \leftarrow 10^{-8}$ and $k \leftarrow 0$
  $(\boldsymbol{u}^0, \cdot, \cdot) \leftarrow \mathscr{P}^{\text{lin}}_{\text{sta}}(\boldsymbol{u}^0, \boldsymbol{g}^0)$ ▷ Evaluate linearised problem (2.2.43)
  $cost^0 \leftarrow \mathscr{O}^*(\boldsymbol{u}^0, \boldsymbol{g}^0, \tilde{\boldsymbol{u}}^t)$ ▷ Evaluate cost function (2.2.5)
  for $k \leftarrow 1, n$ **do**
    $(\cdot, \cdot, \boldsymbol{\lambda}^k_{\boldsymbol{r}}) \leftarrow \mathscr{P}_{\text{adj}}(\boldsymbol{u}^{k-1}, \tilde{\boldsymbol{u}}^t)$ ▷ Evaluate adjoint problem (2.2.29)–(2.2.31)
    $\boldsymbol{s}^k \leftarrow -(\beta \boldsymbol{g}^{k-1} - \beta_1 \triangle_{\boldsymbol{\tau}} \boldsymbol{g}^{k-1} + \boldsymbol{\lambda}^k_{\boldsymbol{r}})$ ▷ Set steepest descent direction (2.2.42)
    repeat
      $\boldsymbol{g}^k \leftarrow \boldsymbol{g}^{k-1} + \sigma \boldsymbol{s}^k$ ▷ Update control, using step size σ
      $(\boldsymbol{u}^k, \cdot, \cdot) \leftarrow \mathscr{P}^{\text{lin}}_{\text{sta}}(\boldsymbol{u}^{k-1}, \boldsymbol{g}^k)$
      $cost^k \leftarrow \mathscr{O}^*(\boldsymbol{u}^k, \boldsymbol{g}^k, \tilde{\boldsymbol{u}}^t)$
      if $cost^k \geq cost^{k-1}$ **then**
        $\sigma \leftarrow 0.5\sigma$
      end if
    until $cost^k < cost^{k-1}$
    if $(\left|cost^k - cost^{k-1}\right|)/(cost^k) > \xi$ **then**
      $\sigma \leftarrow 1.5\sigma$
    else
      return $\boldsymbol{u}^k$
    end if
  end for
end procedure

2.3 Preprocessing of Observational Data

The proposed approach was validated and tested based on data that were generated both artificially and empirically. Generated artificial data were used to validate the approach both on a simplified geometry with an available analytical solution (see section 2.4) as well as on a physical glass replica of a human aorta. The latter geometry was used to generate a reference

flow solution to be considered as the ground truth for validation purposes (see section 2.5.4). The experimental data were generated with real measurements of flow MRI acquired for the glass replica of the aorta (see section 2.5). Both kinds of observations contain either some artificially added or realistic noise respectively. Hence, the data further require some preprocessing prior to the application of the proposed optimisation algorithm. Let $\boldsymbol{u}_{\mathbf{mri}}$ denote the noisy data, which are either artificially generated or obtained from the MR scan. First of all, a noise detection strategy (see section 2.3.1) was applied to the observed data, $\boldsymbol{u}_{\mathbf{mri}}$, to eliminate potential spurious vectors, yielding a denoised flow field, $\boldsymbol{u}^{\circ}_{\mathbf{mri}}$. Second, the vascular domain was segmented from the (either artificial or experimental) MRI data and was registered with the exact phantom geometry (for both the experimental scenario with the flow MRI scan and the artificially generated reference flow solution on the phantom). For both artificial and experimental data, the geometries were available as either a user-generated cylinder or the surface data representing the 3-D print of the glass replica respectively. Furthermore, the computational mesh was created from these exact geometries. The measured and denoised velocity field, $\boldsymbol{u}^{\circ}_{\mathbf{mri}}$, inside the segmented region of interest was mapped into the computational mesh domain, using the transformation obtained from the registration step. This mapping was performed using linear interpolation, yielding a denoised flow field in the computational mesh domain, denoted as $\bar{\boldsymbol{u}}_{\mathbf{mri}}$. Finally, a space projection was applied to $\bar{\boldsymbol{u}}_{\mathbf{mri}}$ to recover back the divergence-free property of the flow data, which returns a flow field called $\tilde{\boldsymbol{u}}^{\star}$. The preprocessing steps can be tabularly summarised as follows:

$$\boldsymbol{u}_{\mathbf{mri}} \xrightarrow{\text{Outlier Detection}} \boldsymbol{u}^{\circ}_{\mathbf{mri}} \xrightarrow{\text{Registration}} \bar{\boldsymbol{u}}_{\mathbf{mri}} \xrightarrow{\text{Space Projection}} \tilde{\boldsymbol{u}}^{\star}$$

$\boldsymbol{u}_{\mathbf{mri}}$: Reconstructed flow field from 4-D flow MRI (or artificially generated),

$\boldsymbol{u}^{\circ}_{\mathbf{mri}}$: Denoised flow field defined in observational domain (usually coarse mesh),

$\bar{\boldsymbol{u}}_{\mathbf{mri}}$: Linearly interpolated flow field mapped in the computational domain (fine mesh),

$\tilde{\boldsymbol{u}}^{\star}$: Divergence-free flow field defined in the computational domain.

2.3.1 Noise Detection

A variation of the usual median test, proposed by Westerweel *et al.* [Wes05] and initially applied to PIV, was implemented and applied to MRI data, $\boldsymbol{u}_{\mathbf{mri}}$, for detecting the spurious vectors in the measurements. The method utilises a normalization to the original median test and considers the local fluctuations of the flow field. For a wide variety of documented flow cases, Westerweel and Scarano verified the generality of the method for Re numbers ranging from 10^{-1} to 10^{7}.

For a more formal description of the method, let us first introduce a set of 3-tuples,

$$N_R = \{\, (i,j,k) \in \mathbb{Z} \mid -R \leq i,j,k \leq R \wedge R \in \mathbb{N} \,\} \setminus \{\, (0,0,0) \,\} \quad . \tag{2.3.1}$$

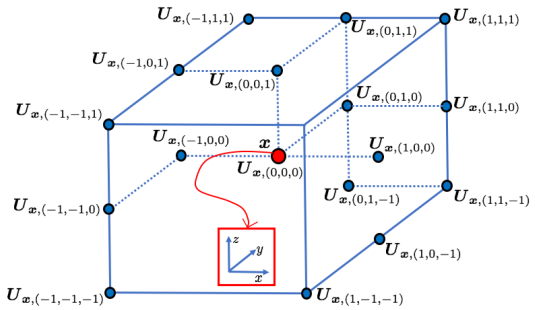

Figure 2.2: For $R = 1$, the set $\boldsymbol{U}_{\boldsymbol{x},N_1}$ is shown with the 26 neighbours of $\boldsymbol{U}_{\boldsymbol{x}}$ (not all neighbours illustrated). Note that N_R does not contain the tuple $(0, 0, 0)$, hence $\boldsymbol{U}_{\boldsymbol{x}} = \boldsymbol{U}_{\boldsymbol{x},(0,0,0)}$ is not included in $\boldsymbol{U}_{\boldsymbol{x},N_1}$.

Second, we define $\boldsymbol{U}_{\boldsymbol{x}} = \boldsymbol{U}_{\boldsymbol{x},(0,0,0)} \in \mathbb{R}^n$ to be the displacement vector at pixel position $\boldsymbol{x}$ and $\boldsymbol{U}_{\boldsymbol{x},N_R}$ is the set of its $[(2R+1)^3 - 1]$ neighbours. Figure 2.2 illustrates the neighborhood for $R = 1$. Additionally, let $\boldsymbol{U}_{\boldsymbol{x},\text{med}}$ be the median of $\boldsymbol{U}_{\boldsymbol{x},N_R}$. The classical median test value is defined as $(\text{MT})_{\boldsymbol{x},N_R} = \|\boldsymbol{U}_{\boldsymbol{x},\text{med}} - \boldsymbol{U}_{\boldsymbol{x}}\|$, which is passed if it is smaller than a user defined threshold value ϵ_t. Furthermore, we define the set of residuals, $r_{\boldsymbol{x},N_R}$, as

$$r_{\boldsymbol{x},N_R} = \{\, r \in \mathbb{R} \mid r = \|\boldsymbol{U} - \boldsymbol{U}_{\boldsymbol{x},\text{med}}\| \wedge \boldsymbol{U} \in \boldsymbol{U}_{\boldsymbol{x},N_R} \,\} \quad , \tag{2.3.2}$$

and, similarly, $r_{\boldsymbol{x},\text{med}}$ is defined to be the median of $r_{\boldsymbol{x},N_R}$, which is used to normalise the usual median test,

$$(\text{NMT})_{\boldsymbol{x},N_R} = \frac{\|\boldsymbol{U}_{\boldsymbol{x},\text{med}} - \boldsymbol{U}_{\boldsymbol{x}}\|}{r_{\boldsymbol{x},\text{med}} + \epsilon} < \epsilon_t \quad . \tag{2.3.3}$$

Under uniform flow conditions, the main normalization factor $r_{\boldsymbol{x},\text{med}}$ tends to yield zero: hence, a small and acceptable local fluctuation level ϵ is applied to compensate for a potential division by zero and to account for remaining velocity fluctuations obtained from cross correlation analysis. In practice, ϵ values between 0.1 and 0.2 might be used [Wes05; Raf07; Gar11]. In our case, $\epsilon = 0.2$ performed well for the available MR flow data. Furthermore, $\epsilon_t = 2.25$ is used as the validation threshold. Once the latter parameter is detected from numerical experiments, it can be used for other data in similar flow regimes with the same imaging modality.

Prior to the application of noise detection, the observations $\boldsymbol{u}_{\mathbf{mri}}$ obtained from MRI measurements are initially already divergence-free. This is ensured by the constraints applied during the reconstruction process of the MRI data, which is out of the scope of this work. After denoising, however, the detected spurious vectors are erased from the data, which results in a flow field $\boldsymbol{u}^{\circ}_{\mathbf{mri}}$ with gaps at certain positions within the observations. This clearly violates the divergence-free property of the observed data, $\boldsymbol{u}_{\mathbf{mri}}$. One possible way to fill in the gaps would be the use of some interpolation scheme. However, such schemes will not

necessarily ensure a solenoidal flow field. Therefore, we rely on the application of a projection over a divergence-free space at a later stage (see section 2.3.4) to automatically fill in the aforementioned gaps and to recover back the divergence-free property of the flow field.

2.3.2 Segmentation and Registration

After the removal of outliers, the arterial structures, in which the analysis is to be performed, are segmented from both the artificially generated flow data as well as the acquired MR measurements. The experimental MRI data comprise the anatomical structures and the velocity field data [Mar12], whereas the artificial flow data consist of the flow field generated either in a cylindrical geometry or in the geometry of the phantom aorta. For validation studies in the simplified domain, the flow data were used for segmentation of the cylindrical geometry (see section 2.4), whereas for experimental and complementary validation studies, the anatomical data from MR images were used to extract the vascular geometry from the aorta replica (see section 2.5). The segmentation was performed using the snake evolution method available in ITK-SNAP (www.itksnap.org) and was smoothed using the tools available in the VMTK library (www.vmtk.org). This procedure is expected to suffer from the low resolution and partial volume effects of flow MRI data.

For the comparison with experimental MRI data, high-resolution aortic surface data were already available from the 3-D print of the glass replica. The latter were used to generate the computational mesh for the exact geometry. However, after image acquisition and segmentation, the flow data are misaligned with the exact geometry of the replica. Therefore, a registration step was necessary to align the measured flow field with the exact geometry of the replica. The rigid registration was performed using the iterative closest point (ICP) algorithm, which aims to minimise the distance between two sets of points. The numbers of available points in the point clouds of both the exact and the segmented geometries were approximately 1 600 000 and 12 000 respectively. Prior to the registration process, 5 000 points were randomly sampled from each geometry, which were then used as the two point input clouds for the ICP algorithm. The root mean square error between the registered point clouds was 0.001. In the case of the artificially generated flow data in the cylindrical domain, no registration step was required, since the geometry was already aligned with the segmented domain.

2.3.3 Mapping in the Computational Mesh

For both cases, the analytical geometry (cylinder) and the experimental geometry (glass replica of aorta), the available exact geometries were used to generate the computational mesh domain, which was used for the flow simulations. For both datasets, a hexahedral mesh was created using OpenFOAM's snappyHexMesh procedure. In the case of the experimental geometry, the mesh was rigidly transformed into its corresponding segmentation using the mapping obtained from the registration step. After mesh generation, the velocities, $\boldsymbol{u}^{\circ}_{\mathbf{mri}}$, from the

denoised phase difference images (obtained from 4-D flow MRI and denoised with the universal outlier detection scheme) with limited resolution (i.e. in a coarse observational domain) were mapped into the fine hexahedral mesh (computational domain for CFD simulations with high resolution) using the linear interpolation method available in ITK [Joh13]. As a result of the combination of the linear interpolation and the previous noise detection process, the final flow field (denoted by $\bar{\boldsymbol{u}}_{\mathbf{mri}}$) in the CFD mesh was not divergence-free. The divergence-free property was then recovered with the projection over a divergence-free space applied to the velocity field in the CFD mesh as explained next.

2.3.4 Projection into Divergence-Free Space

Let $\bar{\boldsymbol{u}}_{\mathbf{mri}} \in \left(L^2\left(\Omega\right)\right)^3$ be a given observed velocity field on a bounded Lipschitz domain $\Omega \in \mathbb{R}^3$ with boundary $\partial\Omega$. According to Helmholtz-Hodge decomposition (HHD), the velocity field can be decomposed into the sum of its divergence-free, curl-free and gradient of harmonic components, if the velocity is known at the boundary [Den03; Har12; Bha13]. In this work, we reconstruct the divergence-free flow field by removing the gradient of the harmonic component and solving the following problem:

$$\begin{aligned} \mathscr{P}_{\perp}(\bar{\boldsymbol{u}}_{\mathbf{mri}}):\ &\text{Given } \bar{\boldsymbol{u}}_{\mathbf{mri}},\ \text{find } \tilde{\boldsymbol{u}}^{\star} = \bar{\boldsymbol{u}}_{\mathbf{mri}} - \nabla q,\ \text{such that} \\ &\Delta q = \nabla \cdot \bar{\boldsymbol{u}}_{\mathbf{mri}} \text{ in } \Omega \\ &q = 0 \text{ on } \Gamma_w \quad \text{and} \quad \nabla q \cdot \boldsymbol{n} = 0 \text{ on } \partial\Omega \backslash \Gamma_w \ . \end{aligned} \tag{2.3.4}$$

The problem $\mathscr{P}_{\perp}$ differs from the HHD in terms of the applied BCs, but under certain modifications the HHD can be recovered. Although the problem $\mathscr{P}_{\perp}$ does not directly correspond to the HHD, it still represents a projection over a space of divergence-free flow fields.

The observations, $\bar{\boldsymbol{u}}_{\mathbf{mri}}$, are assumed to be already modified by the application of the universal outlier detection scheme (as described in section 2.3.1) prior to its projection in the CFD mesh. The projection ($\boldsymbol{u}^{\circ}_{\mathbf{mri}} \rightarrow \bar{\boldsymbol{u}}_{\mathbf{mri}}$) is performed by linear interpolation. Problem $\mathscr{P}_{\perp}$ is solved using OpenFOAM's [Wel98] conjugate gradient solver (PCG) with simplified diagonal-based incomplete Cholesky preconditioner (DIC). Figure 2.3 illustrates that the projection into the space of divergence-free vector fields (in the phantom replica of the human aorta) recovers the divergence-free property of the flow field to a great extent.

2.4 Validation of the Methodology

To validate the approach and analyse its performance, we consider the flow of a fluid in a cylindrical geometry, where an analytical solution of a fully developed flow is available. In this work, first an analytical solution is generated for a fine hexahedral mesh of a cylinder. Second, a much coarser voxel grid is used to simulate the MRI acquisition pipeline. For each voxel, the MRI simulation is based on the averaged velocity field provided by the fine mesh.

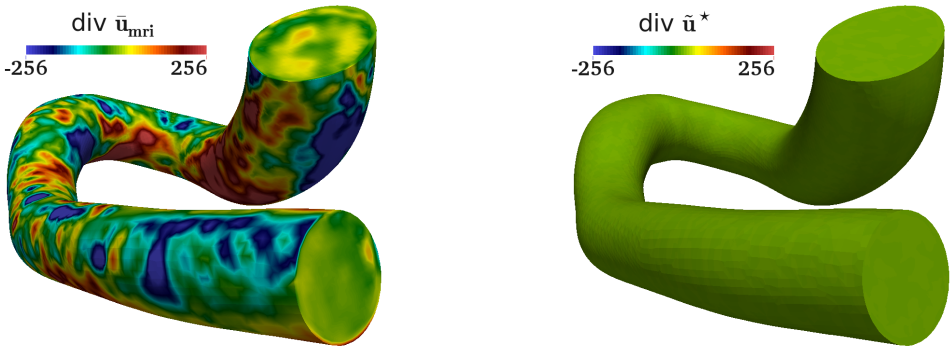

(a) (b)

Figure 2.3: Divergence of flow field in a phantom of a human aorta acquired with MRI: (a) Raw data, before the application of divergence-free projection operator, $\mathscr{P}_{\perp}$. (b) Divergence-free flow field, after the application of $\mathscr{P}_{\perp}$.

Furthermore, some artificial noise is added to the voxel data and, finally, these artificially generated MRI data are put into the preprocessing pipeline described in section 2.3.

2.4.1 Poiseuille Flow

We consider the fully developed laminar flow of a Newtonian fluid in a cylinder of length L, constant cross-sectional area A and diameter D ($R = D/2$ is the pipe radius). The solution of the Navier-Stokes equations in this case yields

$$\boldsymbol{u}_{\mathbf{ext}}(r) = \frac{\Delta P D^2}{16 \nu \rho L} \left(1 - \frac{r^2}{R^2}\right) \quad . \tag{2.4.1}$$

From (2.4.1), and calling $\boldsymbol{U}_{\mathbf{avr}}$ the average velocity, it can be derived that

$$\boldsymbol{u}_{\mathbf{ext}}(r) = 2\boldsymbol{U}_{\mathbf{avr}} \left(1 - r^2/R^2\right) . \tag{2.4.2}$$

Finally, taking $Re = D\boldsymbol{U}_{\mathbf{avr}}/\nu$, the analytical solution can be given in terms of the Reynolds number and kinematic viscosity as

$$\boldsymbol{u}_{\mathbf{ext}}(r) = \frac{2\nu Re}{D} \left(1 - \frac{r^2}{R^2}\right) \quad . \tag{2.4.3}$$

2.4.2 Evaluation of Analytical Solution

During the MRI acquisition process, the velocities are spatially averaged. To simulate such a framework, the exact solution from equation (2.4.3) needs to be spatially averaged to the desired MRI voxel size. Since it is not possible to calculate the exact solution for an infinite number of points, its evaluation was performed on each cell center of a fine hexahedral mesh with 3 693 600 cells. The cylinder radius was $R = 1.2$ cm (diameter $D = 2.4$ cm) and the

length was $L = 6$ cm (see figure 2.4(c)). As the solution described by the Hagen-Poiseuille equation (2.4.1) is valid for laminar flow, the Reynolds number was chosen to be 2 000. Finally, as a reasonable approximation of blood viscosity in the human aorta, the kinematic viscosity was chosen to be $\nu = 4.8$ cP. Under these conditions, the maximum flow velocity in the aforementioned cylinder approximately results in $|\boldsymbol{u}|_{max} \approx 0.8$ m/s.

2.4.3 Generation of Artificial MRI Data

The acquired velocities with flow MRI are proportional to the phase shift in the signal of spins moving along a magnetic gradient field. Since the phase of a signal is limited to 2π radians, so is also the range of velocities that can be detected uniquely. The highest velocity that is likely to be encountered within the region of interest is held within a user-defined velocity encoding (VENC). For velocity magnitudes higher than the VENC, the so-called velocity aliasing effect (or phase wrap-around artifact) occurs, which prevents the unique assignment of the velocities. The quality of flow MRI suffers from velocity noise, which is proportional to the velocity encoding and inversely associated with the signal-to-noise ratio (SNR) in the related phase difference images [Pel91]. As described by Pelc *et al.* [Pel91], the standard deviation of the velocity can be approximated as

$$\sigma_u \approx (0.45 * \text{VENC})/\text{SNR} \ . \tag{2.4.4}$$

Gudbjartsson *et al.* [Gud95] showed that in the existence of noise, the image intensity in phase-contrast MRI is governed by the Rician distribution. For SNR greater than two, the noise distribution is shown to be nearly Gaussian. The analytical solution evaluated in the fine mesh was first averaged into an MRI grid of 2 mm voxel size in each direction, as shown in figure 2.4(a). Gaussian white noise was added thereafter on the averaged velocities, as shown in figure 2.4(b). The VENC was chosen to be 120 cm/s in the longitudinal direction (z), whereas it was 20 cm/s in the remaining directions (x and y). The standard deviation of the velocity was chosen such that the noise amplitude corresponded to an SNR of 20. As the cylinder is user-defined, the acquired flow field is already registered with the exact geometry. After the addition of artificial noise, the thus-simulated MRI data follow the pre-processing pipeline (with the exception of the registration stage) as described in section 2.3, before starting the CFD simulation. In what follows, $\boldsymbol{u}_{\mathbf{snr}}$ will represent the noisy MRI measurements, which are mapped into the computational domain and for which a decomposition is applied to project the field over a divergence-free space as described in sections 2.3.3 and 2.3.4. The cylindrical computational domain is illustrated in figure 2.4(c).

2.4.4 Optimisation with Exact Solution as Target Flow

First, we consider one case where the optimisation starts with a noisy flow field and is performed against the exact solution. That is, the target flow field $\tilde{\boldsymbol{u}}^t$ in the objective function

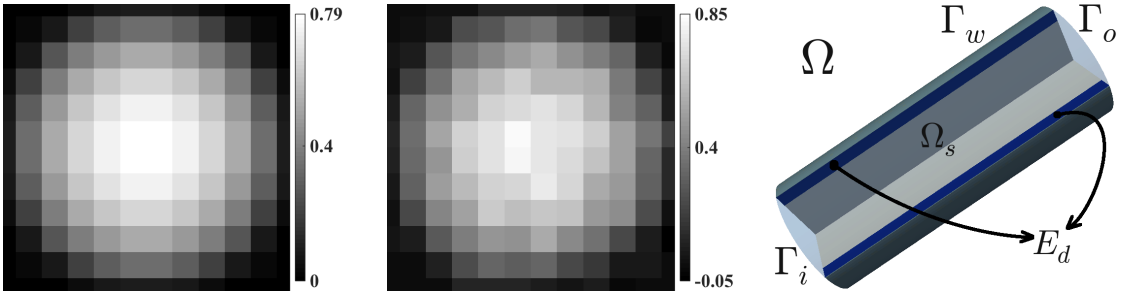

(a) Exact averaged solution (b) Artificial noisy solution (c) Flow Domain

Figure 2.4: Artificially generated velocity images (2 mm isotropic voxel size) of both the exact solution (a) and the integrated noise with a SNR of 20 (b), before their mapping into the computational flow domain (c).

(2.2.5) corresponds to $\boldsymbol{u}_{\mathbf{ext}}$ given by (2.4.3). In addition, the initial condition, $(\boldsymbol{u})_0 = \boldsymbol{u}^0$, corresponds to the artificially generated divergence-free flow field, $\boldsymbol{u}_{\mathbf{snr}}$, as described in section 2.4.3. Thus, algorithm 1 is executed with the input parameters $(\boldsymbol{u}_{\mathbf{snr}}, \boldsymbol{g}_{\mathbf{snr}}, \boldsymbol{u}_{\mathbf{ext}})$, where $\boldsymbol{g}_{\mathbf{snr}} = \boldsymbol{u}_{\mathbf{snr}}$ on Γ_i. In what follows, we will denote $\boldsymbol{u}_{\mathbf{opt}} = \boldsymbol{u}^k_{\mathbf{opt}}$ as the solution returned by the optimisation process after k iterations of algorithm 1. The mesh is set up with 118 800 cells including 114 840 hexahedras and 3 960 prisms. The size of the mesh is suitable to obtain satisfactory results. Flow-matching domains, Ω_s, Γ_{si} and Γ_{so} (see figure 2.4(c)), cover the lumen including both inlet and outlet boundaries. In what follows, we will give a meaning to the subscript, s, in the flow-matching domain, Ω_s. The subscript s prescribes the extent of contraction of the whole domain Ω in millimetres (mm), as follows:

$$\Omega_s = \{\, \boldsymbol{x} \in \Omega \mid \|\boldsymbol{x} - \boldsymbol{y}\| \geq s\,(\text{mm})\, \forall \boldsymbol{y} \in \Gamma_w \,\} \quad . \tag{2.4.5}$$

In this set-up, we set $s = 2$. That is, the flow-matching domain Ω_s is a contracted domain of Ω such that the distance to Γ_w is at least 2 mm. Figure 2.4(c) shows the example of Ω_s in the cylinder. Furthermore, the optimisation parameters are $\alpha = 0.15$, $\beta = 10^{-4}$ and $\beta_1 = 10^{-8}$. Figures 2.5(a), 2.5(b) and 2.5(c) illustrate the norms of the flow matching, $\|\tilde{\boldsymbol{u}}^t - \boldsymbol{u}\|_{\text{fm}}$, the control, $\|\boldsymbol{g}\|_{\text{co}}$, and the surface gradient of the control, $\|\nabla_{\boldsymbol{\tau}}\, \boldsymbol{g}\|_{\text{sg}}$, which are defined as follows:

$$\|\tilde{\boldsymbol{u}}^t - \boldsymbol{u}\|_{\text{fm}} = \left(\frac{100}{\underset{\Omega}{\text{avr}}|\tilde{\boldsymbol{u}}^t|} \right) \sqrt{\frac{1}{V_\Omega} \int_\Omega |\tilde{\boldsymbol{u}}^t - \boldsymbol{u}|^2 \, d\Omega} \quad , \tag{2.4.6}$$

$$\|\boldsymbol{g}\|_{\text{co}} = \left(\frac{1}{\underset{\Gamma_i}{\text{avr}}|\tilde{\boldsymbol{u}}^t|} \right) \sqrt{\frac{1}{A_{\Gamma_i}} \int_{\Gamma_i} |\boldsymbol{g}|^2 \, d\Gamma} \quad , \tag{2.4.7}$$

$$\|\nabla_{\boldsymbol{\tau}}\, \boldsymbol{g}\|_{\text{sg}} = \left(\frac{1}{\underset{\Gamma_i}{\text{avr}}|\nabla_{\boldsymbol{\tau}} \tilde{\boldsymbol{u}}^t|} \right) \sqrt{\frac{1}{A_{\Gamma_i}} \int_{\Gamma_i} |\nabla_{\boldsymbol{\tau}} \boldsymbol{g}|^2 \, d\Gamma} \quad , \tag{2.4.8}$$

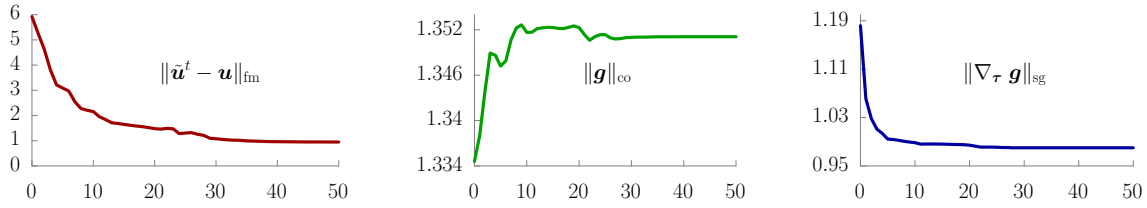

(a) Flow-matching (b) Control (c) Control's surface gradient

Figure 2.5: The norms from optimisation with parameters $\alpha = 0.15$, $\beta = 10^{-4}$, $\beta_1 = 10^{-8}$. The norms are plotted against the number of iterations in the horizontal axis.

where V_Ω is the volume of the entire domain, and A_{Γ_i} is the area at inlet. The norms are normalised against the average magnitude of target velocity or its surface gradient.

As shown in figure 2.5(b), the norm of the control, $\|\boldsymbol{g}\|_{\text{co}}$, rapidly grows at the beginning, forcing the noisy vectors towards their desired position and remaining almost constant after a while. In figure 2.5(c), the sudden decrease in the norm of velocity surface gradient, $\|\nabla_{\boldsymbol{\tau}}\, \boldsymbol{g}\|_{\text{sg}}$, shows the denoising process at inlet. Once a good approximation is reached, the velocities at inlet are only being adjusted slightly during the rest of iterations. This is continued until a sufficient flow matching is achieved in the entire domain as illustrated in figure 2.5(a).

Let us now focus on the results in the domain close to the cylinder wall. To confirm the presented results also with respect to the accuracy in near-wall regions, we calculated both the root mean square error, $\text{nRMSE}_d = \text{nRMSE}_d(\boldsymbol{u}_{\mathbf{ext}}, \boldsymbol{u}_{\mathbf{opt}})$, and the flow direction error, $\text{FDE}_d = \text{FDE}_d(\boldsymbol{u}_{\mathbf{ext}}, \boldsymbol{u}_{\mathbf{opt}})$, defined by

$$\text{nRMSE}_d(\boldsymbol{u}_t, \boldsymbol{u}_c) = \left(\frac{100}{\underset{E_d}{\text{avr}}|\boldsymbol{u}_t|} \right) \sqrt{\frac{1}{V_d} \int_{E_d} |\boldsymbol{u}_t - \boldsymbol{u}_c|^2 \, dE_d} \quad , \tag{2.4.9}$$

$$\text{FDE}_d(\boldsymbol{u}_t, \boldsymbol{u}_c) = \sqrt{\frac{1}{V_d} \int_{E_d} \left(1 - \frac{\boldsymbol{u}_t \cdot \boldsymbol{u}_c}{|\boldsymbol{u}_t||\boldsymbol{u}_c|} \right)^2 dE_d} \quad . \tag{2.4.10}$$

In what follows, the subscript d stands for the evaluation of the error within the contracted subdomain $E_d \subset \Omega$ with volume V_d, which is defined as

$$E_d = \{\, \boldsymbol{x} \in \Omega \;\mid\; \exists \boldsymbol{y} \in \Gamma_w,\, \|\boldsymbol{x} - \boldsymbol{y}\| < d \text{ (mm)} \,\} \quad . \tag{2.4.11}$$

That is, we want to evaluate the errors in the domain E_d at near-wall regions (this domain is not meant to be included in the flow-matching domain Ω_s), where the nearest Euclidean distance of all points in E_d is at most d mm apart from the wall, Γ_w. Figure 2.4(c) features the contracted domain in the cylinder. It should be noted that both errors, (2.4.9) and (2.4.10), are evaluated between the exact solution, $\boldsymbol{u}_{\mathbf{ext}}$, and the results obtained from the proposed optimisation strategy, $\boldsymbol{u}_{\mathbf{opt}}$, in the contracted region E_d. In addition, the error nRMSE_d is

normalised against the average velocity magnitude of the observations in E_d.

For $d = 2$, the initial errors $\mathrm{nRMSE}_2(\boldsymbol{u}_{\mathbf{ext}}, \boldsymbol{u}_{\mathbf{snr}})$ and $\mathrm{FDE}_2(\boldsymbol{u}_{\mathbf{ext}}, \boldsymbol{u}_{\mathbf{snr}})$ between the exact solution, $\boldsymbol{u}_{\mathbf{ext}}$, and noisy observations, $\boldsymbol{u}_{\mathbf{snr}}$, were 26.65% and $1.1 \cdot 10^{-2}$ respectively. After optimal control, the root mean square error, as a percentage of the average velocity magnitude, was reduced to $\mathrm{nRMSE}_2(\boldsymbol{u}_{\mathbf{ext}}, \boldsymbol{u}_{\mathbf{opt}}) = 3.53\%$, and the flow direction error was $\mathrm{FDE}_2(\boldsymbol{u}_{\mathbf{ext}}, \boldsymbol{u}_{\mathbf{opt}}) = 3.5 \cdot 10^{-5}$.

Sensitivity Analyses with Respect to Changes in Optimisation Parameters

There have been some reported discussions in the literature concerning the choice of the optimisation parameters for related control problems. In Lee [Lee11], the penalisation value was set to 10^{-10} for a Neumann boundary control and validations were performed for a flow problem in a 2-D square case. In Guerra *et al.* [Gue14], a 2-D geometry for a stenosed vessel was considered, where the parameter related to the surface gradient term (denoted as β_1 in this work) was set to 10^x with $x \in \{-5, -4, -2, -1, 0, 1\}$, whereas the other optimisation parameters were maintained constant. Further works have also reported on the choice of regularisation parameters in the related field [Fur98; DEl12a; Ber14; Gue15].

In this work, the parameter α was chosen on a trial and error basis. It was observed that α should be between 0.15 and 0.5 depending on the data being used. Values larger than 0.5 enforce a more stringent flow-matching and the optimiser already stops at very early stages of the iterations. For values smaller than 0.15, the optimiser needs more iterations because the flow-matching term is more relaxed. In the latter case, as expected, the final solution gets further away from the observations.

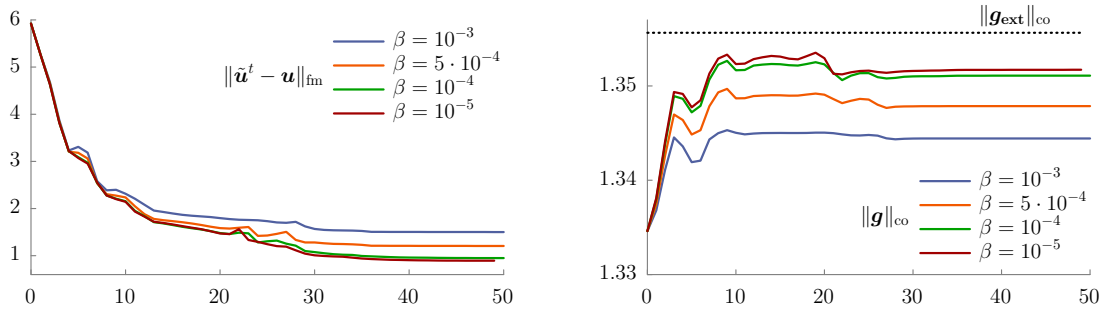

(a) Norms of flow-matching

(b) Norms of control

Figure 2.6: Alteration in norms of flow-matching and control (solid lines in (a) and (b)) with respect to changes in β, along with the constant norm of exact solution (dashed line in (b)), where $\alpha = 0.15$ and $\beta_1 = 10^{-8}$. The norms are plotted against the number of iterations in the horizontal axis.

The differences in the response as a consequence of changes in the optimisation parameters, β and β_1, were examined in this work for the 3D case. First of all, we set $\alpha = 0.15$, which was experimentally found to be an appropriate parameter for this use case and was then used

in the sensitivity analyses with respect to changes in β and β_1. Second, we kept $\beta_1 = 10^{-8}$ fixed and modified β. Figures 2.6(a) and 2.6(b) show the flow-matching norm, $\|\tilde{\boldsymbol{u}}^t - \boldsymbol{u}\|_{\text{fm}}$, and the control norm, $\|\boldsymbol{g}\|_{\text{co}}$, for different β values. In addition, figure 2.6(b) also contains the constant norm, $\|\boldsymbol{g}_{\text{ext}}\|_{\text{co}}$, of the exact solution. We observed that for larger values, such as $\beta > 10^{-4}$, there was not enough control and the flow-matching was poor. This is because the objective function was rapidly penalised at early stages of the optimisation, where the optimiser needs larger controls in order to reduce the error. For smaller β values, however, there was no hard penalization and the optimiser could apply larger controls as illustrated in figure 2.6(b). In general, the values 10^{-4} and 10^{-5} delivered satisfactory results and $\beta = 10^{-5}$ was observed to be the best choice.

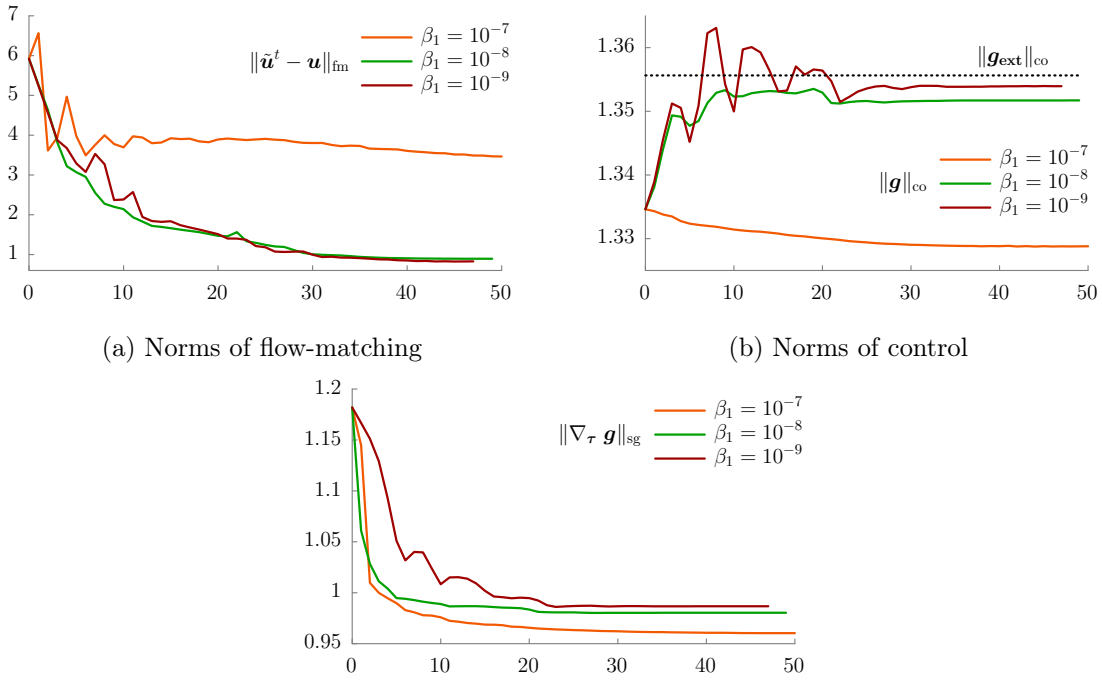

(a) Norms of flow-matching

(b) Norms of control

(c) Norms of control surface gradient

Figure 2.7: Alteration in norms of flow-matching and control (solid lines in (a), (b) and (c)) with respect to changes in β_1, along with the constant norm of exact solution (dashed line in (b)), where $\alpha = 0.15$ and $\beta = 10^{-5}$. The norms are plotted against the number of iterations in the horizontal axis.

Furthermore, we fixed β at 10^{-5} and ran the optimiser with β_1 set to 10^{-7}, 10^{-8} and 10^{-9} (smaller values of β_1 rendered unacceptable solutions because of the lack of smoothing effect on noisy measurements). For different β_1 values, figures 2.7(a) and 2.7(c) show the plots for the flow-matching norm, $\|\tilde{\boldsymbol{u}}^t - \boldsymbol{u}\|_{\text{fm}}$, and the surface gradient norm, $\|\nabla_{\boldsymbol{\tau}}\, \boldsymbol{g}\|_{\text{sg}}$. Let us first analyse the results between the values 10^{-7} and 10^{-8} for β_1. It can be observed that the norm of the surface gradient is further reduced for $\beta_1 = 10^{-8}$ over the successive iterations,

and better flow matching is achieved. This can be explained by further investigation of the control norm, $\|\boldsymbol{g}\|_{\text{co}}$, along with the norm of the exact solution, $\|\boldsymbol{g}_{\mathbf{ext}}\|_{\text{co}}$, in figure 2.7(b). We can observe that there is not enough control for $\beta_1 = 10^{-7}$. This shows that even if we are able to remove the noise at the inlet (which is explained by the reduction in the value of the surface gradient for $\beta_1 = 10^{-7}$), the controls are small and hence the velocities cannot be properly optimised. Second, let us consider the results for β_1 values of 10^{-8} and 10^{-9}. Figure 2.7(a) shows that the flow-matching is achieved with an almost equally good quality. In figure 2.7(b), however, fluctuations along the iterations can be observed in the norm of controls for $\beta_1 = 10^{-9}$. In addition, figure 2.7(c) shows that the fluctuations also have an effect on the norm of the surface gradient, which is not as greatly reduced in early iterations as is the case for $\beta_1 = 10^{-8}$.

Finally, our interpretations are also confirmed quantitatively in near-wall regions. Table 2.1 summarises the results from the sensitivity analysis comparing the root mean square errors, nRMSE_2, and the flow direction errors, FDE_2, for varied optimisation parameters. Our conclusion is that a value of $\beta_1 = 10^{-8}$ delivers sufficiently accurate results, and this value will be used hereafter.

(β, β_1)	$(10^{-3}, 10^{-8})$	$(10^{-4}, 10^{-8})$	$(10^{-5}, 10^{-8})$	$(10^{-5}, 10^{-9})$	$(10^{-5}, 10^{-7})$
$\mathbf{nRMSE}_2$	4.53 %	3.53 %	3.41 %	3.68 %	8.40 %
$\mathbf{FDE}_2$	$7.0 \cdot 10^{-5}$	$3.5 \cdot 10^{-5}$	$2.8 \cdot 10^{-5}$	$1.4 \cdot 10^{-4}$	$4.8 \cdot 10^{-5}$

Table 2.1: Dimensionless root mean square ($\text{nRMSE}_2(\boldsymbol{u}_{\mathbf{ext}}, \boldsymbol{u}_{\mathbf{opt}})$) and flow direction ($\text{FDE}_2(\boldsymbol{u}_{\mathbf{ext}}, \boldsymbol{u}_{\mathbf{opt}})$) errors measured within the near-wall (2 mm) domain (E_2).

2.4.5 Optimisation with Noisy Solution as Target Flow

So far, we have been able to validate the proposed approach using an analytical solution. Actually, an exact solution is not available or cannot be provided by measurements or experiments. Here, the performance of the optimisation framework was evaluated considering the artificially generated noisy measurements as the target flow. That is, we set $\tilde{\boldsymbol{u}}^t = \boldsymbol{u}_{\mathbf{snr}}$ in the objective function (2.2.5). In order to avoid lack of control, the initial flow field was low-pass filtered with a cutoff frequency of 0.5. The low-pass filtered field is just a smoothed version of the measurements. It reduces the edge contents and results in a blurred image. The degree of the smoothness is proportional to the chosen cut-off frequency. Use of a blurred (smoothed or low-pass filtered) version of the measurements as initial condition is not mandatory. However, the motivation behind using it was the fact that, preferably, the flow-matching term in the objective function (first-term in (2.2.5)) should not result in a null value at the very first iteration (e.g. by the application of the measurements directly as initial condition). Moreover, the choice of such an initial condition enables us to start with a guess close (in some sense) to the

measurements (as opposed to the case of, e.g., potentially applying a zero-field as initial condition) to avoid a significantly large number of iterations until the convergence. The resulting flow field is represented by $\boldsymbol{u}_{\mathbf{lpf}}$ in Ω, and algorithm 1 was executed with the input parameters $(\boldsymbol{u}_{\mathbf{lpf}}, \boldsymbol{g}_{\mathbf{lpf}}, \boldsymbol{u}_{\mathbf{snr}})$, where $\boldsymbol{g}_{\mathbf{lpf}} = \boldsymbol{u}_{\mathbf{lpf}}$ on Γ_i. Motivated by the findings of the previous section, parameters β and β_1 were set to 10^{-5} and 10^{-8} respectively. Flow matching was performed in Ω_2. The parameter α was adjusted to 0.5 for this set-up. Under these conditions, the quantitative results yielded 4.85% and $5.8 \cdot 10^{-5}$ for nRMSE_2 and FDE_2 respectively.

Sensitivity Analyses with Respect to Changes in the Flow-Matching Domain

As described in section 2.4.3, the addition of artificial noise follows the same procedure at each location in the flow domain and does not depend on the velocity magnitudes. Hence, the near-wall regions with very low velocities contain almost no relevant signal, but mostly noise. Moreover, near-wall regions also contain further errors due to partial volume effects. Hence, such locations should rather be avoided in the flow-matching domain, Ω_s. Therefore, a further contraction in the subdomain was considered in addition. To account for it, we performed a sensitivity analysis with respect to changes in the flow-matching domain Ω_s using the same parameters as specified above. The simulations were performed with s varying from 1.5 to 4.

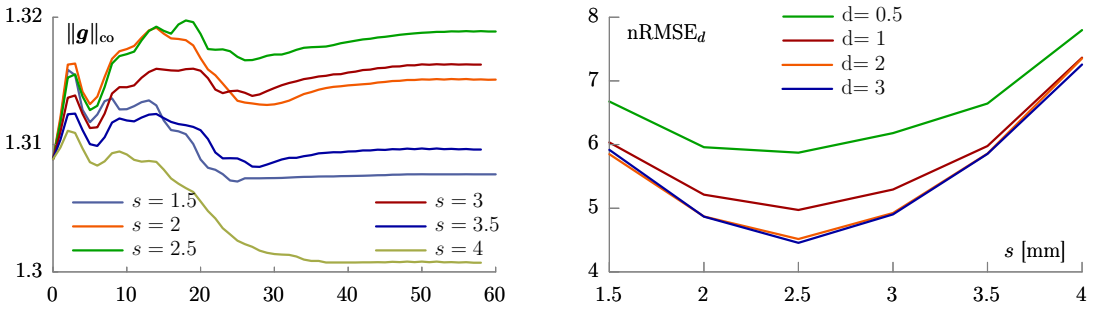

(a) Norms of control for different s

(b) Errors plotted against s for different d

Figure 2.8: Illustration of (a): norms of control with respect to changes in flow-matching domain, Ω_s, and (b): root mean square errors at near-wall domain, E_d. The norms are plotted against the number of iterations in the horizontal axis.

The norms of the control are shown in figure 2.8(a) for different values of s. It can be observed that larger controls result for $s = 2.5$. The magnitude of the control $\boldsymbol{g}$ decreases if Ω_s is further contracted or extended. This can be also confirmed by nRMSE_d in figure 2.8(b), where the x-axis represents s. The errors in near-wall regions are further decreased for $s = 2.5$. In addition, figure 2.8(b) illustrates the error measurements (y-axis) for different values of d represented in different colours. In all cases, the optimisation framework delivers accurate results at locations of the domain close to the lateral boundary (the wall). This is especially interesting for the evaluation of WSSs, some of the most important parameters for diagnostic

purposes in the cardiovascular field. Table 2.2 summarises the results in the near-wall domains E_d defined for different distances from the wall (with d values ranging from 3 mm to 0.5 mm) for varying flow-matching domains Ω_s with s varying from 1.5 to 4. For example, for a flow-matching domain $\Omega_{2.5}$, which is 2.5 mm apart from the wall Γ_w, the root mean square error nRMSE_2, which is evaluated within 2 mm distance of the wall Γ_w, is 4.52%, and $\text{FDE}_{0.5}$ is $5.0 \cdot 10^{-5}$. This improves the accuracy in comparison with the results from the previous section, where the flow-matching domain was chosen to be Ω_2. For $s \geq 3$, the accuracy also starts to drop. This is a remarkable finding for the choice of Ω_s. In addition, contraction of the flow-matching domain also in the longitudinal direction (e.g. exclusion of the locations at and near the inlet/outlet boundaries from Ω_s) also results in loss of accuracy. In this case, the errors (achieved from the contractions in the longitudinal direction) increase to a similar extent to that, given in table 2.2 for the radial contractions. In general, the flow-matching domain should be constructed such that it contains almost all available information about the flow field in the luminal area (reaching from inlet to outlet), whereas it should avoid using the information at near-wall locations. We have shown that it is a very good choice to keep the flow-matching domain 2.5 (mm) away from the vessel wall for this case.

s	1.5	2	2.5	3	3.5	4
$\mathbf{nRMSE}_3$	5.92 %	4.86 %	4.46 %	4.90 %	5.85 %	7.26 %
$\mathbf{FDE}_3$	$6.1 \cdot 10^{-5}$	$4.8 \cdot 10^{-5}$	$4.2 \cdot 10^{-5}$	$4.4 \cdot 10^{-5}$	$4.7 \cdot 10^{-5}$	$5.0 \cdot 10^{-5}$
$\mathbf{nRMSE}_2$	5.85 %	4.85 %	4.52 %	4.92 %	5.86 %	7.35 %
$\mathbf{FDE}_2$	$7.5 \cdot 10^{-5}$	$5.8 \cdot 10^{-5}$	$5.0 \cdot 10^{-5}$	$5.3 \cdot 10^{-5}$	$5.7 \cdot 10^{-5}$	$6.0 \cdot 10^{-5}$
$\mathbf{nRMSE}_1$	6.03 %	5.18 %	4.97 %	5.29 %	5.98 %	7.36 %
$\mathbf{FDE}_1$	$1.0 \cdot 10^{-4}$	$7.9 \cdot 10^{-5}$	$6.9 \cdot 10^{-5}$	$7.3 \cdot 10^{-5}$	$7.7 \cdot 10^{-5}$	$8.2 \cdot 10^{-5}$
$\mathbf{nRMSE}_{0.5}$	6.68 %	5.93 %	5.88 %	6.18 %	6.64 %	7.80 %
$\mathbf{FDE}_{0.5}$	$1.3 \cdot 10^{-4}$	$1.0 \cdot 10^{-4}$	$8.7 \cdot 10^{-5}$	$9.2 \cdot 10^{-5}$	$9.8 \cdot 10^{-5}$	$1.0 \cdot 10^{-4}$

Table 2.2: Dimensionless root mean square, $\text{nRMSE}_d(\boldsymbol{u}_{\mathbf{ext}}, \boldsymbol{u}_{\mathbf{opt}})$, and flow direction, $\text{FDE}_d(\boldsymbol{u}_{\mathbf{ext}}, \boldsymbol{u}_{\mathbf{opt}})$, errors measured within the near-wall (d (mm)) domain, E_d, for varying flow-matching domains, Ω_s (s (mm) apart from the wall).

Comparison against classical CFD

Finally, the ability of the boundary control approach to reconstruct the measured flow field in the entire domain was compared against the results delivered from the classical CFD strategy. The latter is based on a single forward simulation, with Dirichlet BCs, applied (as usual) at the inlet boundary. Then, the classical CFD implies solution of the problem $\mathscr{P}_{\text{sta}}$, as stated

by the variational equations (2.2.20)-(2.2.21)-(2.2.22). Thus, using the initial guess $\boldsymbol{u}_{\mathbf{snr}}$ and the BC $\boldsymbol{u} = \boldsymbol{u}_{\mathbf{snr}}$ on Γ_i, the linearised problem $\mathscr{P}^{\text{lin}}_{\text{sta}}(\boldsymbol{u}_{\mathbf{snr}}, \boldsymbol{g}_{\mathbf{snr}})$ was solved with $\boldsymbol{g}_{\mathbf{snr}} = \boldsymbol{u}_{\mathbf{snr}}$ on Γ_i, iteratively until convergence was achieved. In what follows, the solution obtained from a classical CFD approach will be denoted as $\boldsymbol{u}_{\mathbf{cfd}}$. Motivated by the conclusion in section 2.4.5, the optimisation algorithm was employed to deliver the optimised solution $\boldsymbol{u}_{\mathbf{opt}}$ for parameters $\alpha = 0.5$, $\beta = 10^{-5}$, $\beta_1 = 10^{-8}$ and $s = 2.5$. Furthermore, the optimisation was performed against the noisy solution as target flow and initialised with the low-pass filtered flow field, as described in section 2.4.5. We want to emphasise that, during the optimisation procedure, there is no knowledge available about the exact solution at all.

Flow patterns were first inspected visually to obtain a qualitative interpretation. Figure 2.9 shows the flow patterns in the domain, obtained from the artificially generated noisy measurements, $\boldsymbol{u}_{\mathbf{snr}}$, the computations via the traditional CFD method, $\boldsymbol{u}_{\mathbf{cfd}}$, the computations from the proposed optimisation framework, $\boldsymbol{u}_{\mathbf{opt}}$, and finally the exact solution, $\boldsymbol{u}_{\mathbf{ext}}$. It can be appreciated that the optimised flow is the one that better resembles the exact solution. Especially, it features excellent qualitative agreement with the exact solution at the inlet boundary and at locations near to the inlet, where the traditional CFD approach suffers from inaccuracy, caused by the noisy BC.

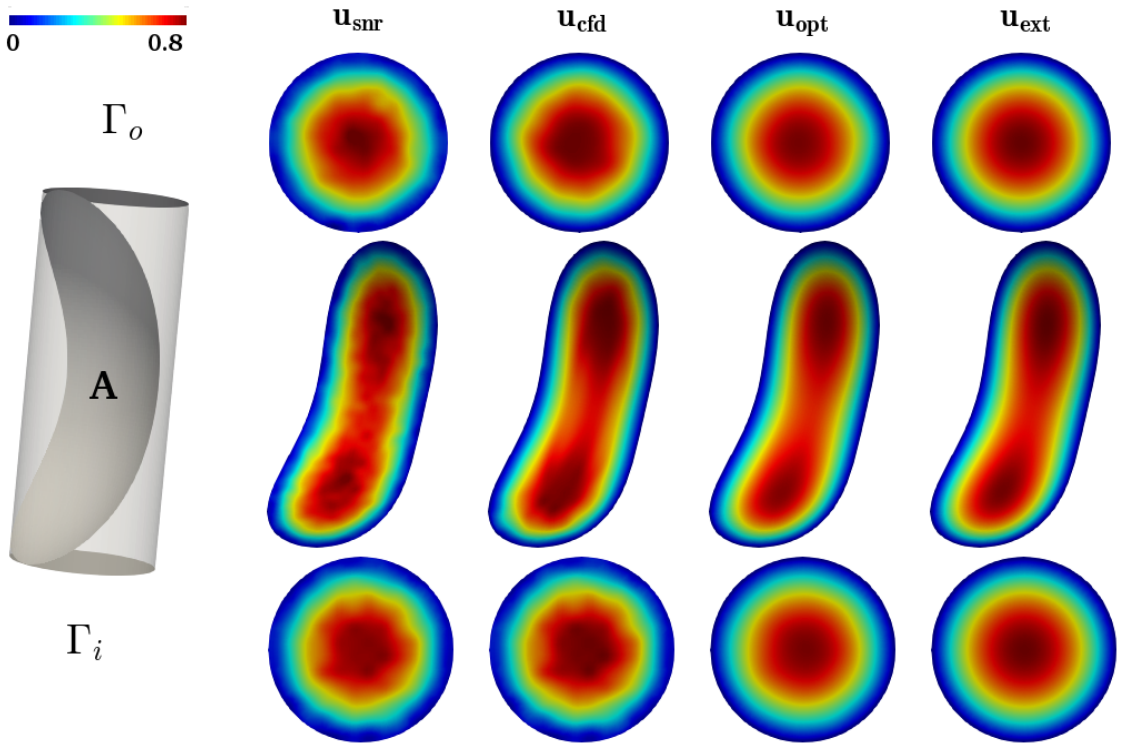

Figure 2.9: Flow patterns for fields $\boldsymbol{u}_{\mathbf{snr}}$, $\boldsymbol{u}_{\mathbf{cfd}}$, $\boldsymbol{u}_{\mathbf{opt}}$ and $\boldsymbol{u}_{\mathbf{ext}}$ illustrated at inlet (Γ_i), outlet (Γ_o) and at a curved surface (A) immersed in the lumen. The colours representing the velocity magnitudes are scaled to the range of 0 and 0.8, whereas the corresponding maximum velocities were $|\boldsymbol{u}_{\mathbf{snr}}|_{max} \approx 0.853$, $|\boldsymbol{u}_{\mathbf{cfd}}|_{max} \approx 0.777$, $|\boldsymbol{u}_{\mathbf{opt}}|_{max} \approx 0.784$ and $|\boldsymbol{u}_{\mathbf{ext}}|_{max} \approx 0.8$.

To confirm the previous qualitative assessment, the simulation results from both the classical CFD and the control approaches were quantitatively compared against the exact solution. First, we evaluated nRMSE_d and FDE_d in the near-wall domain E_d for the values $d = 2$, $d = 1$ and $d = 0.5$. Table 2.3 shows that the velocity field was reconstructed by the optimisation algorithm much more accurately at the wall boundary, in comparison with the classical CFD approach. Noisy observations, $\boldsymbol{u}_{\mathbf{snr}}$, deliver almost no relevant signal near the boundaries, which can be observed by the huge and increasing errors for decreasing d values. In contrast, however, nRMSE_d is more rapidly decreased when applying the optimisation algorithm to obtain $\boldsymbol{u}_{\mathbf{opt}}$, as we get closer to wall boundary. This shows the feasibility of the optimisation approach, especially for its accuracy at the boundaries. Furthermore, the flow direction errors are decreased to a much greater extent for the optimised flow in comparison with the classical CFD method. This also shows clearly that the noise at the inlet boundary is removed to a great extent by the application of the control. In addition, it can be seen that FDE_d is not further decreased as we get close to the walls. This is expected, since the optimisation procedure itself is a trade-off between decreasing the flow-matching errors in terms of magnitudes and the flow direction errors based on the surface gradient. Both terms are included in the objective function and are affected by the choice of parameters.

$\boldsymbol{x} = \boldsymbol{u}_{\mathbf{ext}}$	$\mathbf{nRMSE_d}(\boldsymbol{x}, \boldsymbol{y})$			$\mathbf{FDE_d}(\boldsymbol{x}, \boldsymbol{y})$		
	$\boldsymbol{y} = \boldsymbol{u}_{\mathbf{snr}}$	$\boldsymbol{y} = \boldsymbol{u}_{\mathbf{cfd}}$	$\boldsymbol{y} = \boldsymbol{u}_{\mathbf{opt}}$	$\boldsymbol{y} = \boldsymbol{u}_{\mathbf{snr}}$	$\boldsymbol{y} = \boldsymbol{u}_{\mathbf{cfd}}$	$\boldsymbol{y} = \boldsymbol{u}_{\mathbf{opt}}$
$d = 2$	26.65 %	8.36 %	4.52 %	$1.1 \cdot 10^{-2}$	$1.2 \cdot 10^{-3}$	$5.0 \cdot 10^{-5}$
$d = 1$	61.30 %	11.79 %	4.97 %	$1.6 \cdot 10^{-2}$	$1.7 \cdot 10^{-3}$	$6.9 \cdot 10^{-5}$
$d = 0.5$	139.82 %	17.93 %	5.88 %	$2.1 \cdot 10^{-2}$	$2.1 \cdot 10^{-3}$	$8.7 \cdot 10^{-5}$

Table 2.3: Dimensionless root mean square ($\text{nRMSE}_d(\boldsymbol{u}_{\mathbf{ext}}, \boldsymbol{y})$) and flow direction ($\text{FDE}_d(\boldsymbol{u}_{\mathbf{ext}}, \boldsymbol{y})$) errors for $\boldsymbol{y} = \{\, \boldsymbol{u}_{\mathbf{snr}}, \boldsymbol{u}_{\mathbf{cfd}}, \boldsymbol{u}_{\mathbf{opt}} \,\}$, measured within the near-wall (d mm) domain (E_d). Optimisation is performed using measurements in the flow-matching volume (Ω_s), which is ($s = 2.5$ mm) apart from the wall boundary.

In addition, the computational cost of both the classical CFD method and the optimisation procedure were evaluated and compared in terms of wall clock time (or execution time). The classical CFD method using the SIMPLE algorithm required approximately 100 iterations to reach the solution, and its execution time was 34 seconds. In turn, the data assimilation process required approximately 50 iterations with an execution time of 82 seconds.

Finally, the maximum and average WSSs were calculated from the numerical results based on the classical CFD and the optimisation procedure. These quantities were then compared against the WSSs computed with the analytical solution. Figure 2.10 shows the box plots to characterise the discrepancies between the WSS fields obtained from the exact solution, $\boldsymbol{u}_{\mathbf{ext}}$, and from both the computations with classical CFD, $\boldsymbol{u}_{\mathbf{cfd}}$, and the optimised solution, $\boldsymbol{u}_{\mathbf{opt}}$.

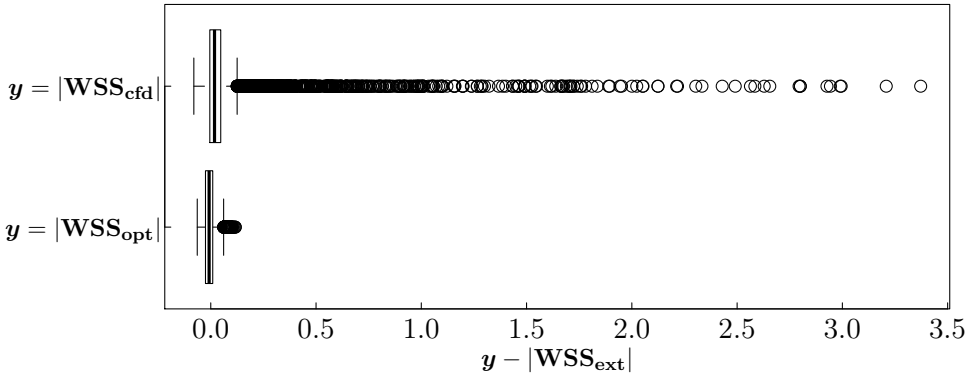

Figure 2.10: Box plot illustrating the differences ($|\mathbf{WSS_{cfd}}| - |\mathbf{WSS_{ext}}|$) and ($|\mathbf{WSS_{opt}}| - |\mathbf{WSS_{ext}}|$) in the horizontal axis, where the labels $\mathbf{WSS_{cfd}}$, $\mathbf{WSS_{opt}}$ and $\mathbf{WSS_{ext}}$ represent the wall shear stresses corresponding to the fields $\boldsymbol{u}_{\mathbf{cfd}}$, $\boldsymbol{u}_{\mathbf{opt}}$ and $\boldsymbol{u}_{\mathbf{ext}}$ respectively.

2.5 Data Assimilation in a Realistic Geometry

The proposed approach was tested for the flow-matching control problem in a more realistic geometry obtained from a glass replica of a human aorta. The geometry consisted of aortic root, ascending aorta, aortic arch without branches and descending aorta as illustrated in figure 2.1(a). First, a validation study was performed on the aorta based on a manufactured solution used as the ground truth. The results from the assimilation procedure and the classical CFD method were quantitatively compared against the ground truth (available reference solution). Second, real flow data were gathered from the flow MRI scans to investigate the performance of the solvers in real case scenarios. The optimisation results were first qualitatively compared with measured data. In addition, and since there is no reference solution available in this case, the results were quantitatively compared against the results when using the classical CFD method prescribing Dirichlet BCs. The discrepancies between the solution obtained from the data assimilation approach and the CFD solution were also examined in contrast to the discrepancies encountered between both solutions in the manufactured scenario involving the aorta phantom geometry. Furthermore, a sensitivity analysis with respect to changes in the initial guess flow field was analysed and discussed in the real case scenario. Finally, the proposed approach was tested under flow conditions with increasing Reynolds numbers ranging approximately from 1 200 up to 2 100. For the highest Reynolds number, a mesh sensitivity analysis was also carried out.

2.5.1 Experimental Setup

The in-vitro experiment was prepared in a scanner and control room including a 3T MRI scanner from Philips. The glass replica, covered by a six-element cardiac coil, was placed in the scanner and connected to a centrifugal pump (in the control room) with a maximum pressure of 3.9 bar. The connection was made with a PVC tubing of total length 20 m with

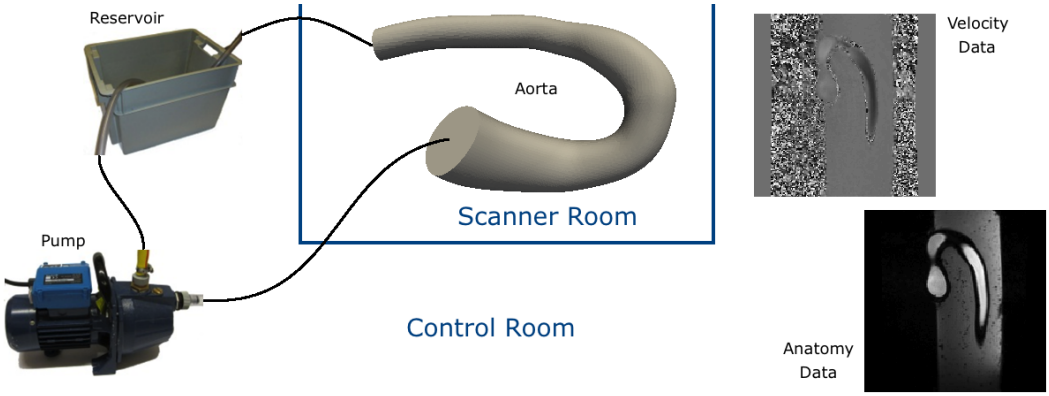

Figure 2.11: Experimental setup for the glass replica of human aorta.

an inner diameter of 19 mm. The inlet and outlet of the pipe were connected to a reservoir in the control room creating an open circuit. A ball bearing valve was placed 1.5 m downstream of the tube and was used to control the flow rate. Figure 2.11 shows the experimental setup.

The reservoir was filled with a mixture of 24 liter H_2O, 40 gr carboxymethyl cellulose carboxymethyl (CMC) and 10 gr sulfate. The aim of the CMC medium was to increase the viscosity of the fluid to an approximately similar level to blood viscosity. On the other hand, the sulfate acted as a contrast agent to increase the signal magnitude. For a temperature of 27° C, the mixture featured a viscosity of 3.5 cP.

Three different image acquisitions were performed to obtain data with increasing Reynolds numbers. The maximum velocities in the obtained data were $1.06, 1.71$ and 2.26 m/s and the corresponding Reynolds numbers were $1\,223, 1\,860$ and $2\,105$ respectively. Thus, the flow rates were controlled such that the obtained data contained laminar flow. We highlight the fact that the flow model does not account for turbulence and consideration of turbulence models is matter of current research.

A 3-D spoiled gradient-echo sequence with flow encoding gradients was used for the flow-MRI acquisitions. The eddy-current induced background phase was compensated by application of linear phase correction. The acquisition parameters were chosen as flip angle 10^o, time of repetition and echo (TR/TE) 2.6/4.87 ms, field of view (FOV) $[244 \times 244 \times 62]$ mm^3 and voxel size $[1.4 \times 1.4 \times 1.5]$ mm^3. Furthermore, considering the increasing Reynolds numbers of the measured data, the corresponding VENCs were chosen as $120, 200$ and 260 cm/s respectively.

2.5.2 On the imaging resolution of flow-MRI

Flow MRI is primarily limited by the SNR, and the scanning parameters must be chosen such that there is a trade-off between the acquisition time and the spatial/temporal resolution. Besides, in patient specific cardiovascular acquisition, the optimised scan parameters must take the variability of the cardiac period and/or shifts in patient position into account and

ensure that physiological artifacts, such as respiratory motion, are minimised [Cal16a]. A substantial decrease in the voxel size is not clinically feasible. This would increase the scan time (potentially by several hours) which is not practical for a patient lying inside of the MRI device. At the same time, this will result in a lower number of protons within the voxel substantially decreased in size. Hence, the gathered signal will suffer more from noise and the SNR will decrease.

Under normal clinical conditions, it is currently possible to acquire a 4-D flow dataset of the heart and major vessels in approximately 10 minutes at a spatial resolution of 2.5 mm (isotropic) with a temporal resolution of 30-40 ms [Cal16b]. In the work reported by Bock *et al.* [Boc11], the authors used 2.1 mm isotropic voxel size for patient specific measurement of the aorta. In addition, Cibis *et al.* [Cib15] performed MRI scans of patients with Fontan circulation using a spatial resolution of $1.9-2.5\times1.9-2.5\times2.2-3.3$ mm^3 with coverage of the heart and large arteries. Further studies have performed personalised acquisitions of the ventricle based on a cross-sectional resolution between 1.9 and 2.5 mm [Vec16; Lar17]. However, the most recent studies of flow MRI have investigated the feasibility towards even higher resolutions with clinically feasible scan times. Schmitter *et al.* [Sch16] reported increased imaging resolutions, such of 1.2 mm isotropic voxel size, using accelerated protocols.

Following the clinical feasibility and considering the recent improvements in terms of the resolution, we have therefore used an approximately 1.5 mm isotropic voxel size in our acquisitions, which finally resulted in a resolution of $1.4\times1.4\times1.5$ mm^3.

2.5.3 Data Preprocessing

For the generation of the computational mesh, the aortic replica was first segmented (see figure 2.12(a)) from the anatomical data and then smoothed (see figure 2.12(b)). Thereafter, the available exact geometry (see figure 2.12(d)), with the region of interest that defines the inlet/outlet boundaries highlighted, was registered with the smoothed geometry as shown in figure 2.12(c). Section 2.3.2 provides more details about the applied segmentation and registration. Finally, a hexahedral mesh with 122 079 cells was created using the exact geometry cut by the region of interest. Moreover, two additional hexahedral meshes with approximately 750 000 and 1 370 000 cells were created for a mesh sensitivity analysis. Figures 2.12(e)–2.12(f) illustrate the computational mesh with 122 079 cells.

Having generated the computational mesh, the measured flow data followed into the preprocessing pipeline as described in section 2.3. In what follows, $\boldsymbol{u}_{\mathbf{snr}}^{Re}$ with $Re = \{\,1\,223, 1\,860, 2\,105\,\}$ will represent the flow fields derived after the application of divergence-free space projection: that is, after solving the problem $\mathscr{P}_\perp$ described by the equation (2.3.4).

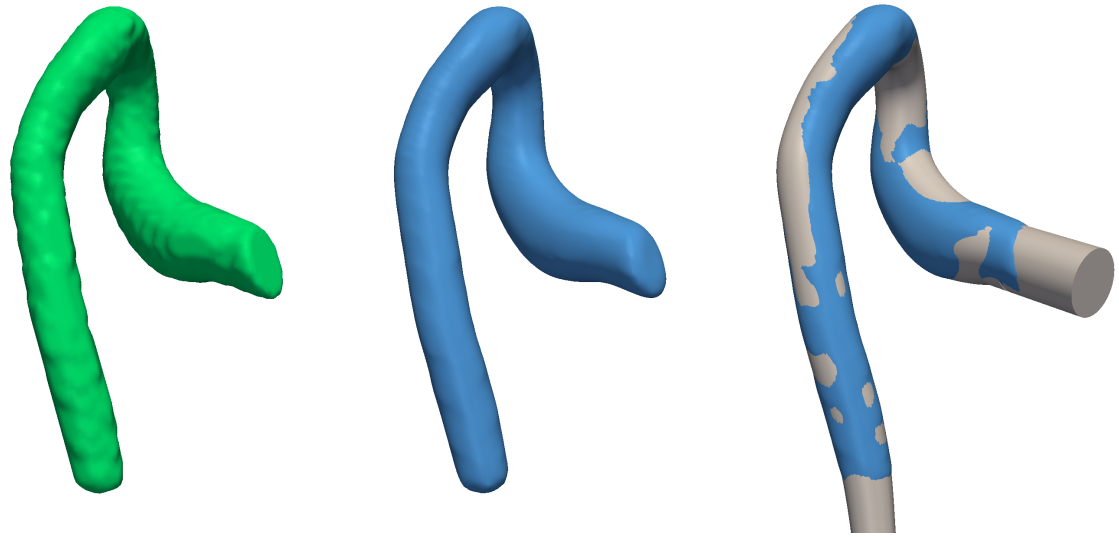

(a) Segmented Domain (b) Smoothed Domain (c) Registration

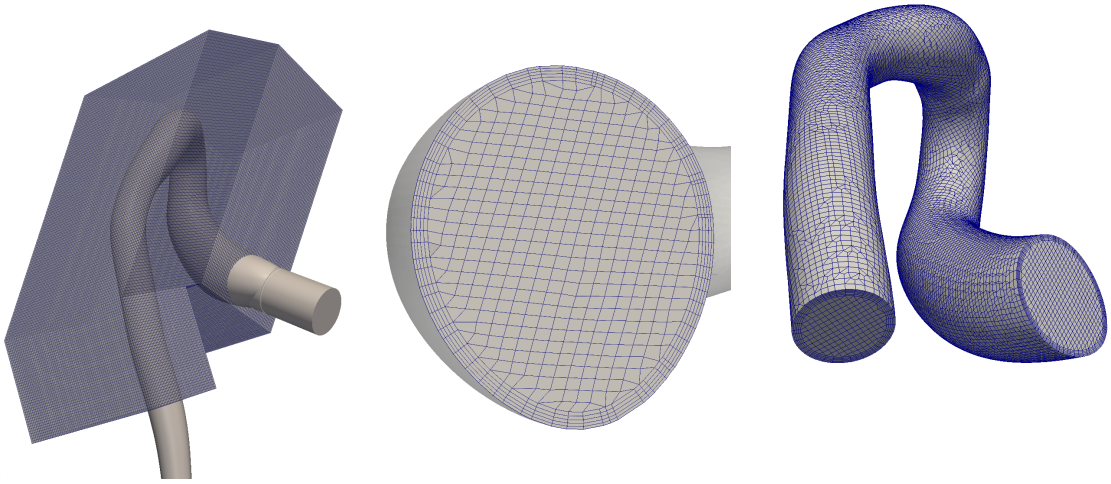

(d) Exact Geometry (e) Mesh at Inlet (f) Mesh in Domain

Figure 2.12: Mesh generation from exact geometry (d) including the segmentation (a) of domain from anatomical data, smoothing (b) and registration (c) of exact geometry with the smoothed geometry. A region of interest (d) defines the computational domain for which a hexahedral mesh with 122 079 cells is created (e), (f).

2.5.4 Validation of the Data Assimilation based on a Reference Solution in the Aorta

Due to the noisy nature of flow MRI scans, there exists no true reference solution in such real case scenarios. This makes it difficult to provide an argumentation about the value of the assimilation procedure. Therefore, we have first generated a numerical reference solution on the computational mesh to validate the approach on the aortic geometry. The numerical solution will be considered as the ground truth in the quantification of the errors.

The generation of the ground truth was based on a forward steady-state flow simulation

with an idealised BC at the inlet, resembling a parabolic flow profile. A kinematic viscosity of 4.5 cP was considered and the resulting flow field with $Re = 1\,780$ had a maximum flow velocity of 0.8 m/s. In what follows, the ground truth will be denoted as $\boldsymbol{u}_{\mathbf{ext}}$. An artificial noise with an isotropic VENC of 0.9 m/s and an SNR of 10 (see section 2.4.3 for more details) was added on top of the ground truth. Following our usual notation, the noisy flow field (after being decomposed into its divergence-free components) will be denoted as $\boldsymbol{u}_{\mathbf{snr}}$.

To analyse the performance of the optimisation procedure for such a realistic aortic geometry, the assimilation was first performed against the ground truth. Thus, the target flow in the objective function (2.2.5) was set as $\tilde{\boldsymbol{u}}^t = \boldsymbol{u}_{\mathbf{ext}}$ and the algorithm 1 was executed with the input parameters $(\boldsymbol{u}_{\mathbf{snr}}, \boldsymbol{g}_{\mathbf{snr}}, \boldsymbol{u}_{\mathbf{ext}})$, where $\boldsymbol{g}_{\mathbf{snr}} = \boldsymbol{u}_{\mathbf{snr}}$ on Γ_i. The resulting flow field will be denoted as $\boldsymbol{u}_{\mathbf{opt}}^{\mathbf{ext}}$ in the sense of the solution of data assimilation performed against the ground truth. A quantitative comparison of the assimilation procedure against the ground truth in terms of $\mathrm{nRMSE}_d(\boldsymbol{u}_{\mathbf{opt}}^{\mathbf{ext}}, \boldsymbol{u}_{\mathbf{ext}})$ yielded 0.8, 1.1 and 1.4% for $d = 2, 1, 0.5$ respectively. The errors are relatively small, which shows the feasibility of the approach in a complex geometry.

However, in a real case scenario, a ground truth is usually not available and the assimilation cannot be performed against an already known solution. In order to avoid any bias in favour of one of the solvers (the optimisation or the classical CFD), the assimilation was additionally performed against the noisy solution. That is, algorithm 1 was additionally executed with the input parameters $(\boldsymbol{u}_{\mathbf{snr}}, \boldsymbol{g}_{\mathbf{snr}}, \boldsymbol{u}_{\mathbf{snr}})$. In this case, the resulting flow field will be denoted as $\boldsymbol{u}_{\mathbf{opt}}^{\mathbf{snr}}$. The classical CFD method was also executed, where the Dirichlet BC and the initial conditions were set to the flow field $\boldsymbol{u}_{\mathbf{snr}}$, and the resulting flow field will be denoted as $\boldsymbol{u}_{\mathbf{cfd}}$. In this sense, both solvers have no information whatsoever about the ground truth prior starting the simulations. The errors, $\mathrm{nRMSE}_1(\boldsymbol{x}, \boldsymbol{u}_{\mathbf{ext}})$ and $\mathrm{FDE}_1(\boldsymbol{x}, \boldsymbol{u}_{\mathbf{ext}})$, evaluated for $\boldsymbol{x} = \{\boldsymbol{u}_{\mathbf{cfd}}, , \boldsymbol{u}_{\mathbf{opt}}^{\mathbf{snr}}, \boldsymbol{u}_{\mathbf{opt}}^{\mathbf{ext}}\}$, were 6.81 %, 4.77 %, 1.10 % and 0.12, 0.10, 0.01 respectively. This reveals that the optimisation solver still performs better in comparison with the classical CFD method, even if one assimilates against a noisy solution. The rather small difference between 6.81 % and 4.77 % can be explained by the fact that the errors within the close proximity of the wall are evaluated in the entire domain. However, it should be noted that in this aorta geometry the size of the entire domain is much larger than the region where the BCs have a true impact. Indeed, after the development length, whatever the BC is, the solution tends to become that of a fully developed flow, and the errors are masked by this fact. In other words, as the optimisation controls the velocities at the inlet, it is expected that more representative errors are encountered near the inlet location. To investigate this, the same errors were evaluated near the aortic root inlet (within a close proximity of the inlet), instead of taking the entire domain. Let us define a further contracted subdomain domain $E_d^s \subset E_d \subset \Omega$ as follows:

$$E_d^s = \{\, \boldsymbol{x} \in \Omega \mid \exists \boldsymbol{y} \in \Gamma_w,\, \exists \boldsymbol{z} \in \Gamma_i,\, \|\boldsymbol{x} - \boldsymbol{y}\| < d \text{ (mm)} \wedge \|\boldsymbol{x} - \boldsymbol{z}\| < s \text{ (cm)} \,\} \quad . \tag{2.5.1}$$

Correspondingly, the errors nRMSE_d^4 and FDE_d^4 are defined within 4 cm proximity of the inlet in the corresponding domain E_d^4 and will be used in the rest of this work. The errors, $\text{nRMSE}_1^4(\boldsymbol{x}, \boldsymbol{u}_{\mathbf{ext}})$ and $\text{FDE}_1^4(\boldsymbol{x}, \boldsymbol{u}_{\mathbf{ext}})$, evaluated for $\boldsymbol{x} = \{\boldsymbol{u}_{\mathbf{cfd}}, , \boldsymbol{u}_{\mathbf{opt}}^{\mathbf{snr}}, \boldsymbol{u}_{\mathbf{opt}}^{\mathbf{ext}}\}$, were 34 %, 17 %, 5 % and 0.22, 0.18, 0.03 respectively. These results are also summarized on the left-hand side of table 2.4. It can be observed that, compared with the results of the classical CFD method, there is a significant improvement in the outcome provided by the assimilation (against the noisy solution) in the close proximity of the inlet. This is a remarkable finding for the improvement of the flow field, especially at the aortic root, which is a place where flow disturbances can easily lead to pathological modifications of the arterial wall.

$\boldsymbol{x} \longrightarrow$	$\boldsymbol{u}_{\mathbf{cfd}}$	$\boldsymbol{u}_{\mathbf{opt}}^{\mathbf{snr}}$	$\boldsymbol{u}_{\mathbf{opt}}^{\mathbf{ext}}$	$\mathbf{d} \longrightarrow$	**2**	**1**	**0.5**
$\mathbf{nRMSE}_{\mathbf{1}}^{\mathbf{4}}(\boldsymbol{x}, \boldsymbol{u}_{\mathbf{ext}})$	34 %	17 %	5 %	$\mathbf{nRMSE}_{\mathbf{d}}^{\mathbf{4}}(\boldsymbol{u}_{\mathbf{cfd}}, \boldsymbol{u}_{\mathbf{opt}}^{\mathbf{snr}})$	23 %	30 %	34 %
$\mathbf{FDE}_{\mathbf{1}}^{\mathbf{4}}(\boldsymbol{x}, \boldsymbol{u}_{\mathbf{ext}})$	0.22	0.18	0.03	$\mathbf{FDE}_{\mathbf{d}}^{\mathbf{4}}(\boldsymbol{u}_{\mathbf{cfd}}, \boldsymbol{u}_{\mathbf{opt}}^{\mathbf{snr}})$	0.11	0.13	0.15

Table 2.4: On the left: Root mean square errors ($\text{nRMSE}_1^4(\boldsymbol{x}, \boldsymbol{u}_{\mathbf{ext}})$) and flow direction errors ($\text{FDE}_1^4(\boldsymbol{x}, \boldsymbol{u}_{\mathbf{ext}})$) evaluated within the close proximity (4 cm) of the inlet and the near-wall (1 mm) domain (E_1^4) , where $\boldsymbol{x} = \{\, \boldsymbol{u}_{\mathbf{cfd}}, \boldsymbol{u}_{\mathbf{opt}}^{\mathbf{snr}}, \boldsymbol{u}_{\mathbf{opt}}^{\mathbf{ext}} \,\}$. On the right: The corresponding errors ($\text{nRMSE}_d^4(\boldsymbol{u}_{\mathbf{cfd}}, \boldsymbol{u}_{\mathbf{opt}}^{\mathbf{snr}})$) and ($\text{FDE}_d^4(\boldsymbol{u}_{\mathbf{cfd}}, \boldsymbol{u}_{\mathbf{opt}}^{\mathbf{snr}})$) reporting the difference between the solutions of the classical CFD, $\boldsymbol{u}_{\mathbf{cfd}}$, and the data assimilation procedure, $\boldsymbol{u}_{\mathbf{opt}}^{\mathbf{snr}}$.

Furthermore, we examined the difference between the solutions of the optimisation, $\boldsymbol{u}_{\mathbf{opt}}^{\mathbf{snr}}$, and the classical CFD, $\boldsymbol{u}_{\mathbf{cfd}}$. The errors, $\text{nRMSE}_1^4(\boldsymbol{u}_{\mathbf{cfd}}, \boldsymbol{u}_{\mathbf{opt}}^{\mathbf{snr}})$ and $\text{FDE}_1^4(\boldsymbol{u}_{\mathbf{cfd}}, \boldsymbol{u}_{\mathbf{opt}}^{\mathbf{snr}})$, were 23 %, 30 %, 34 % and 0.11, 0.13, 0.15 respectively. Thus, the difference between the data assimilation procedure and the classical CFD method is approximately 30 %, which clearly emphasizes to what extent the data assimilation is able to alter the CFD solution. The right-hand side of table 2.4 summarises the differences between the two solvers.

2.5.5 Numerical Results Based on Flow MRI Scans

Numerical results are first presented for $Re = 1\,223$ based on the flow data denoted by $\boldsymbol{u}_{\mathbf{snr}}^{Re}$ (as described in section 2.5.3), mapped on the computational mesh domain and projected into a divergence-free space. In what follows, $\boldsymbol{u}_{\mathbf{snr}}^{Re}$ with $Re = 1\,223$ will be simply denoted as $\boldsymbol{u}_{\mathbf{snr}}$. The target flow in the objective function (2.2.5) was set as $\tilde{\boldsymbol{u}}^t = \boldsymbol{u}_{\mathbf{snr}}$. A low-pass filtered flow field of this target flow with a cut-off frequency of 4 was used as the initial guess, which will be denoted as $(\boldsymbol{u})_0 = \boldsymbol{u}_{\mathbf{lpf}}^{4.0}$. The frequency was chosen such that the flow field, being low-pass filtered, was not oversmoothed and remained close to the actual target field. The maximum magnitude of low-pass filtered flow data was 0.98 m/s, whereas for the target flow it was 1.06 m/s. Flow matching was performed in Ω_s with $s = 2.5$ and the parameters were $\beta = 10^{-5}$, $\beta_1 = 10^{-6}$ and $\alpha = 0.25$. That is, algorithm 1 was executed in the domain as represented in figure 2.1(a) with the input parameters $(\boldsymbol{u}_{\mathbf{lpf}}^{4.0}, \boldsymbol{g}_{\mathbf{lpf}}^{4.0}, \boldsymbol{u}_{\mathbf{snr}})$, where $\boldsymbol{g}_{\mathbf{lpf}}^{4.0} = \boldsymbol{u}_{\mathbf{lpf}}^{4.0}$ on Γ_i.

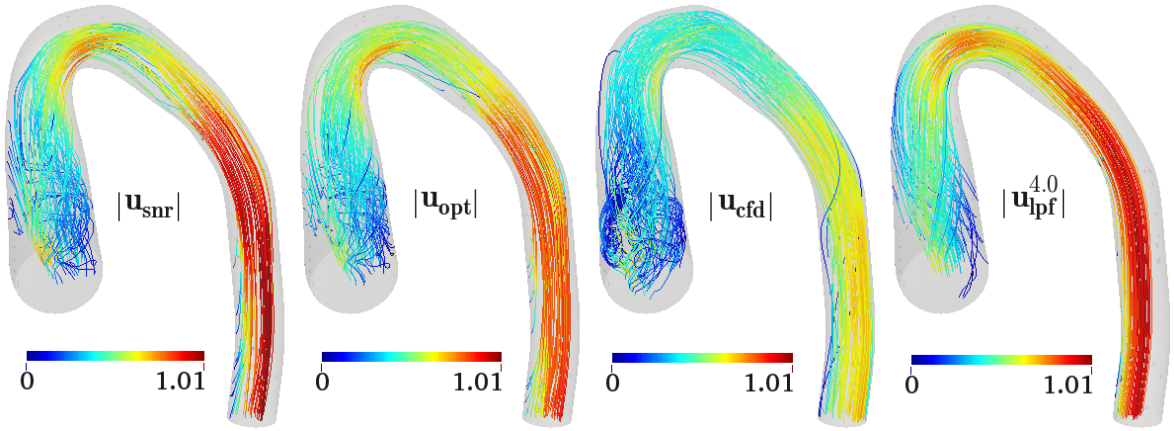

Figure 2.13: Streamlines for the magnitudes of different velocity fields. The observations considered here are the measured data with $Re = 1\,223$

The flow patterns predicted by the optimisation algorithm and the classical CFD method were first qualitatively compared against the measured data by visual inspection. Figure 2.13 shows the streamlines corresponding to the different velocity fields. Figure 2.14 illustrates the magnitude of the velocity field in a cross-sectional slice covering part of the ascending and descending aorta. Furthermore, figure 2.15 highlights the warps of the velocity profile for a set of transverse slices. It can be observed that the measured velocity field, $\boldsymbol{u}_{\mathbf{snr}}$, and the optimised solution, $\boldsymbol{u}_{\mathbf{opt}}$, are reasonably similar, whereas the flow field predicted by the classical CFD method is relatively far from the measured data.

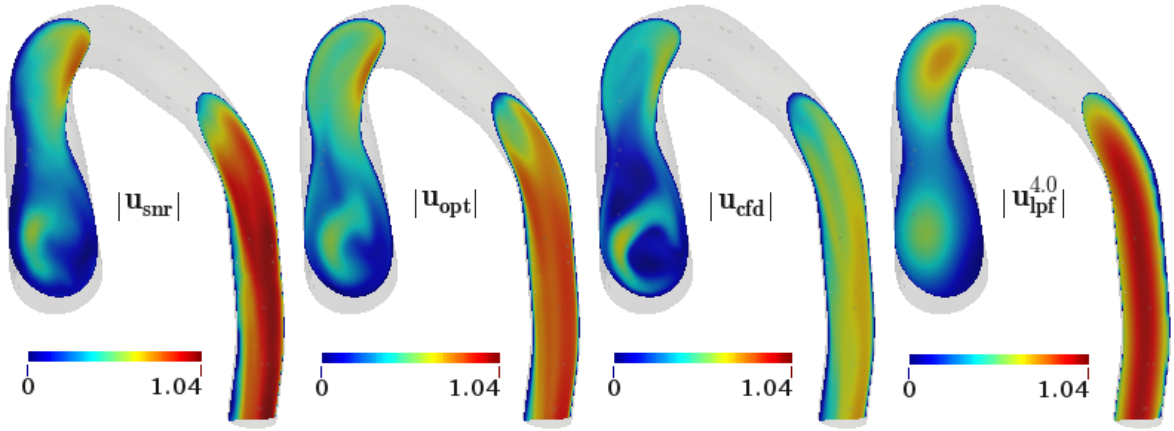

Figure 2.14: Velocity magnitude in a cross-sectional slice for the different velocity fields. The observations considered here are the measured data with $Re = 1\,223$

The results were also analysed quantitatively. However, the observations have a noisy nature and there is no true reference solution available in this case. Respectively, we evaluated the errors between $\boldsymbol{u}_{\mathbf{cfd}}$ and $\boldsymbol{u}_{\mathbf{opt}}$ to quantify the differences of the flow fields predicted by the classical CFD method and the optimisation strategy. The flow matching norm, $\|\boldsymbol{u}_{\mathbf{opt}} - \boldsymbol{u}_{\mathbf{cfd}}\|_{\mathrm{fm}}$,

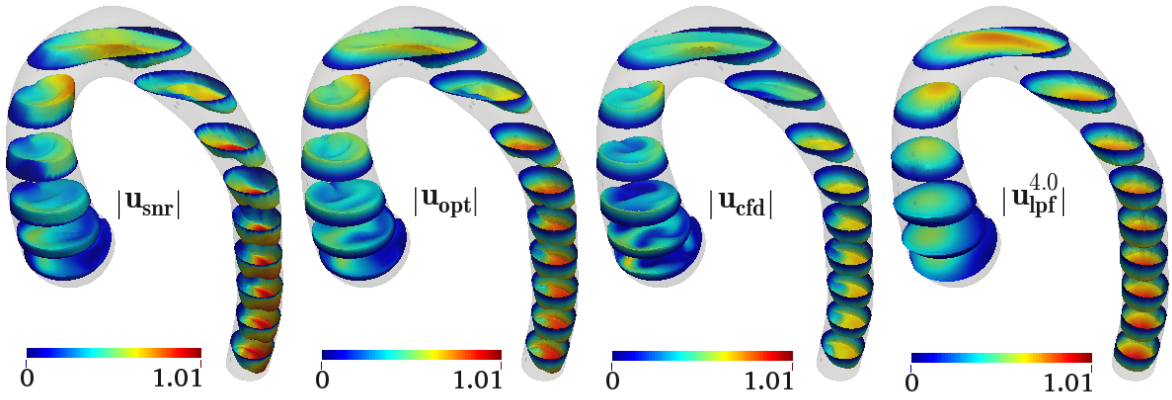

Figure 2.15: Warps of the magnitudes of velocity fields at a set of cross-sectional slices. The observations considered here are the measured data with $Re = 1\,223$

resulted in 39% of the average velocity magnitude of optimised solution. In addition, the errors were evaluated at the aortic root in the close proximity of the inlet. For $d = \{2, 1, 0.5\}$, the errors $\text{nRMSE}^4_d(\boldsymbol{u}_{\mathbf{cfd}}, \boldsymbol{u}_{\mathbf{opt}})$ were 46 %, 51 % and 60 % respectively. This shows that the differences in the predictions grow on getting closer to the wall. The normalised difference, $\|\mathbf{WSS}_{\mathbf{cfd}} - \mathbf{WSS}_{\mathbf{opt}}\|$ (see equations (2.5.2) and (2.5.3)), between the WSS fields corresponding to the velocity fields $\boldsymbol{u}_{\mathbf{cfd}}$ and $\boldsymbol{u}_{\mathbf{opt}}$ was 43.72%. Furthermore, figures 2.16(a) and 2.16(b) illustrate the magnitudes of the WSS fields, $\mathbf{WSS}_{\mathbf{cfd}}$ and $\mathbf{WSS}_{\mathbf{opt}}$, and figure 2.16(c) shows their normalised difference field. In addition, figures 2.17(a) and 2.17(b) illustrate the pressure fields of the predictions from the classical CFD method and from the optimisation strategy respectively, whereas figure 2.17(c) shows their normalised difference field.

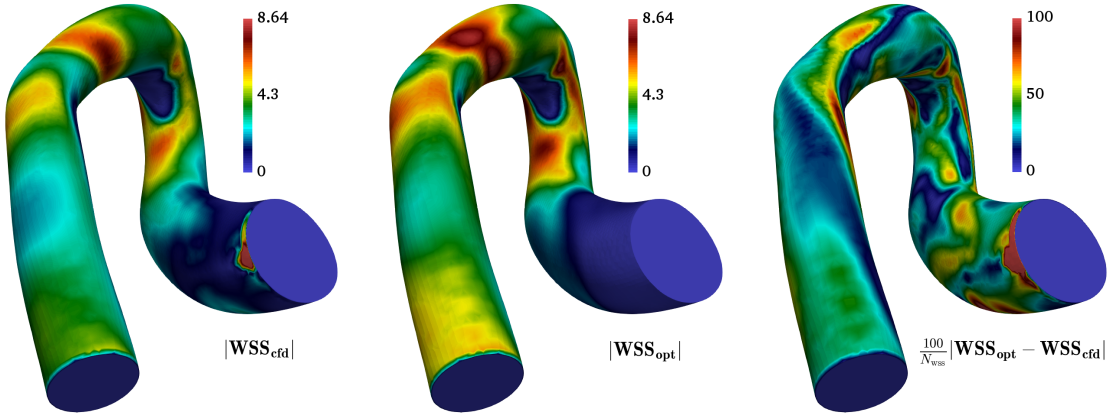

(a) (b) (c)

Figure 2.16: (a), (b): Magnitude fields of wall shear stresses, $|\mathbf{WSS}_{\mathbf{cfd}}|$ and $|\mathbf{WSS}_{\mathbf{opt}}|$, corresponding to the velocity fields $\boldsymbol{u}_{\mathbf{cfd}}$ and $\boldsymbol{u}_{\mathbf{opt}}$, (c): Normalised difference field, $\frac{100}{N_{\text{wss}}}|\mathbf{WSS}_{\mathbf{opt}} - \mathbf{WSS}_{\mathbf{cfd}}|$ on Γ_w, where N_{wss} is as described in (2.5.2). The observations considered here are the measured data with $Re = 1\,223$

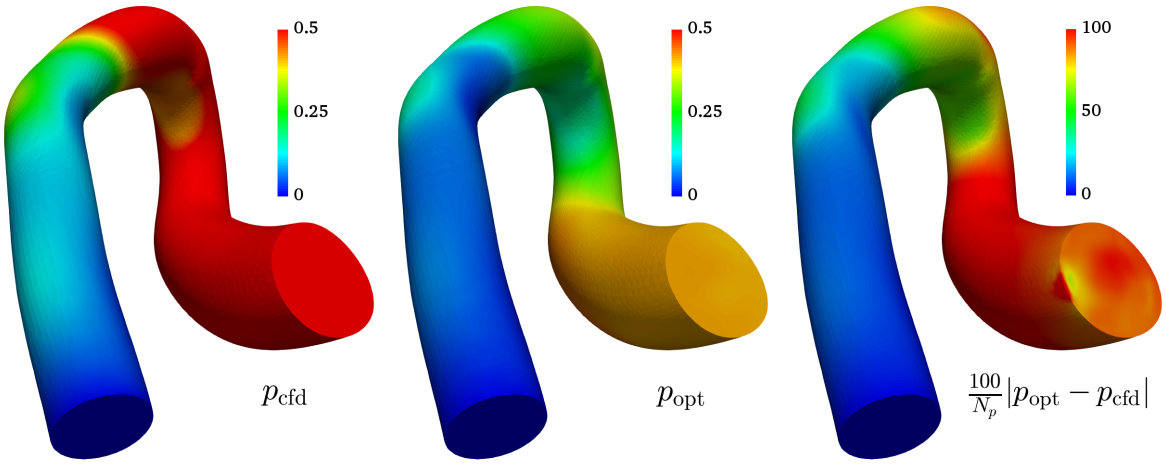

(a) (b) (c)

Figure 2.17: Pressure fields corresponding to predictions from classical CFD, p_{cfd}, from optimisation strategy, p_{opt}, and their normalised difference field, $\frac{100}{N_p}|p_{\text{opt}} - p_{\text{cfd}}|$ on $\partial\Omega$, where $N_p = \frac{1}{V_\Omega}\int_\Omega \frac{|p_{\text{opt}}+p_{\text{cfd}}|}{2}\,d\Omega$. The observations considered here are the measured data with $Re = 1\,223$.

Notably, the better qualitative agreement between the observations and the optimised solution, and quantitatively significant differences between the optimised solution and the predictions from classical CFD, support the fact that the optimisation delivers a better solution when compared with the classical CFD approach. The improvement in the flow field is especially emphasised at the aortic root, which is one of the most important clinically relevant locations for the development of pathological alterations of the anatomical structures underlying the arterial wall.

$$N_{\text{wss}} = \frac{1}{A_{\Gamma_w}}\int_{\Gamma_w} \frac{|\mathbf{WSS_{opt}} + \mathbf{WSS_{cfd}}|}{2}\,d\Gamma \quad , \tag{2.5.2}$$

$$\|\mathbf{WSS_{opt}} - \mathbf{WSS_{cfd}}\| = \frac{100}{N_{\text{wss}}}\sqrt{\frac{1}{A_{\Gamma_w}}\int_{\Gamma_w} |\mathbf{WSS_{opt}} - \mathbf{WSS_{cfd}}|^2\,d\Gamma} \quad . \tag{2.5.3}$$

2.5.6 Sensitivity with Respect to Changes in Initial Guess

To analyse the performance and sensitivity of the optimisation strategy with respect to changes in the initial guess, different flow fields were generated from the observations to be applied as the initial guess flow. The observations were low-pass filtered with different cutoff frequencies 3.5 and 4.5, denoted as $\boldsymbol{u}_{\mathbf{lpf}}^{3.5}$ and $\boldsymbol{u}_{\mathbf{lpf}}^{4.5}$ respectively. The maximum velocity magnitude was 1.16 m/s for the flow field $\boldsymbol{u}_{\mathbf{lpf}}^{3.5}$, whereas it was 0.84 m/s for $\boldsymbol{u}_{\mathbf{lpf}}^{4.5}$. In addition, a zero flow field, $\boldsymbol{u}_0$, was prepared as the initial guess, that is $\boldsymbol{u}_0 = \mathbf{0}$ in Ω. Under the same conditions as in section 2.5.5, algorithm 1 was executed with input parameters $(\boldsymbol{u}_{\mathbf{lpf}}^{3.5}, \boldsymbol{g}_{\mathbf{lpf}}^{3.5}, \boldsymbol{u}_{\mathbf{snr}})$, $(\boldsymbol{u}_{\mathbf{lpf}}^{4.5}, \boldsymbol{g}_{\mathbf{lpf}}^{4.5}, \boldsymbol{u}_{\mathbf{snr}})$,

$(\boldsymbol{u}_{\mathbf{snr}}, \boldsymbol{g}_{\mathbf{snr}}, \boldsymbol{u}_{\mathbf{snr}})$ and $(\boldsymbol{u}_0, \boldsymbol{g}_{\mathbf{snr}}, \boldsymbol{u}_{\mathbf{snr}})$, where $\boldsymbol{g}^{3.5}_{\mathbf{lpf}} = \boldsymbol{u}^{3.5}_{\mathbf{lpf}}$, $\boldsymbol{g}^{4.5}_{\mathbf{lpf}} = \boldsymbol{u}^{4.5}_{\mathbf{lpf}}$ and $\boldsymbol{g}_{\mathbf{snr}} = \boldsymbol{u}_{\mathbf{snr}}$ on Γ_i correspondingly.

Visual inspection revealed no remarkable differences in the final optimised velocity fields. Table 2.5 shows the flow-matching norms, the averaged WSS and the number of iterations for the optimisation starting with initial conditions $\boldsymbol{u}_{\mathbf{snr}}$, $\boldsymbol{u}_0$, $\boldsymbol{u}^{3.5}_{\mathbf{lpf}}$, $\boldsymbol{u}^{4.0}_{\mathbf{lpf}}$ and $\boldsymbol{u}^{4.5}_{\mathbf{lpf}}$ respectively. The numerical experiments with modified initial guesses provide clear evidence that, for the steady-state problem, the data assimilation algorithm is converging to the unique solution of the problem regardless of the initial solution provided. Both the qualitative and the quantitative results indicate that there were no significant changes in the solution with respect to changes in the initial guess provided to the optimisation algorithm. However, the number of iterations to reach convergence was rather sensitive to this initial guess.

Init. Guess	$(\boldsymbol{u})_0 = \boldsymbol{u}_{\mathbf{snr}}$	$(\boldsymbol{u})_0 = \boldsymbol{u}_0$	$(\boldsymbol{u})_0 = \boldsymbol{u}^{3.5}_{\mathbf{lpf}}$	$(\boldsymbol{u})_0 = \boldsymbol{u}^{4.0}_{\mathbf{lpf}}$	$(\boldsymbol{u})_0 = \boldsymbol{u}^{4.5}_{\mathbf{lpf}}$
Numb. Iters.	955	854	640	492	251
$\|\tilde{\boldsymbol{u}}^t - \boldsymbol{u}\|_{\mathrm{fm}}$	37.17 %	37.01 %	37.03 %	36.84 %	36.91 %
avr($\|\mathbf{WSS}_{\mathbf{opt}}\|$)	2.83	2.85	2.85	2.87	2.88

Table 2.5: Results of optimised solutions (number of iterations, flow-matching norm and average WSS) for different initial guesses $\boldsymbol{u}_{\mathbf{snr}}$, $\boldsymbol{u}_0$, $\boldsymbol{u}^{3.5}_{\mathbf{lpf}}$, $\boldsymbol{u}^{4.0}_{\mathbf{lpf}}$ and $\boldsymbol{u}^{4.5}_{\mathbf{lpf}}$.

2.5.7 Data assimilation for different Reynolds numbers

In what follows, the measured and preprocessed data will now be denoted as $\boldsymbol{u}^{Re}_{\mathbf{snr}}$ representing the flow fields with different Reynolds numbers, as described in section 2.5.1. Using the available data with increasing flow rates and setting the initial guesses to $\mathbf{0}$, algorithm 1 was executed with the input parameters $(\mathbf{0}, \boldsymbol{g}^{Re}_{\mathbf{snr}}, \boldsymbol{u}^{Re}_{\mathbf{snr}})$, where $\boldsymbol{g}^{Re}_{\mathbf{snr}} = \boldsymbol{u}^{Re}_{\mathbf{snr}}$ on Γ_i and $Re = \{\,1\,223, 1\,860, 2\,105\,\}$. The results are summarised in table 2.6. It can be observed that the errors between the solutions predicted by the classical CFD and the optimised flow grow for increasing Reynolds number and they grow more when getting closer to the wall, which is also consistent with the corresponding validations in table 2.4 of section 2.5.4.

For the observed data with $Re = 2\,105$, the flow field is almost in a transitional region. Therefore, we additionally performed a mesh analysis for the computations relying on the flow field $\boldsymbol{u}^{2105}_{\mathbf{snr}}$. The consistency of the assimilation on two different additional meshes with 750 000 and 1 370 000 cells was examined. Table 2.6 additionally summarises the errors for the different meshes.In general, it can observed that the flow field predicted by the classical CFD method diverges by approximately 50% from the solution provided by the optimised flow.

$\boldsymbol{x} = \boldsymbol{u}_{\mathbf{cfd}}$, $\boldsymbol{y} = \boldsymbol{u}_{\mathbf{opt}}$	$\mathbf{nRMSE}_{\mathbf{2}}^{\mathbf{4}}(\boldsymbol{x}, \boldsymbol{y})$	$\mathbf{nRMSE}_{\mathbf{1}}^{\mathbf{4}}(\boldsymbol{x}, \boldsymbol{y})$	$\mathbf{nRMSE}_{\mathbf{0.5}}^{\mathbf{4}}(\boldsymbol{x}, \boldsymbol{y})$
$Re = 1\,223$, cells: 122K	46 %	51 %	60 %
$Re = 1\,860$, cells: 122K	49 %	58 %	66 %
$Re = 2\,105$, cells: 122K	64 %	73 %	80 %
$Re = 2\,105$, cells: 750K	53 %	58 %	69 %
$Re = 2\,105$, cells: 1 370K	46 %	49 %	61 %

Table 2.6: Root mean square errors ($\mathrm{nRMSE}_d^4(\boldsymbol{u}_{\mathbf{cfd}}, \boldsymbol{u}_{\mathbf{opt}})$) and flow direction errors ($\mathrm{FDE}_d^4(\boldsymbol{u}_{\mathbf{cfd}}, \boldsymbol{u}_{\mathbf{opt}})$) evaluated within the close proximity (4 cm) of the inlet and the near-wall (d mm) domain (E_d^4) for different Re numbers, where $d = \{2, 1, 0.5\}$.

2.6 Conclusion

In this work, an optimise-then-discretise approach was developed for the flow control problem using 4-D flow MRI data in the context of computational hemodynamics. The methodology was validated against an analytical solution as well as against experimental MRI measurements performed in a glass replica of a human aorta.

The proposed control algorithm was analysed in detail in order to assess the capabilities of the methodology to reconstruct blood flow in near-wall regions, targeting the computation of hemodynamically relevant quantities such as the wall shear stress.

A critical aspect in the assimilation procedure is the size and location of the domain, Ω_s, where the flow-matching is performed. In general, Ω_s should be constructed such that it contains almost all available and reliable information about the flow field in the luminal area (spanning the entire domain from inlet to outlet), whereas it should avoid using the information at near-wall locations.

The method proved to deliver physically consistent flow fields with substantial reduction of noise present in the 4-D flow MRI measurements, outperforming the predictive capabilities of standard CFD approaches. The proposed approach provides a systematic strategy to improve the model predictions regarding clinically relevant hemodynamic data.

Overall, the flow control algorithm demonstrated robustness and feasibility towards reconstruction of flow fields from partial 4-D flow MRI measurements under different flow regimes with increasing Reynolds number. Reconstruction of the more complex flow structures observed in transient fluid dynamics and account for turbulence are out of the scope of the present work, and are matters of current research.

The proposed method is the groundwork for the development of a frequency-based approach for periodic flows. Therefore, this study is the first of a sequence addressing the dynamic case in the forthcoming chapters.

3 Analysis for Harmonic Approximation

The following material in present chapter is based on the books of Königsberger [Kön03; Kön06] and additionally on other books about functional analysis and spectral methods [Can88; Sax01; Mus14; Can15].

3.1 Method of Weighted Residuals

Most of the mathematical models describing a physical phenomena progressing in time can be written in the following form

$$\frac{\partial \boldsymbol{u}}{\partial t} = \boldsymbol{f}(t, \boldsymbol{u}), \tag{3.1.1}$$

where $\boldsymbol{u}$ denotes a state variable and the term $\frac{\partial \boldsymbol{u}}{\partial t}$ describes its temporal derivative. The term $\boldsymbol{f}(t, \boldsymbol{u})$ on the right hand side (RHS) usually contains spatial derivatives, non-linear terms and source terms. Naturally, the evolution equation (3.1.1) must be complemented with some boundary and initial conditions. In what follows, we will assume (without loss of generality) that the boundary conditions (BCs) are periodic in time. Further, we will require that $\boldsymbol{u}$ belongs to a Hilbert space $\mathcal{H}$, which ensures the existence of a scalar product along with an L^2-Norm for $\boldsymbol{u}$ (to be utilized in section 3.2 to perform a Fourier analysis based on this function space).

The method of weighted residuals (MWR) [Cra56] dictates the sense in which the evolution equation (3.1.1) is to be satisfied, and when a certain approximation is performed, it delivers an approximation $\tilde{\boldsymbol{u}}$ of the state variable $\boldsymbol{u}$. The MWR offers several alternatives (as reviewed by Finlayson *et al.* [Fin66]) to approximate the exact solution for the type of equations like (3.1.1). For $k = 1, 2, \ldots, n$, aforementioned approximation can be considered as being a linear combination of some (in a way appropriately chosen and known) time-dependent basis functions $\varphi_k : \mathbb{R} \to \mathbb{C}$ with certain spatially varying expansion coefficients $\boldsymbol{c}_k : \Omega \to \mathbb{C}^3$. The expansion is written as

$$\tilde{\boldsymbol{u}}(t, \boldsymbol{x}) = \sum_{k=-n}^{n} \boldsymbol{c}_k(\boldsymbol{x}) \varphi_k(t), \tag{3.1.2}$$

where $\tilde{\boldsymbol{u}}$ must satisfy prescribed boundary conditions for all possible selection of the expansion coefficients $\boldsymbol{c}_k$. The selection of basis functions φ_k defines the numerical methodology. The

choice of infinitely differentiable global polynomials leads to the so-called spectral methods [Hes07; Can07]. These are most notably the Fourier spectral methods [Che98; Bue14; Boy01], Chebyshev spectral methods [Boy01; Bré18] and Legendre spectral methods [Mad81; Lee90], which are distinguished by the choice of φ_k as trigonometric polynomials (see section 3.2), Chebyshev polynomials or Legendre polynomials, respectively. In turn, the division of the spatial domain of interest into smaller subdomains and the application of certain basis functions with compact support results in well-known numerical methods, such as finite-elements, finite-differences or finite-volumes.

The sense in which $\tilde{\boldsymbol{u}}$ satisfies the equation (3.1.1) depends upon the weighing of the residual with appropriately chosen weight functions $\varpi_k : \mathbb{R} \to \mathbb{C}$. Thus, the residual $\mathscr{R}$ will not vanish everywhere in the considered time domain. In fact, the goal is to have the quantity

$$\mathscr{R}(\tilde{\boldsymbol{u}}) = \frac{\partial \tilde{\boldsymbol{u}}}{\partial t} - \boldsymbol{f}(t, \tilde{\boldsymbol{u}}). \tag{3.1.3}$$

as small as possible, something that is expected to happen when n is increased in equation (3.1.2)). Let us consider a time domain interval $\mathbb{T} := [-\pi, \pi]$ of length 2π. The MWR follows from choosing a basis function φ_k for the field $\tilde{\boldsymbol{u}}$ and from weighting the residuals with some functions ϖ_k. Finally, it is required that the integral of the weighted residuals on $\mathbb{T}$ is nullified [Fin72]:

$$\int_{\mathbb{T}} \mathscr{R}(\tilde{\boldsymbol{u}}) \varpi_k(t) dt = \boldsymbol{0}. \tag{3.1.4}$$

There are several alternatives for the choice of the weight functions $\varpi_k(t)$. These methods can be listed as the Galerkin approach, integral and sub-domain methods, method of least squares, collocation methods and tau methods. A historical overview about these and other possible choices along with their differences from or connections to each other can be found in Finlayson *et al.* [Fin66]. In addition, a detailed list of references including the further developments of these different approaches is provided by Finlayson [Fin13].

The construction of spectral methods is not only based on the choice of basis functions φ_k as the global polynomial functions, but also on the particular choice of the weight functions $\varpi_k(t)$. The most commonly used and established spectral methods with respect to the choice of weight function $\varpi_k(t)$ are the Galerkin, tau or collocation approaches [Can88].

The spectral Galerkin approach considers infinitely differentiable polynomials as the weight functions, which are essentially the same as the basis functions. As an example, consider the trigonometric polynomials as the basis functions, thus $\varphi_k = e^{ikt}$. In this case (which is essentially the Fourier spectral method) the Galerkin approach corresponds to the application of trigonometric weight functions, $\varpi_k = \frac{1}{2\pi} e^{-ikt}$, which satisfy the orthonormality condition $\int_{\mathbb{T}} \varphi_k(t) \varpi_l(t) dt = \delta_{kl}$, where δ_{kl} is the Kronecker delta function. The Galerkin approach requires that (3.1.4) is satisfied for each weight function. In addition, usually the integration

by parts is applied and the Galerking approach ensures that each BC in the resulting set of equations is also satisfied individually. In contrast, the spectral tau methods are similar in the way of enforcing the partial differential equations, but they differ in the fact that the weight functions do not verify the BCs. This results in the necessity of introducing additional sets of equations into the system, in order to enforce the BCs [Can06].

The spectral collocation approach introduces a set of sample points (the so-called collocation points) and requires that (3.1.3) is satisfied at exactly these points [Mal85; Sun16; Gom16]. In this case, the weight functions are the Dirac delta functions correspondingly shifted at the N collocation points

$$\varpi_k(t) = \delta(t - t_j), \quad j = 1, 2, \cdots, N, \quad t_j = \frac{j2\pi}{N}$$

As a result of this, the integral expression (3.1.4) becomes

$$\int_{\mathbb{T}} \mathscr{R}(\tilde{\boldsymbol{u}})\delta(t - t_j)dt = \mathbf{0}, \quad j = 1, 2, \cdots, N \tag{3.1.5}$$

which finally results in a set of N equations

$$\left\{ \mathscr{R}(\tilde{\boldsymbol{u}}) = \mathbf{0} \right\}\Big|_{t_j}, \quad j = 1, 2, \cdots, N \tag{3.1.6}$$

A detailed review about the early developments and first uses of collocation approaches can be found in Canuto *et al.* [Can06] (Chap. 1, Sec. 1.1, Para. 4).

3.2 Fourier Analysis

Linear combinations of basic trigonometric functions, such as cosine and sine waves, posed as infinite sums are already well-known as candidate solutions to physical problems. Most notably such decomposition was reported some centuries ago by Fourier and Bernoulli. Following their findings, this field was further developed and established by many excellent mathematicians, especially Weierstrass, Cauchy and Riemann. A historical overview about these developments can be found in Bressoud [Bre06].

3.2.1 Fourier series

Decomposition of a function into linear combination of more basic functions can be best analysed in the framework of Hilbert spaces. Let $\mathcal{H} := L^2(-\pi; \pi)$ be an abstract Hilbert space, where $L^2(V) := \left\{ f : A \to \mathbb{C} \mid \int_V |f(t)|^2 dt < \infty \right\}$. Further, we define the scalar product

$$\langle a, b \rangle := \frac{1}{2\pi} \int_{-\pi}^{\pi} a(t)\overline{b(t)}dt. \tag{3.2.1}$$

For $w \in \mathcal{H}$, a norm $\|\cdot\|_2$ is induced on the space by the scalar product $\langle \cdot, \cdot \rangle$

$$\|w\|_2 := \sqrt{\langle w, w \rangle} = \sqrt{\frac{1}{2\pi} \int_{-\pi}^{\pi} |w|^2 \, dt}. \tag{3.2.2}$$

In addition to the concept of a distance on $\mathcal{H}$, also the concept of orthogonality is introduced by the scalar product. Two vectors a, b are said to be orthogonal if $\langle a, b \rangle = 0$.

For a locally integrable 2π-periodic function $w \in \mathcal{H}$, the Fourier transformation is given by the function $\widehat{w} : \mathbb{Z} \to \mathbb{C}$, where

$$\widehat{w}(k) = \frac{1}{2\pi} \int_{-\pi}^{\pi} w(t) e^{-ikt} dt. \tag{3.2.3}$$

With $\widehat{w}(k) = \widehat{w}_k$, the sequence $(\widehat{w}_k)$ stands for the Fourier coefficients, and is called the discrete spectrum of w. The n-th Fourier polynomial, $S_n w$, for w is defined by the trigonometric expansion

$$S_n w(t) := \sum_{k=-n}^{n} \widehat{w}(k) e^{ikt}. \tag{3.2.4}$$

Most of the engineering problems deal with real functions. Hence, a corresponding representation of the Fourier polynomial would simplify the theoretical formulations, which then leads to the derivation of final real equations for a considered problem. Such simplification can be achieved by setting $\widehat{a}_k = \widehat{w}(k) + \widehat{w}(-k)$, $\widehat{b}_k = i(\widehat{w}(k) - \widehat{w}(-k))$ and replacing e^{ikt} with $\cos(kt) + i \sin(kt)$ in (3.2.4). This results in

$$S_n w(t) = \frac{\widehat{a}_0}{2} + \sum_{k=1}^{n} \widehat{a}_k \cos(kt) + \widehat{b}_k \sin(kt), \tag{3.2.5}$$

where $\widehat{a}_k$ and $\widehat{b}_k$ have the following integral representation

$$\widehat{a}_k = \frac{1}{\pi} \int_{-\pi}^{\pi} w(t) \cos(kt) dt, \qquad k = 0, 1, 2, \cdots, \tag{3.2.6}$$

$$\widehat{b}_k = \frac{1}{\pi} \int_{-\pi}^{\pi} w(t) \sin(kt) dt, \qquad k = 1, 2, \cdots. \tag{3.2.7}$$

Also, it follows that, if w is a real-valued function, then $\widehat{a}_k$ and $\widehat{b}_k$ become real numbers.

The sequence of the Fourier polynomials, $S_n w$, results in the Fourier series

$$Sw(t) = \lim_{n \to \infty} S_n w(t) = \frac{\widehat{a}_0}{2} + \sum_{k=1}^{\infty} \widehat{a}_k \cos(kt) + \widehat{b}_k \sin(kt). \tag{3.2.8}$$

The limit exists in case of convergence, which is actually induced by the scalar product (3.2.1).

If the Fourier series of w converges at a point t, the following equation holds

$$Sw(t) = \frac{w(t-) + w(t+)}{2}. \tag{3.2.9}$$

At a point t of continuity, it is $Sw(t) = w(t)$. The equation (3.2.9) follows from the ansatz of Fejér and the fact that the mean of Fourier polynomials correspond to the Fejér polynomials (as illustrated by Königsberger [Kön03]). A detailed convergence analysis is out of the scope of this work. Interested readers are referred to [Kön03] for the point-wise convergence, uniform convergence and quadratic mean convergence of the Fourier series.

3.2.2 Discrete Fourier Transform

For signals known at a finite number N of time samples $t_j = \frac{2\pi j}{N}$ with $j = 1, 2, \cdots, N$, an equivalent of the continuous Fourier transformation (3.2.3) can be represented by the discrete Fourier transformation defined as

$$\widehat{\widehat{w}}(k) = \frac{1}{N} \sum_{j=1}^{N} w(t_j) e^{-ikt_j}. \tag{3.2.10}$$

Concerning the orthogonality relations, (3.2.10) can be inverted and the resulting trigonometric polynomial (similar to (3.2.4)) serves as an interpolant of w at time instants t_j,

$$I_n w(t) := \sum_{k=-n}^{n} \widehat{\widehat{w}}(k) e^{ikt}. \tag{3.2.11}$$

Further, let us define

$$\widehat{\widehat{a}}_k := \widehat{\widehat{w}}(k) + \widehat{\widehat{w}}(-k), \tag{3.2.12}$$

$$\widehat{\widehat{b}}_k := i(\widehat{\widehat{w}}(k) - \widehat{\widehat{w}}(-k)). \tag{3.2.13}$$

Inserting (3.2.10) in (3.2.12) yields the discrete cosine transform

$$\begin{aligned}
\widehat{\widehat{a}}_k &= \frac{1}{N} \sum_{j=1}^{N} w(t_j) e^{-ikt_j} + \frac{1}{N} \sum_{j=1}^{N} w(t_j) e^{ikt_j} = \frac{1}{N} \sum_{j=1}^{N} w(t_j) \left[e^{-ikt_j} + e^{ikt_j} \right] \\
&= \frac{1}{N} \sum_{j=1}^{N} w(t_j) \left[\cos(kt_j) - i \sin(kt_j) + \cos(kt_j) + i \sin(kt_j) \right] \\
&= \frac{2}{N} \sum_{j=1}^{N} w(t_j) \cos(kt_j)
\end{aligned} \tag{3.2.14}$$

Following (3.2.13), the derivation of the discrete sine transform is analogous

$$\widehat{\widehat{b}}_k = \frac{2}{N} \sum_{j=1}^{N} w(t_j) \sin(kt_j). \tag{3.2.15}$$

Finally, the interpolant (3.2.11) can be written in a more convenient way

$$I_n w(t) = \frac{\widehat{\widehat{a}}_0}{2} + \sum_{k=1}^{n} \widehat{\widehat{a}}_k \cos(kt) + \widehat{\widehat{b}}_k \sin(kt). \tag{3.2.16}$$

4 On the Potential of Harmonic Balance in Cardiovascular Fluid Mechanics

Abstract

The application of fluid mechanics concepts in the domain of cardiovascular research has turned out to be very valuable for the analysis of blood flow in the arteries and its interaction with the arterial walls. The typical flow regime is unsteady and periodic in nature as dictated by cardiac dynamics. Most studies featuring computational simulations have approached the problem exploiting the traditional mathematical formulation in the time domain, an approach that can be extremely time-consuming. This work presents the application and exploration of the harmonic balance method as an alternative numerical modeling tool to resolve the dynamic nature of blood flow. The method takes advantage of the pulsatile regime to transform the original problem into a family of equations in frequency space, while the combination of the corresponding solutions yields the periodic solution of the original problem. As a result of this study we conclude that only a few harmonics are required for resolving the fluid flow accurately, for the regimes encountered in the cardiovascular system, and the method is worth of further investigation in this field. Also, the harmonic balance approach has been compared with a traditional method in terms of computational effort and accuracy. Finally, a realistic set-up based on a glass replica of human aorta is employed to illustrate the potential of harmonic balance method in the context of cardiovascular fluid mechanics.

4.1 Introduction

In order to assess clinically relevant hemodynamic parameters, different imaging modalities, particularly those capable of providing insights in the velocity components of the blood flow, have received considerable attention [Hoc04; Ren06; Kat07; Mar12; Kol16]. Notably, phase-contrast magnetic resonance imaging (also known as 4D flow MRI) has gained relevance as it offers several advantages. Velocity measurements can be performed in-vivo and non-invasively. Moreover, 4D flow MRI offers full-field velocity components of the blood flow, that is, full three-dimensional spatial encoding as a time series data [Mar12].

However, 4D flow MRI is not able to accurately predict some flow related quantities, such as wall shear stress, owing to its limitations such as low resolution and signal-to-noise ratio (SNR). Furthermore, it also suffers from partial volume effects [Tha95]. In spite of this, 4D

flow MRI can still provide useful information, when properly integrated with complementary approaches to compensate its shortcomings. Computational fluid dynamics (CFD), relying on partial differential equations, is based on first principles and can provide an accurate picture of the blood flow phenomenology. In this regard, such mathematical formulation requires the definition of boundary conditions (BCs) for the specific arterial district under consideration, as well as for the specific patient under study. However, blood flow simulations based on CFD are known to be quite sensitive to the BCs [Wak09].

In the last two decades, there has been a considerable amount of research addressing the combination of the advantages offered by computational fluid dynamics (CFD) and 4D flow MRI to estimate the blood flow in patient-specific settings [Zha03; Pap03; Mar04; Ray08; Iso10; Gha16; Col18]. Many of such studies apply the measured velocity field as BC for the CFD simulations. Two approaches to define these BCs have been considered. Either the prescription of the flow rates retrieved from the observations or the prescription of point-wise velocity data mapped at the boundaries. Initially these studies considered steady-state scenarios for simplification purposes. However, the flow is heavily influenced by the pulsatile nature of the heart beat, which results in unsteady and periodic flow phenomena. In this sense, more recent studies considered transient CFD simulations supported by the observations (either flow rate or point-wise velocity BCs) obtained from 4D flow MRI. In Zhao *et al.* [Zha03], the quantification of pulsatile flow was studied in a carotid bifurcation phantom, where the experiments were based on a set of 2D slices. The flow waveforms were applied as BCs. Further studies also applied volumetric flow rates as inflow BCs, considering cerebral aneurysm or carotid artery bifurcation [Ray08; Gha16]. A validation study of steady inspiratory flow in models of human airways was reported by Collier *et al.* [Col18]. They use time-resolved 1D velocity profiles obtained from phase-contrast MRI at 2D slices and perform transient CFD simulation based on the obtained flow rates. Moreover, the axial velocity component was applied as BC for transient CFD studies in carotid bifurcation models [Pap03; Mar04], whereas fully point-wise imposition of the velocity field was considered by Isoda *et al.* [Iso10] to study the hemodynamics in intracranial aneurysm. In all of these studies CFD was combined and compared with flow MRI in terms of clinically relevant parameters, such as the evaluation of wall shear stresses (WSS).

When performing pulsatile flow simulations in computational hemodynamics, the traditional approach consists in the time-discretisation of the PDEs using adequate numerical schemes which require the definition of boundary conditions at every time instant. Sparsely measured velocity profiles can be interpolated to generate velocity fields to be applied as dynamic BCs for each time instant. Most of these studies simply apply linear interpolation [Zha03; Wak09; Iso10; Mar04], whereas other studies did not mention how the measured data was interpolated to prescribe the time-dependent velocity boundary conditions [Pap03; Ray08; Gha16; Col18]. In addition, Miyazaki *et al.* [Miy17] performed a validation study in the aortic arch using 4D flow MRI and considered a spline interpolation for transient CFD simulations.

With regards to the temporal discretisation, in this work we propose to employ an alternative and effective approach which, up to the authors' knowledge, is novel in the field of computational hemodynamics. The proposed method is based on the Fourier decomposition of the velocity field and enables the evaluation of its derivative with respect to time in frequency space. Furthermore, it offers the crucial advantage that the new temporal discretisation can be adjusted to be registered with the time instants corresponding to available observations. This eliminates the necessity for completing the missing data for all time steps, as required in conventional methods. Hence, simple linear interpolations (or similar strategies) of the measured fields into the infinitesimal time steps are not needed. In fact, the proposed method can be considered as an alternative interpolation approach, which proves to be accurate and remarkably effective in terms of computational time.

In addition, and for comparison purposes, we describe a method to provide traditional time discretisation schemes with the missing time dependent BCs. Instead of using a simple linear interpolation, this method performs an inverse problem based on penalized regression spline. As a result of this, the method aims to reconstruct the inflow BCs at all time instants present in the time discretization, for which the observations are not available.

The proposed methods were tested and analysed in the context of an arterial geometry corresponding to a 3D physical phantom aorta. First, periodic solutions were numerically manufactured to be used as the ground truth for validation purposes. Second, a real 4D flow MRI acquisition was performed using the phantom aorta. Finally, the proposed methods were tested based on these observations and compared in terms of accuracy and effort.

4.2 Materials

A phantom made of glass is utilised to mimic the human aorta, covering the aortic root, the ascending and descending aorta. Branches were not considered. This geometry has been employed

- to manufacture numerical solutions, as explained in Section 4.4.1;
- as a phantom to perform time-resolved phase-contrast MRI acquisition (4D flow MRI), as explained next.

The manufactured solution is merely used to validate the approach based on a numerically generated ground truth, whereas the 4D flow MRI acquisition is used as an additional verification process, aimed to show the feasibility of the proposed methods using real in-vitro dynamic flow measurements.

4.2.1 Experimental Setup for 4D flow MRI

In chapter 2, section 2.5 an experimental setup has been provided to perform steady-state flow measurements. In the present section, the same environment and tools were used to perform

a time-dependent in-vitro experiment in the glass replica of human aorta. A schematic view of the experimental environment can be observed in Figure 2.11.

The working fluid was created with a mixture of 24 liter H_2O, 46 gr carboxymethyl cellulose (CMC) to increase the viscosity and 10 gr sulfate as a contrast agent to increase the signal magnitude. The CMC medium correspondingly increased the viscosity of the working fluid to an approximate level of blood viscosity in the aorta, which resulted in 4.5 cP at a temperature of 29° C. Finally, the reservoir was filled with the working fluid.

A dynamic data acquisition with a 3D spoiled Gradient-Echo sequence and flow encoding gradients was performed under laminar flow conditions. Linear phase correction was applied to compensate for the background phase induced by eddy-current. Controlling the flow rates, a Reynolds number of at most 1100 was achieved. The flow model in this work does not account for turbulence, which is a matter of current research.

Concerning the acquisition parameters, time of repetition and echo (TR/TE) were 2.7/4.7 ms, velocity encoding (VENC) was 150 $\frac{\text{cm}}{\text{s}}$ and field of view (FOV) was $[160 \times 260 \times 50]$ mm^3. The acquired voxel size was 1.5 mm^3 isotropic, along with a time resolution of 33 ms. The period of one heart cycle was chosen to be 0.825 seconds and 25 data were acquired per cardiac cycle. Finally, the obtained volumetric flow rate resulted in a wave containing two peaks of different magnitudes (see Figure 4.1(a)). The first peak is of higher magnitude (at the same time the peak amplitude of the wave) and represents the systolic phase of the cardiac cycle.

4.2.2 Data Preprocessing and Geometry Generation

Image reconstruction from 4D flow MRI data acquisition yields 3D CINE magnitude images (anatomical data) and three phase difference images (velocity data), corresponding to the components of the 3D velocity field [Mar12]. Following the reconstruction process, obtained raw measurements (anatomical and velocity data) underwent a set of preprocessing tasks, which have been comprehensively described in sections 2.3 and 2.5.3. Hence, in-depth details are skipped here for the sake of brevity.

Three computational meshes with different numbers of cells were generated using the available exact geometry from 3D print of the aortic replica. The cells of the meshes were mainly made up of hexahedras, along with a smaller number of polyhedras, prisms and tetrahedral elements. The total numbers of cells were approximately 215 000, 440 000 and 750 000, whereby these computational meshes will be denoted as $\mathbf{M_2}$, $\mathbf{M_4}$ and $\mathbf{M_7}$ respectively.

It is worthy of note that the velocity data retrieved from the experimental setting is initially not aligned with the exact geometry of the aortic replica. In order to map the measured velocity components onto the computational geometry, a registration process is required. For this purpose, the aortic replica was segmented from the anatomical data (which is already aligned with the velocity data) and registered with the exact geometry. Applied methodologies for registration and segmentation are described in detail in sections 2.3.2 and 2.5.3.

The measured velocity components in the observational domain are denoted as $\boldsymbol{u}_{\mathbf{mri}}$. Owing to the noise nature of phase-contrast flow MRI measurements, a universal outlier detection scheme was applied on $\boldsymbol{u}_{\mathbf{mri}}$ prior to the registration process. The resulting denoised flow field in the observational domain, after the elimination of potential spurious vectors, is denoted by $\boldsymbol{u}^{\circ}_{\mathbf{mri}}$. Relying on the segmentation and registration processes explained in the previous paragraph, the denoised flow field $\boldsymbol{u}^{\circ}_{\mathbf{mri}}$ was linearly mapped from the observational domain to the computational mesh domain, rendering the velocity field $\bar{\boldsymbol{u}}_{\mathbf{mri}}$. Finally, a projection into a divergence-free space is applied to the field $\bar{\boldsymbol{u}}_{\mathbf{mri}}$, resulting in a divergence-free flow field in the computational domain, which is denoted as $\tilde{\boldsymbol{u}}^{\star}$. This projection step was inspired by the Helmholtz-Hodge decomposition (HHD). Applying the projection step is advantageous in two aspects: first, it helps to fill in the gaps generated after the elimination of the detected outliers; second, it recovers back the divergence-free property of the flow field which is otherwise lost on account and nature of the acquisition and preprocessing stages. In what follows, only the flow field $\tilde{\boldsymbol{u}}^{\star}$ is used as the so-called observational data for the application of the methodologies proposed in this work. All the outlined preprocessing steps are described in detail in [Kol18], and can be summarized as follows

$$\boldsymbol{u}_{\mathbf{mri}} \xrightarrow{\text{Outlier Detection}} \boldsymbol{u}^{\circ}_{\mathbf{mri}} \xrightarrow{\text{Registration}} \bar{\boldsymbol{u}}_{\mathbf{mri}} \xrightarrow{\text{Space Projection}} \tilde{\boldsymbol{u}}^{\star}$$

$\boldsymbol{u}_{\mathbf{mri}}$: Reconstructed flow field from 4D flow MRI,

$\boldsymbol{u}^{\circ}_{\mathbf{mri}}$: Denoised flow field in observational domain (usually coarse mesh),

$\bar{\boldsymbol{u}}_{\mathbf{mri}}$: Flow field mapped in the computational domain (fine mesh),

$\tilde{\boldsymbol{u}}^{\star}$: Divergence-free flow field defined in the computational domain.

4.3 Methods

Let $\Omega \subset \mathbb{R}^3$ be an open set with boundary $\partial\Omega = \Gamma_i \cup \Gamma_o \cup \Gamma_w$. See Figure 4.1(b), where Γ_i, Γ_o and Γ_w represent the inlet, outlet and wall boundaries respectively. An incompressible Newtonian fluid is assumed to flow through Ω in the time interval $\mathbb{T} := [0; T]$, as the result of prescribed T-periodic inflow data at Γ_i. The velocity field prescribed at the inlet is characterized by the function $\boldsymbol{g} = \boldsymbol{g}(t, \boldsymbol{x}) = \boldsymbol{g}(t + mT, \boldsymbol{x}) : \mathbb{T} \times \Gamma_i \to \mathbb{R}^3$ with $m \in \mathbb{N}$. The density and dynamic viscosity of the fluid are denoted as ρ and μ respectively.

4.3.1 Mathematical Model

Setting $\boldsymbol{\mathcal{U}} = \left\{ \boldsymbol{v} \in \boldsymbol{H}^1(\Omega) \mid \boldsymbol{v}|_{\Gamma_w} = \mathbf{0} \right\}$, the variational form of the Navier-Stokes equations, in which the boundary datum $\boldsymbol{g}$ over Γ_i is enforced through a Lagrange multiplier, say $\boldsymbol{r}$, can be written as follows: for $t \in \mathbb{T}$, given the initial guess $\boldsymbol{u}(0, \boldsymbol{x}) = \boldsymbol{u}(\boldsymbol{x})^{\{0\}}$, find $(\boldsymbol{u}, p, \boldsymbol{r}) \in$

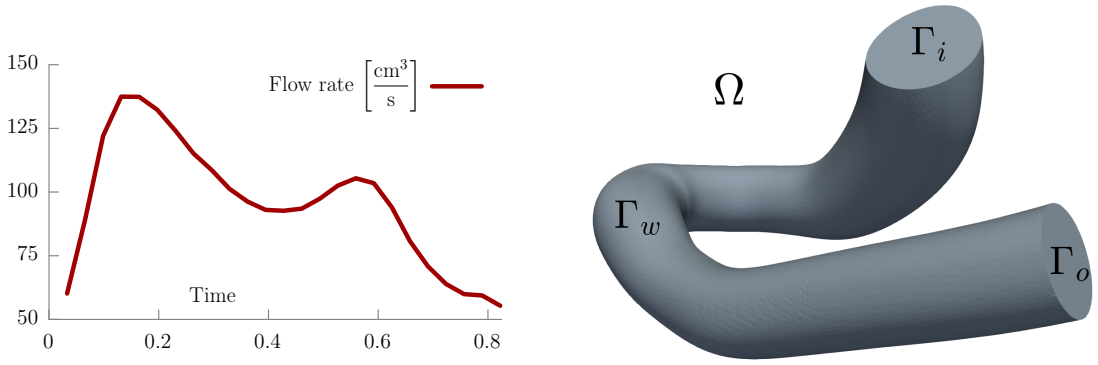

(a) Flow Rate (b) Flow Domain

Figure 4.1: Flow rate waveform obtained from 4D flow MRI acquisition in the observational flow domain Ω, whose boundaries are Γ_i : inlet, Γ_o : outlet and Γ_w : wall.

$\boldsymbol{\mathcal{U}} \times L^2(\Omega) \times \boldsymbol{H}^{-\frac{1}{2}}(\Gamma_i)$, such that

$$\begin{aligned} &\int_\Omega \left[\rho \frac{\partial \boldsymbol{u}}{\partial t} \cdot \hat{\boldsymbol{u}} + \rho(\nabla \boldsymbol{u})\boldsymbol{u} \cdot \hat{\boldsymbol{u}} + 2\mu \nabla^s \boldsymbol{u} \cdot \nabla^s \hat{\boldsymbol{u}} - p \operatorname{div} \hat{\boldsymbol{u}} - \hat{p} \operatorname{div} \boldsymbol{u}\right] d\Omega \\ &= \int_{\Gamma_i} \hat{\boldsymbol{r}} \cdot (\boldsymbol{u} - \boldsymbol{g})\, d\Gamma + \int_{\Gamma_i} (\boldsymbol{r} \cdot \hat{\boldsymbol{u}})\, d\Gamma \quad \forall\, (\hat{\boldsymbol{u}}, \hat{p}, \hat{\boldsymbol{r}}) \in \boldsymbol{\mathcal{U}} \times L^2(\Omega) \times \boldsymbol{H}^{-\frac{1}{2}}(\Gamma_i) \ . \end{aligned} \tag{4.3.1}$$

Denoting $\dfrac{\partial \boldsymbol{u}}{\partial t} = \partial_t \boldsymbol{u}$ and integrating by parts in equation (4.3.1) yields

$$\begin{aligned} &\int_\Omega \left[\rho(\partial_t \boldsymbol{u}) \cdot \hat{\boldsymbol{u}} + \rho(\nabla \boldsymbol{u})\boldsymbol{u} \cdot \hat{\boldsymbol{u}} - \mu \Delta \boldsymbol{u} \cdot \hat{\boldsymbol{u}} + \nabla p \cdot \hat{\boldsymbol{u}}\right] d\Omega - \int_\Omega \hat{p} \operatorname{div} \boldsymbol{u}\, d\Omega \\ &+ \int_{\partial\Omega} \left[-p\boldsymbol{n} + 2\mu(\nabla^s \boldsymbol{u})\boldsymbol{n}\right] \cdot \hat{\boldsymbol{u}}\, d\Gamma \\ &= \int_{\Gamma_i} \hat{\boldsymbol{r}} \cdot (\boldsymbol{u} - \boldsymbol{g})\, d\Gamma + \int_{\Gamma_i} (\boldsymbol{r} \cdot \hat{\boldsymbol{u}})\, d\Gamma \quad \forall\, (\hat{\boldsymbol{u}}, \hat{p}, \hat{\boldsymbol{r}}) \in \boldsymbol{\mathcal{U}} \times L^2(\Omega) \times \boldsymbol{H}^{-\frac{1}{2}}(\Gamma_i) \ . \end{aligned} \tag{4.3.2}$$

Thus, the variational equation (4.3.1) implies the following strong formulation

$$\rho\left[\partial_t \boldsymbol{u} + (\nabla \boldsymbol{u})\boldsymbol{u}\right] - \mu \Delta \boldsymbol{u} + \nabla p = \boldsymbol{0} \qquad \text{in } \mathbb{T} \times \Omega \ , \tag{4.3.3}$$

$$\operatorname{div} \boldsymbol{u} = 0 \qquad \text{in } \mathbb{T} \times \Omega \ , \tag{4.3.4}$$

$$\boldsymbol{u} = \boldsymbol{0} \qquad \text{on } \mathbb{T} \times \Gamma_w \ , \tag{4.3.5}$$

$$\boldsymbol{u} = \boldsymbol{g} \qquad \text{on } \mathbb{T} \times \Gamma_i \ , \tag{4.3.6}$$

$$(-p\boldsymbol{I} + 2\mu \nabla^s \boldsymbol{u})\boldsymbol{n} = \boldsymbol{r} \qquad \text{on } \mathbb{T} \times \Gamma_i \ , \tag{4.3.7}$$

$$(-p\boldsymbol{I} + 2\mu \nabla^s \boldsymbol{u})\boldsymbol{n} = \boldsymbol{0} \qquad \text{on } \mathbb{T} \times \Gamma_o \ , \tag{4.3.8}$$

$$\boldsymbol{u}(0, \boldsymbol{x}) = \boldsymbol{u}(\boldsymbol{x})^{\{0\}} \qquad \text{in } \Omega \ , \tag{4.3.9}$$

where the strain rate tensor is defined as $\nabla^s(\cdot) = [\nabla(\cdot) + (\nabla(\cdot))^T]/2$.

4.3.2 Approaches to Time Discretization

When performing numerical simulations in the context of computational hemodynamics, a typical approach is trying to take into account as many reliable measured values as possible. In the present case, it was postulated that the velocity field is known on boundary Γ_i (see equation (4.3.6) where the datum is $\boldsymbol{g}$). In the case of transient problems, as in the present study, such boundary condition is time-dependent. In real world problems, measured data is provided only at a sparse set of time instants. Hence, an effective and reliable approach is necessary for an efficient completion of the boundary data at missing time instants, based on the measured data.

This work proposes two different approaches to tackle time-dependent fluid flow simulations and compares the methods in terms of accuracy and efficiency. The first method is the classical approach which relies on the traditional time discretization of the system of partial differential equations seen in the previous section. In this case, the boundary data is constructed from the sparse set of instant point measurements using cubic splines, rendering a continuous function $\boldsymbol{s}$. This approach will be termed as "the traditional method using penalized regression spline".

The second strategy, and the main contribution of the present work, takes a different path which proves to be computationally more efficient. It relies on a temporal discretization of the momentum equation (4.3.3) based on a trigonometric polynomial in time. This method is also known as the harmonic balance (HB) approach, which was previously applied in different fields with preliminary results mostly based on 2D flow simulations or idealized cylindrical geometries [Sto72; Hal02; Bac05; Hal13; Gar13; Kar14; Cvi16]. To the best of authors' knowledge, the HB method is investigated in this work for the first time in the field of computational hemodynamics.

In both methods, sparsely distributed dynamic acquisitions obtained from 4-D flow MRI are employed as observational data. The main contribution of this work is the assessment of the HB method to conduct hemodynamic simulations in the context of realistic geometries and realistic boundary data. To this end, the traditional approach (using penalized regression spline method) is employed to serve as reference method for comparison purposes, in terms of accuracy and computational efficiency.

4.3.3 Traditional Method Using Penalized Regression Spline

Let $\tilde{\boldsymbol{u}}^\star(t^k)$ be some set of measurements acquired at time instants t^k, for $k = 1, 2, \cdots, N$. The penalized regression spline (PRS) method delivers a smooth function, denoted by $\boldsymbol{s}$, as an approximation of the observations $\tilde{\boldsymbol{u}}^\star(t^k)$. The regression model functions are of class C^2 and correspond to cubic splines with uniformly distributed nodes. The approximation does not aim to enforce an exact agreement with the observed data, as this would be inappropriate due to the noisy nature of the MRI velocities. Instead, the PRS method is cast as a mathematical optimization problem, which aims to minimize the sum of squared fitting error relaxed by a

Tikhonov regularization term weighted by λ. The minimizer function defines a time dependent signal $\boldsymbol{s}$ that plays the role of the datum, $\boldsymbol{g}$, required at the inlet boundary in equation (4.3.6). For each spatial position in Γ_i, the interpolation in time reads

$$\boldsymbol{s}(t) = \underset{\boldsymbol{a} \text{ in } \Omega}{\arg\min} \left(\sum_k |\tilde{\boldsymbol{u}}^\star(t^k) - \boldsymbol{a}(t^k)|^2 + \lambda \int |\boldsymbol{a}''(\tau)|^2 d\tau \right) \qquad \text{for } t \in \mathbb{T}. \tag{4.3.10}$$

This strategy defines a time continuous function and allows the definition of the BC ($\boldsymbol{g} = \boldsymbol{s}$ on Γ_i) at any time instant in the time-discrete problem when utilizing the traditional approach.

4.3.4 Harmonic Balance

In what follows, we will consider a time discretisation of the momentum equation (4.3.3), which can be expressed in the following compact form

$$\partial_t \boldsymbol{u} = \boldsymbol{f}(t, \boldsymbol{u}), \tag{4.3.11}$$

where $\boldsymbol{f} = -\left[(\nabla \boldsymbol{u})\boldsymbol{u} - \nu \Delta \boldsymbol{u} + \dfrac{\nabla p}{\rho}\right]$ (with $\nu := \dfrac{\mu}{\rho}$ being the kinematic viscosity), which encompasses the convective, diffusive, pressure forces, and possibly other force terms.

Equation (4.3.11) has the form of an evolution equation (see (3.1.1)). Hereinafter, the theoretical material provided in chapter 3 will be systematically employed. Both sections 3.1 and 3.2 contain an abstract description aimed to present the theoretical framework in a general form. Hence, for example, a 2π-periodic function in the time domain $[-\pi; \pi]$ was considered in chapter 3 along with its approximation based on complex valued expansion coefficients. In the context of hemodynamic simulations, however, the dependent state variable of interest, such as the velocity $\boldsymbol{u}$, is actually a T-periodic real vector-valued function in time. Therefore, in what follows, the time interval $\mathbb{T} := [0; T]$ is considered instead and, in addition, real-valued expansion coefficients are used for the approximation of $\boldsymbol{u}$.

Let $\varphi_k : \mathbb{R} \to \mathbb{R}$ and $\boldsymbol{c}_k : \Omega \to \mathbb{R}^3$ be sequences of real valued basis functions and expansion coefficients respectively. Further, let $\tilde{\boldsymbol{u}}(t, \boldsymbol{x})$ be an approximation of $\boldsymbol{u}$ (see (3.1.2)) as follows

$$\tilde{\boldsymbol{u}}(t, \boldsymbol{x}) = \sum_{k=1}^{2n+1} \boldsymbol{c}_k(\boldsymbol{x}) \varphi_k(t). \tag{4.3.12}$$

According to the method of weighted residuals (MWR) as explicitly described in section 3.1, we are interested in weighting the momentum residual $\mathscr{R}(\tilde{\boldsymbol{u}}) = \partial_t \tilde{\boldsymbol{u}} - \boldsymbol{f}(t, \tilde{\boldsymbol{u}})$ with several weight functions $\varpi : \mathbb{R} \to \mathbb{R}$ and requiring their integral to be identically zero,

$$\int_{\mathbb{T}} \mathscr{R}(\tilde{\boldsymbol{u}}) \varpi(t)\, dt = \boldsymbol{0}. \tag{4.3.13}$$

The selection of the basis functions φ_k from the following set of trigonometric functions

leads to Fourier spectral methods (this and other possible choices are described in section 3.1)

$$\mathcal{T} := \{\, 1, \cos(\omega t), \sin(\omega t), \cos(2\omega t), \sin(2\omega t), \, \cdots \, , \cos(n\omega t), \sin(n\omega t) \,\}, \tag{4.3.14}$$

where $\mathcal{T}$ represents a complete L^2-orthogonal system on $\mathbb{T}$ and $\omega = \frac{2\pi}{T}$ is the angular frequency. This choice corresponds to the n-th Fourier polynomial

$$\tilde{\boldsymbol{u}}(t, \boldsymbol{x}) = \frac{\widehat{\boldsymbol{u}}_{c_0}(\boldsymbol{x})}{2} + \sum_{k=1}^{n} \Big[\widehat{\boldsymbol{u}}_{c_k}(\boldsymbol{x}) \cos(k\omega t) + \widehat{\boldsymbol{u}}_{s_k}(\boldsymbol{x}) \sin(k\omega t) \Big], \tag{4.3.15}$$

where $\widehat{\boldsymbol{u}}_{c_k}$ for $k = 0, 1, ..., n$ and $\widehat{\boldsymbol{u}}_{s_k}$ for $k = 1, ..., n$ form the discrete spectrum of $\boldsymbol{u}$ (the readers are referred to section 3.2 for a mathematical description of the spectrum and the derivation of (4.3.15)).

The Fourier spectral method is further distinguished by the choice of the weight function (or arbitrary variation) ϖ in the weighted equation (4.3.13). In general, this choice distinguishes the approaches which are usually named as the Galerkin, tau or collocation methods (section 3.1 describes these methods and their differences). In this work, the collocation Fourier spectral method is employed, which considers the weight function to be the Dirac delta function $\varpi = \delta(t - t_j)$ shifted at the so-called collocation points

$$t_j := \frac{j\, T}{2n+1}, \quad j = 1, 2, \cdots, 2n+1. \tag{4.3.16}$$

The time instants t_j are equidistantly placed on $\mathbb{T}$ and their number is $2n+1$, which is in correspondence with the number of terms in the Fourier polynomial (4.3.15). Following the collocation approach, (4.3.13) becomes

$$\int_{\mathbb{T}} \Big[\partial_t \tilde{\boldsymbol{u}} - \boldsymbol{f}(t, \tilde{\boldsymbol{u}}) \Big] \delta(t - t_j)\, dt = \boldsymbol{0}. \tag{4.3.17}$$

This forces the momentum residual $\mathscr{R}(\tilde{\boldsymbol{u}})$ to be exactly zero at each t_j, yielding $2n+1$ equations (recall that $-\boldsymbol{f}(t, \boldsymbol{u}) \approx -\boldsymbol{f}(t, \tilde{\boldsymbol{u}})$)

$$\Big\{ \partial_t \tilde{\boldsymbol{u}} - \boldsymbol{f}(t, \tilde{\boldsymbol{u}}) = \boldsymbol{0} \Big\} \Big|_{t_j}, \quad j = 1, 2, \cdots, 2n+1. \tag{4.3.18}$$

Finally, replacing (4.3.15) into (4.3.18) and applying the derivative, the following $2n+1$ equations are obtained in the frequency domain

$$\sum_{k=1}^{n} \Big[-\widehat{\boldsymbol{u}}_{c_k} k\omega \sin(k\omega t_j) + \widehat{\boldsymbol{u}}_{s_k} k\omega \cos(k\omega t_j) \Big] = \boldsymbol{f}(t_j, \tilde{\boldsymbol{u}}(t_j, \boldsymbol{x})), \quad j = 1, 2, \cdots, 2n+1 \tag{4.3.19}$$

Solving the equations in (4.3.19) would yield the Fourier coefficients (or the discrete spectrum) of $\tilde{\boldsymbol{u}}$. The Fourier coefficients have to be computed numerically. However, there are

serious challenges and obstacles in solving for the Fourier coefficients, essentially due to the existence of non-linearities in the system [Can88]. Moreover, the evaluation of harmonic fluxes requires $\mathcal{O}(n^3)$ operations, which makes the problem (of solving for Fourier coefficients) computationally very expensive and practically unfeasible [Hal02; Hal13]. In addition, since we are interested in solving for the approximation $\tilde{\boldsymbol{u}}$ of the state variable $\boldsymbol{u}$, the information gained in the frequency domain must be effectively reconstructed in the time domain. The most effective way to overcome all these difficulties lies in the application of the discrete Fourier transformation (DFT) (see section 3.2.2). Using the DFT, a signal known at a finite number of time samples t_j is transformed into its discrete spectrum, which is in a linear relation to the signal. Therefore, this process can be inverted (through the iDFT), recovering back the information in the time domain. For the approximation $\tilde{\boldsymbol{u}}$, the inversion results in an interpolant of the signal (see (3.2.16) for detailed derivation)

$$I_n\tilde{\boldsymbol{u}}(t) = \frac{\widehat{\widehat{\boldsymbol{u}}}_{c_0}}{2} + \sum_{k=1}^{n} \widehat{\widehat{\boldsymbol{u}}}_{c_k}\cos(k\omega t) + \widehat{\widehat{\boldsymbol{u}}}_{s_k}\sin(k\omega t), \tag{4.3.20}$$

where $\widehat{\widehat{\boldsymbol{u}}}_{c_k}$ and $\widehat{\widehat{\boldsymbol{u}}}_{s_k}$ are the discrete spectrum of $\tilde{\boldsymbol{u}}$ related to the DFT.

For $i = 1, 2, \cdots, 2n+1$, let $\tilde{\boldsymbol{u}}^{\,i} := \tilde{\boldsymbol{u}}(t_i, \boldsymbol{x})$ be the approximated velocity field at time instant t_i. The DFT of $\tilde{\boldsymbol{u}}^i$ for the discrete spectrum $\widehat{\widehat{\boldsymbol{u}}}_{c_k}$ and $\widehat{\widehat{\boldsymbol{u}}}_{s_k}$ are defined by the corresponding discrete cosine and sine transforms as follows:

$$\widehat{\boldsymbol{u}}_{c_k} \approx \widehat{\widehat{\boldsymbol{u}}}_{c_k} = \frac{2}{2n+1}\sum_{i=1}^{2n+1} \tilde{\boldsymbol{u}}^{\,i}\cos(k\omega t_i), \tag{4.3.21}$$

$$\widehat{\boldsymbol{u}}_{s_k} \approx \widehat{\widehat{\boldsymbol{u}}}_{s_k} = \frac{2}{2n+1}\sum_{i=1}^{2n+1} \tilde{\boldsymbol{u}}^{\,i}\sin(k\omega t_i). \tag{4.3.22}$$

Derivations of the discrete cosine and sine transforms are provided in section 3.2.2 followed by the equations (3.2.14) and (3.2.15). Inserting the discrete spectrum (4.3.21) and (4.3.22) related to the DFT into the equations in (4.3.19) and using the trigonometric identities, $\sin(\alpha \pm \beta) = \sin(\alpha)\cos(\beta) \pm \cos(\alpha)\sin(\beta)$, results in the following approximation,

$$\begin{aligned}
&\sum_{k=1}^{n}\Big[\frac{2k\omega}{2n+1}\sum_{i=1}^{2n+1}\tilde{\boldsymbol{u}}^{\,i}\Big(\sin(k\omega t_i)\cos(k\omega t_j) - \cos(k\omega t_i)\sin(k\omega t_j)\Big)\Big] = \boldsymbol{f}(t_j, \tilde{\boldsymbol{u}}(t_j, \boldsymbol{x})) \\
\Rightarrow\ &\frac{2\omega}{2n+1}\sum_{i=1}^{2n+1}\sum_{k=1}^{n} k\tilde{\boldsymbol{u}}^{\,i}\sin(k\omega(t_i - t_j)) = \boldsymbol{f}(t_j, \tilde{\boldsymbol{u}}(t_j, \boldsymbol{x})), \quad j = 1, 2, \cdots, 2n+1
\end{aligned} \tag{4.3.23}$$

Moreover, setting $N = 2n+1$ and defining the constants

$$c_{ij} = \frac{2\omega}{N}\sum_{k=1}^{n} k\sin(k\omega(t_i - t_j)), \quad i, j = 1, 2, \cdots, N\,, \tag{4.3.24}$$

one finally observes in (4.3.23) the harmonically balanced momentum equations

$$\sum_{i=1}^{N} \tilde{\boldsymbol{u}}^{\,i} c_{ij} + (\nabla \tilde{\boldsymbol{u}}^{\,j})\tilde{\boldsymbol{u}}^{\,j} - \nu \Delta \tilde{\boldsymbol{u}}^{\,j} + \frac{\nabla p^j}{\rho} = \boldsymbol{0}\,, \qquad j = 1, 2, \cdots, N, \tag{4.3.25}$$

where $(\cdot)^j$ represent the fields $(\cdot)$ at time instants t_j.

Regarding the momentum equation (4.3.3), the frequency domain equations are now expressed in terms of the time domain state variables at each equidistantly placed time instant t_j. Furthermore, note that the time derivative term, transformed through the DFT, is responsible for coupling the velocity fields $\tilde{\boldsymbol{u}}^{\,i}$, $i = 1, 2, \cdots, N$, from all time instants. In this manner, the original problem has been cast into the form of a set of coupled fluid flow problems, where the coupling among equations is realized through a linear zero order term, which is defined by the function $\mathscr{Z} : \boldsymbol{\mathcal{U}} \times \big(\mathbb{N} \cap [1; N]\big) \to \boldsymbol{\mathcal{U}}$ as follows:

$$\mathscr{Z}(\boldsymbol{v}, j) = \sum_{i=1}^{N} \boldsymbol{v}^i c_{ij}. \tag{4.3.26}$$

Furthermore, each one of the transformed equations for $j = 1, 2, \cdots, N$ seen in (4.3.25) is supplied with the corresponding BC, represented by $\boldsymbol{g}^j$, which is the observation of the velocity field at the corresponding time t_j. Finally, the set of coupled equations in (4.3.25) yields the periodic solution of the original problem.

Finally, following the HB approach, the Euler-Lagrangian formulation of the temporally discretised incompressible Navier-Stokes equations reads: for $j = 1, 2, \cdots, N$ and $\boldsymbol{g}^j \in \boldsymbol{H}^{\frac{1}{2}}_{00}(\Gamma_i)$ (the space of traces over Γ_i of $\boldsymbol{H}^1(\Omega)$ functions that are zero over the boundary γ_i of surface Γ_i), determine $(\tilde{\boldsymbol{u}}^{\,j}, p^j, \boldsymbol{r}^j) \in \boldsymbol{\mathcal{U}} \times L^2(\Omega) \times \boldsymbol{H}^{-\frac{1}{2}}(\Gamma_i)$ such that

$$\mathscr{Z}(\tilde{\boldsymbol{u}}, j) + (\nabla \tilde{\boldsymbol{u}}^{\,j})\tilde{\boldsymbol{u}}^{\,j} - \nu \Delta \tilde{\boldsymbol{u}}^{\,j} + \frac{\nabla p^j}{\rho} = \boldsymbol{0} \quad \text{in } \Omega\ , \tag{4.3.27}$$

$$\operatorname{div} \boldsymbol{u}^j = 0 \quad \text{in } \Omega\ , \tag{4.3.28}$$

$$\boldsymbol{u}^j = \boldsymbol{0} \quad \text{on } \Gamma_w\ , \tag{4.3.29}$$

$$\boldsymbol{u}^j = \boldsymbol{g}^j \quad \text{on } \Gamma_i\ , \tag{4.3.30}$$

$$(-p^j \boldsymbol{I} + 2\mu \nabla^s \boldsymbol{u}^j)\boldsymbol{n} = \boldsymbol{r}^j \quad \text{on } \Gamma_i\ , \tag{4.3.31}$$

$$(-p^j \boldsymbol{I} + 2\mu \nabla^s \boldsymbol{u}^j)\boldsymbol{n} = \boldsymbol{0} \quad \text{on } \Gamma_o\ , \tag{4.3.32}$$

$$j = 1, 2, \cdots, N\ .$$

4.3.5 Numerical Methods

The finite volume method was adopted to approximate in space the partial differential equations (4.3.3)–(4.3.9) and (4.3.25). As seen in Section 4.3.4, the time discretisation of the momentum equation (4.3.3) in the HB approach leads to the set of harmonically balanced

momentum equations (4.3.25). For the PRS method (see Section 4.3.3), in contrast, the momentum equation was discretised in time using backward differentiation, an implicit scheme of second order accuracy [Jas96, sec. 3.3.2]. The time steps were chosen such that the Courant number was below 0.3.

Both methods, HB and PRS, rely on external solvers known as SIMPLE and PISO algorithms [Pat72; Iss86]. According to this, first the pressure equation is derived from the continuity equation (4.3.4) (in case of HB approach, several pressure equations are derived from the continuity equations corresponding to the set of harmonically balanced momentum equations (4.3.25) respectively) and thereafter the equations for momentum and pressure are solved sequentially. This is achieved by first solving the momentum equations (after proper linearisation and discretisation) relying on the pressure field from previous iteration (or on an initial guess for pressure at the beginning of the solution process). In the next step, the pressure field is corrected relying on the pressure equation derived from continuity. Following this, the corrected pressure field is then used to update the velocity field.

For the set of harmonically balanced momentum equations (4.3.25), the SIMPLE algorithm (as described by Patankar *et al.* [Pat72]) was employed to deal with the pressure-velocity coupling (mentioned in previous paragraph) of each equation, separately. The coupling among all the equations established by the zero order term (4.3.26) is achieved by using a block-Gauss-Seidel iterative algorithm (see Section 4.3.6). In contrast, the PISO algorithm (as described by Issa [Iss86]) was adopted for the treatment of PRS method (and also for the generation of manufactured solutions).

For both methods, HB and PRS, the discretised pressure correction equations were solved with a generalised geometric-algebraic multi-grid (GAMG) solver using Gauss-Seidel smoothing. In addition, the discretised momentum equations were solved with a preconditioned bi-conjugate gradient (PBiCG) method using a simplified diagonal-based incomplete LU preconditioner (DILU). The proposed methods were all implemented using the open source CFD library, OpenFOAM [Wel98].

4.3.6 Block-Gauss-Seidel Algorithm for Harmonic Balance Equations

The harmonically balanced equations for n harmonics consist in $N = 2n + 1$ fully coupled velocity-pressure equations whose numerical solution is accounted for through an iterative algorithm. For each of these N velocity-pressure equations, the coupling is achieved by the SIMPLE algorithm employed in connection with the momentum and the pressure equations (as briefly described in the previous section). This is commonly known as the pressure-velocity coupling. The coupling among the N equations follows from the harmonic balance treatment by which the temporal derivation (appearing only in the momentum equation) is replaced by the zero order term $\mathscr{Z}$ appearing in (4.3.26). This will be named as the HB coupling in this work. Under these considerations, the equation (4.3.25) is solved for each time instant t_j,

whereas the temporal influence from neighbouring time instants is accounted for by $\mathscr{Z}$.

The HB coupling among the N equations is numerically solved through the Gauss–Seidel iterative method. That is, the pressure-velocity systems of equations are successively solved each in its own SIMPLE loop, with always the latest available solution used for evaluating the zero order term. Therefore, N pressure-velocity systems of equations are being solved within N iterating SIMPLE loops. The calculation is considered converged when each of the N equation sets are converged.

Spatial Discretisation of Harmonic Balance Equations

The finite volume method was adopted to approximate in space the time-discrete harmonically balanced partial differential equations (4.3.27)–(4.3.32). The discretisation is presented following the notation introduced by Rusche [Rus02], by which the angle bracket operator $[\cdot]$ denotes the implicit treatment of the encapsulated term. Other terms are treated explicitly. The problem of solving the discretised form of the momentum equation (4.3.27) at t_j reads

$\mathscr{P}_{\boldsymbol{u}^j}(\boldsymbol{u}, \boldsymbol{g}^j, p)$: Given $\boldsymbol{u}, \boldsymbol{g}^j$ and p, determine $\boldsymbol{u}^j$ such that

$$\left[(\nabla \boldsymbol{u}^j)\boldsymbol{u}^j\right] - \left[\nu \Delta \boldsymbol{u}^j\right] = -\frac{\nabla p}{\rho} - \mathscr{Z}(\boldsymbol{u}, j) \quad \text{in } \Omega \tag{4.3.33}$$

$$\boldsymbol{u}^j = \boldsymbol{0} \quad \text{on } \Gamma_w \tag{4.3.34}$$

$$\boldsymbol{u}^j = \boldsymbol{g}^j \quad \text{on } \Gamma_i \tag{4.3.35}$$

$$(\nabla \boldsymbol{u}^j)\boldsymbol{n} = \boldsymbol{0} \quad \text{on } \Gamma_o \tag{4.3.36}$$

It can be seen that the left hand side is calculated implicitly, while the zero order coupling term is obtained explicitly.

Pressure is calculated based on discretised equation obtained by modifying the continuity equations (4.3.28) for all time instants, following the procedure as presented by [Jas96]. In what follows, $(a_p)^j$ denotes the diagonal coefficient of the discretised momentum equation at time instant t_j, whereas $\mathbf{H}(\boldsymbol{u}^j)$ represents the flux operator related to $\boldsymbol{u}^j$. The problem of solving the discretised form of the obtained pressure equation at time instant t_j reads

$\mathscr{P}_{p^j}(\boldsymbol{u}^j)$: Given $\boldsymbol{u}^j$, determine p^j such that

$$\left[\nabla \cdot \left(\frac{1}{(a_p)^j} \nabla p^j\right)\right] = \nabla \cdot \left(\frac{\mathbf{H}(\boldsymbol{u}^j)}{(a_p)^j}\right) \quad \text{in } \Omega \tag{4.3.37}$$

$$\nabla p^j \cdot \boldsymbol{n} = 0 \quad \text{on } \Gamma_w \tag{4.3.38}$$

$$\nabla p^j \cdot \boldsymbol{n} = 0 \quad \text{on } \Gamma_i \tag{4.3.39}$$

$$p^j = 0 \quad \text{on } \Gamma_o \tag{4.3.40}$$

The equation (4.3.37) follows from the continuity equation for each corresponding time instant.

Coupled SIMPLE and HB Iterations

In what follows, the fields $(\cdot)^{\{k\}}$ will represent the fields $(\cdot)$ at k-th iteration of SIMPLE. Conventionally, the solution procedure starts with the initial guesses $p^{\{0\}}$ and $\boldsymbol{u}^{\{0\}}$ for the pressure and the velocity fields respectively. At iteration $k > 0$, the momentum equation is solved for $\boldsymbol{u}^{\{k\}}$ using the fields $p^{\{k-1\}}$ and $\boldsymbol{u}^{\{k-1\}}$ from the previous iteration. With the newly acquired field $\boldsymbol{u}^{\{k\}}$, the pressure equation is then solved for $p^{\{k\}}$. Furthermore, the velocity field $\boldsymbol{u}^{\{k\}}$ is corrected afterwards based on the new pressure field $p^{\{k\}}$. At this point, the convergence is checked and the procedure is repeated until the criterion is fulfilled.

The set of harmonically balanced momentum equations, see (4.3.25), establishes that the velocity fields $\tilde{\boldsymbol{u}}^{\,i}$, $i = 1, \cdots, N$, are coupled through the zero order term $\mathscr{Z}$ (summation over velocity fields at different time instants multiplied by corresponding Fourier coefficients). This system of equations can be decoupled through any iterative process. In this work, the Gauss-Seidel method was employed to this aim.

Algorithm 2 Harmonic balance iterative procedure

Given: $j = 1, 2, \cdots, N$ ▷ Indices of equidistantly placed time instants t_j
Input : $N = 2n + 1$ ▷ Provide number of harmonics n
$(\boldsymbol{u}^j)^{\{0\}}, (p^j)^{\{0\}}$ ▷ Provide initial guesses $(\cdot)^{\{0\}}$
Output : $(\boldsymbol{u}^j)^{\{k\}}, (p^j)^{\{k\}}$ ▷ Flow fields at last iteration k

procedure HarmonicBalanceLoop($\boldsymbol{u}^{\{0\}}, p^{\{0\}}, N$)
  $m \leftarrow$ total number of iterations
  $\boldsymbol{v} \leftarrow \boldsymbol{u}^{\{0\}}$ in Ω
  $\boldsymbol{g} \leftarrow \boldsymbol{u}^{\{0\}}$ on Γ_i
  for $k \leftarrow 1, m$ **do** ▷ HB iterations
    for $j \leftarrow 1, N$ **do** ▷ Solve at each time instant
      $(\boldsymbol{u}^j)^{\{k\}} \leftarrow \mathscr{P}_{\boldsymbol{u}^j}(\boldsymbol{v}, \boldsymbol{g}^j, (p^j)^{\{k-1\}})$ ▷ Solve equations (4.3.33)–(4.3.36)
      $(p^j)^{\{k\}} \leftarrow \mathscr{P}_{p^j}((\boldsymbol{u}^j)^{\{k\}})$ ▷ Solve equations (4.3.37)–(4.3.40)
      Correct $(\boldsymbol{u}^j)^{\{k\}}$ based on $(p^j)^{\{k\}}$
      $\boldsymbol{v}^j \leftarrow (\boldsymbol{u}^j)^{\{k\}}$ ▷ Update zero order term
    end for
    if each L^1-norm (of equation residuals) $< \xi$ **then** ▷ Convergence criterion
      return $(\boldsymbol{u}^j)^{\{k\}}, (p^j)^{\{k\}}$
    end if
  end for
end procedure

Specifically, only one single iteration of the SIMPLE algorithm is performed for each time instant t_j. Each time, when a single iteration of SIMPLE is accomplished for the time instant t_j (and during this process, the equations at all t_i are idle), the new velocity field obtained at time instant t_j is immediately updated in the zero order term of the equations defined at all other time instants t_i. Thus, within the HB iterations, a single iteration of the SIMPLE loop (as presented in the previous section) is performed for time instant t_j. As all time instants are iterated sequentially, all field variables $(\cdot)^j$ go through the same number of SIMPLE iterations. Therefore, one HB iteration implies solving N times the SIMPLE iterations, one for each of the N harmonic equations. Consequently, one can distinguish between a single SIMPLE iteration (once per time instant t_j) and single HB iteration which consists of $2n+1$ single SIMPLE iterations. This process continues until a convergence criterion is met based on the L^1 norm of solution residual, which is evaluated at the per-equation level. Therefore only when the L^1 norm of all $2n+1$ equations is below a small value ξ (convergence criterion), the simulation is considered to be converged. Algorithm 2 describes the harmonic balance method in terms of a pseudo-code.

4.4 Numerical Experiments

Several numerical experiments were performed to compare the HB method with the traditional approach in terms of accuracy and effort. In addition to 4D flow MRI data obtained from phase-contrast flow acquisition (see Section 4.2.1), numerically manufactured solutions were used as the ground truth for validation purposes. Numerical solutions obtained from the traditional method using PRS and the HB approach were first compared with the ground truth in terms of accuracy. Secondly, a convergence study with respect to mesh size was performed. Furthermore, both methods were compared with each other in terms of computational effort. Finally, both methods were provided with observational boundary data obtained from 4D flow MRI acquisition.

The quantitative comparison between any pair of computed flow fields, say $\boldsymbol{u}_c$ and a reference flow field $\boldsymbol{u}_r$, is performed using the following normalised root-mean square error integrated over time

$$\mathrm{nRMSE}(\boldsymbol{u}_c, \boldsymbol{u}_r) = \left(\frac{100}{\underset{\mathbb{T},\Omega}{\mathrm{avr}}|\boldsymbol{u}_r|} \right) \sqrt{\frac{1}{V_\Omega \cdot T} \int_{\mathbb{T}} \int_{\Omega} |\boldsymbol{u}_c - \boldsymbol{u}_r|^2 \, d\Omega \, dt}. \tag{4.4.1}$$

4.4.1 Comparison using Manufactured Solutions

To generate the ground truth data, a dynamic fluid flow with periodic velocity boundary data at the inlet was considered in the geometry of the aortic replica. The reference solutions were numerically manufactured on two different meshes, $\mathbf{M_2}$ and $\mathbf{M_7}$ (the available meshes are described in Section 4.2.2). The solution manufactured on the mesh $\mathbf{M_2}$ was only used

to validate the methods HB and PRS, which were run on exactly the same mesh $\mathbf{M_2}$. An additional reference solution was generated on the finer mesh $\mathbf{M_7}$ and was mapped onto two different coarser meshes, $\mathbf{M_2}$ and $\mathbf{M_4}$.

The reference solutions were created using the same PISO-based solver, which was employed for the PRS method and is described in Section 4.3.5. For a manufactured solution which serves for validation purposes, it is usually convenient to consider a parabolic velocity profile at the inlet. However, the geometry of the aortic replica used in the experiments has no perfect cylindrical shape and as such it is not feasible to define a parabolic function at the inlet analytically. Instead, we have performed a single steady-state flow MRI acquisition using a similar setup as explained in Section 4.2.1 and utilised the obtained flow profile at the inlet as boundary data. In order to reduce the measurement noise, we first smoothed the flow field using low-pass filtering and then applied the resulting flow field as BC at the inlet. To achieve a transient flow simulation, the acquired steady flow profile was dynamically adjusted over time. This was achieved by multiplying each velocity component at the inlet with an appropriately chosen analytical periodic function $h(t)$ of period 0.8 s and base frequency 1.25. The function contains two peaks of different magnitude in one cycle, which was similar to the flow rates obtained from the dynamic experiments. The explicit form of $h(t)$ is as follows

$$h(t) = 0.5\big[0.315 + 0.25\big(\sin(2\pi 1.25t + 1.882\pi) + \sin(2\pi 2.5t + 1.344\pi)\big)\big]. \tag{4.4.2}$$

The simulations for the manufactured solutions were run for twenty periods, at which the time-integrated normalised root-mean square error between the last two periods was below 10^{-11}. Thus, a periodic state of equilibrium was reached.

Validation with a Single Mesh Geometry

As a first step, only a single mesh, $\mathbf{M_2}$, was employed to generate both the numerical reference solution, as well as the solutions based on the methods HB and PRS. This ensures that in the best case scenario the reference solution can be exactly recovered, and allows us to investigate the accuracy of the proposed methods, HB and PRS. The flow field obtained from the manufactured solution will be denoted by $\boldsymbol{u}_{\mathbf{ext}}$ (considered to be the reference, or "exact", solution). The simulations were all run with 48 processors using the compute nodes from Euler high performance computing cluster (located in Lugano) and evaluated in terms of accuracy and computational effort. The accuracy is assessed through the nRMSE, whereas the computational effort is reported in terms of the wall clock time (WCT) in seconds.

The reference flow solution was first sampled at certain time instants, which were then used as the observational boundary data for the solvers HB and PRS. We want to emphasize that the manufactured solution and the solution from PRS method were obtained from one and exactly the same solver. The only difference was the fact, that the velocity BCs prescribed at the inlet for the reference solution were defined from the analytical function (4.4.2), whereas

$\boldsymbol{u}_c$	$\boldsymbol{u}^2_{\mathbf{hb}}$	$\boldsymbol{u}^5_{\mathbf{hb}}$	$\boldsymbol{u}^8_{\mathbf{hb}}$	$\boldsymbol{u}^{10}_{\mathbf{hb}}$	$\boldsymbol{u}^{12}_{\mathbf{hb}}$	$\boldsymbol{u}_{\mathbf{prs}}$
nRMSE($\boldsymbol{u}_c$, $\boldsymbol{u}_{\mathbf{ext}}$)	13.22%	2.18%	0.75%	0.43%	0.29%	0.03%
WCT in sec.	217 s	458 s	788 s	960 s	1 190 s	13 737 s

Table 4.1: Root mean square errors (nRMSE($\boldsymbol{u}^n_{\mathbf{hb}}, \boldsymbol{u}_{\mathbf{ext}}$) and nRMSE($\boldsymbol{u}_{\mathbf{prs}}, \boldsymbol{u}_{\mathbf{ext}}$)) for the HB approach with different number of harmonics 2 to 12 and for PRS method, evaluated against exact solution $\boldsymbol{u}_{\mathbf{ext}}$. In addition, the corresponding wall clock times (WCT) in seconds. Simulations were performed on mesh $\mathbf{M_2}$ using 48 processors.

for the PRS method the BCs were defined by the interpolation function (4.3.10) based on data sampled from the reference solution at the set of time instants.

First of all, the HB method was considered, and the computational effort was evaluated in terms of the number of harmonics n, which were 2, 5, 8, 10, 12 and 62. For this purpose, the manufactured solution was sampled multiple times at $2n+1$ equidistantly placed time instants for each HB simulation, resulting in 5, 11, 17, 21, 25 and 125 data points (samples) per cycle respectively. The samples were applied as initial guesses and BCs in order to drive the flow for the set of harmonically balanced momentum equations (4.3.25). The different velocity fields obtained as numerical solutions from the HB method will be denoted as $\boldsymbol{u}^n_{\mathbf{hb}}$, where n is the number of harmonics used in the expansion. Quantitatively, the solutions $\boldsymbol{u}^n_{\mathbf{hb}}$ were compared with the manufactured solution $\boldsymbol{u}_{\mathbf{ext}}$ in terms of nRMSE($\boldsymbol{u}^n_{\mathbf{hb}}$, $\boldsymbol{u}_{\mathbf{ext}}$), resulting in 13.22%, 2.18%, 0.75%, 0.43%, 0.29% and 0.23% respectively (these results are also summarised in Table 4.1). We observed that at least 8 harmonics are needed for the HB method to recover the velocity field with nRMSE below 1%. The errors rapidly dropped from using 2 to 12 harmonics (from 13.22% to 0.29%), whereas further increase in the number of harmonics over 12 did not drastically improve the flow field. In this case, nRMSE($\boldsymbol{u}^{12}_{\mathbf{hb}}$, $\boldsymbol{u}_{\mathbf{ext}}$) was 0.29%, whereas nRMSE($\boldsymbol{u}^{62}_{\mathbf{hb}}$, $\boldsymbol{u}_{\mathbf{ext}}$) was 0.23%. The HB simulations were run for 1 000 Gauss-Seidel iterations and the WCTs were 217 s, 458 s, 788 s, 960 s, 1 190 s and 10 335 s respectively.

Secondly, the manufactured solution sampled at 25 equidistantly placed time instants was fed into equation (4.3.10) and the PRS method was applied. The obtained flow field will be denoted as $\boldsymbol{u}_{\mathbf{prs}}$, which offers solutions at the same time instants as the flow field $\boldsymbol{u}^{12}_{\mathbf{hb}}$, enabling a direct comparison between HB and PRS with 25 data points per cycle. The PRS simulation was run for 12 periods until a periodic state of equilibrium was reached. Comparison against the exact solution yielded nRMSE($\boldsymbol{u}_{\mathbf{prs}}$, $\boldsymbol{u}_{\mathbf{ext}}$) = 0.03% and the total WCT was 13 737 s. In this case, the error is due to the approximation of the boundary data given by (4.3.10). Table 4.1 summarises the results obtained from both the PRS method and the HB approach using number of harmonics from 2 to 12.

Compared to the velocity field $\boldsymbol{u}^{12}_{\mathbf{hb}}$ obtained from HB, the accuracy of the velocity field $\boldsymbol{u}_{\mathbf{prs}}$ obtained from PRS was higher. It is worth noting, that the PRS method was based on exactly the same PISO solver as the one from which the manufactured solution $\boldsymbol{u}_{\mathbf{ext}}$ was generated

on exactly the same mesh. Hence, the accuracy of the PRS method is the highest that can be expected. However, the WCT for PRS was around 11.5 times more than the WCT for HB with 12 number of harmonics. In total, the PRS method needed ≈ 3.8 hours, whereas the HB method with $n = 12$ needed below 20 minutes.

Finally, regarding the results obtained with the HB method, we conclude that the use of a moderate number of harmonics, e.g. between 8 and 12, is enough to reconstruct the flow field with an acceptable accuracy (errors below 1%). In addition, there is a huge gain in terms of computational effort, which is essential for pulsatile blood flow simulations. Hereafter, we make use of the HB method set with 12 harmonics. The corresponding HB solution is simply referred to as $\boldsymbol{u}_{\mathbf{hb}}$ (instead of $\boldsymbol{u}_{\mathbf{hb}}^{12}$).

Sensitivity to the Mesh Size Parameter

The proposed methods, HB and PRS, were verified in the previous section using a single mesh, on top of which the reference solution was also created. However, this does not realistically emulate a potential real case scenario, in which the observations are usually not obtained from or available in the same geometrical mesh in which the computations are carried out. To further verify the processes (in addition to the study presented in the previous section), a much finer mesh, denoted by $\mathbf{M_7}$, was used in the present section to manufacture the numerical reference solution. The velocity field obtained in such mesh is denoted as $\boldsymbol{u}_{\mathbf{ext}}$, which was sampled at 25 time instants only. Then, this reference solution was mapped to the meshes $\mathbf{M_2}$ and $\mathbf{M_4}$, and the computations using the HB and the PRS methods were performed in these meshes. The reference velocity fields mapped onto $\mathbf{M_2}$ and $\mathbf{M_4}$ are denoted as $\boldsymbol{u}_{\mathbf{ext}}^2$ and $\boldsymbol{u}_{\mathbf{ext}}^4$ respectively. A cell volume weighted interpolation method [Coe05] was used to map the reference velocity field from the fine mesh, $\mathbf{M_7}$, onto the coarser meshes, $\mathbf{M_2}$ and $\mathbf{M_4}$. The simulations with the HB and PRS methods in mesh $\mathbf{M_4}$ were run with 96 processors.

The velocity fields $\boldsymbol{u}_{\mathbf{hb}}$ and $\boldsymbol{u}_{\mathbf{prs}}$ numerically obtained from HB and PRS methods were compared with the exact solution. In mesh $\mathbf{M_2}$, nRMSE($\boldsymbol{u}_{\mathbf{prs}}$, $\boldsymbol{u}_{\mathbf{ext}}^2$) was 2.88%, whereas nRMSE($\boldsymbol{u}_{\mathbf{hb}}$, $\boldsymbol{u}_{\mathbf{ext}}^2$) was 2.93%. In mesh $\mathbf{M_4}$, the same metric evaluated against $\boldsymbol{u}_{\mathbf{ext}}^4$ were 1.47% and 1.51% for PRS and HB methods respectively. Remarkably, the HB method yields almost the same accuracy as the PRS method, when compared with a reference solution constructed in a finer mesh. Furthermore, the error nRMSE($\boldsymbol{u}_{\mathbf{hb}}$, $\boldsymbol{u}_{\mathbf{prs}}$) between these solutions was 0.39% in $\mathbf{M_2}$ and 0.36% in $\mathbf{M_4}$. Despite the differences among the methods, which are negligible, and the approximations provided by the HB can be considered of the same quality as that provided by the PRS. Finally, the WCT in $\mathbf{M_4}$ were 23 052 s for the PRS method and 1 512 s for the HB method, the latter being ≈ 15 times faster than the former. This is a tremendous gain in terms of computational effort, taking into account that the HB method provides a full 3D approximation to the problem. Table 4.2 summarises the presented results.

$\boldsymbol{u}_c$	nRMSE($\boldsymbol{u}_c$, $\boldsymbol{u}^2_{\mathbf{ext}}$) on mesh $\mathbf{M_2}$	nRMSE($\boldsymbol{u}_c$, $\boldsymbol{u}^4_{\mathbf{ext}}$) on mesh $\mathbf{M_4}$	WCT for $\boldsymbol{u}_c$ on mesh $\mathbf{M_4}$
$\boldsymbol{u}_{\mathbf{hb}}$	2.93%	1.51%	1 512 s
$\boldsymbol{u}_{\mathbf{prs}}$	2.88%	1.47%	23 052 s

Table 4.2: Root mean square errors (nRMSE($\boldsymbol{u}_{\mathbf{hb}}, \boldsymbol{u}^n_{\mathbf{ext}}$) and nRMSE($\boldsymbol{u}_{\mathbf{prs}}, \boldsymbol{u}^n_{\mathbf{ext}}$)) for HB and PRS methods, evaluated against the reference solutions $\boldsymbol{u}^2_{\mathbf{ext}}$ and $\boldsymbol{u}^4_{\mathbf{ext}}$ mapped onto meshes $\mathbf{M_2}$ and $\mathbf{M_4}$ respectively. In addition, the corresponding wall clock time (WCT) in seconds is provided for each simulation on $\mathbf{M_4}$, for which 96 processors were employed.

4.4.2 Simulations with Boundary Data from 4-D Flow MRI

The performance and feasibility of both the HB and PRS methods was studied on $\mathbf{M_2}$ to reconstruct the velocity fields obtained from the experiment (see Section 4.2.1). To this end, observational boundary data of the velocity field, obtained from 4D flow MRI acquisition protocol, is prescribed at the inlet. Computed flow patterns were first qualitatively compared by visual inspection. The HB method proved to be able to reproduce the velocity field delivered by the PRS method. Figure 4.2 illustrates the velocity profiles at different cross sections of the arterial geometry (warping of velocity vector field) at the time instant corresponding to the peak of the systole. Qualitatively, there was no appreciable difference between the fields obtained from HB and PRS.

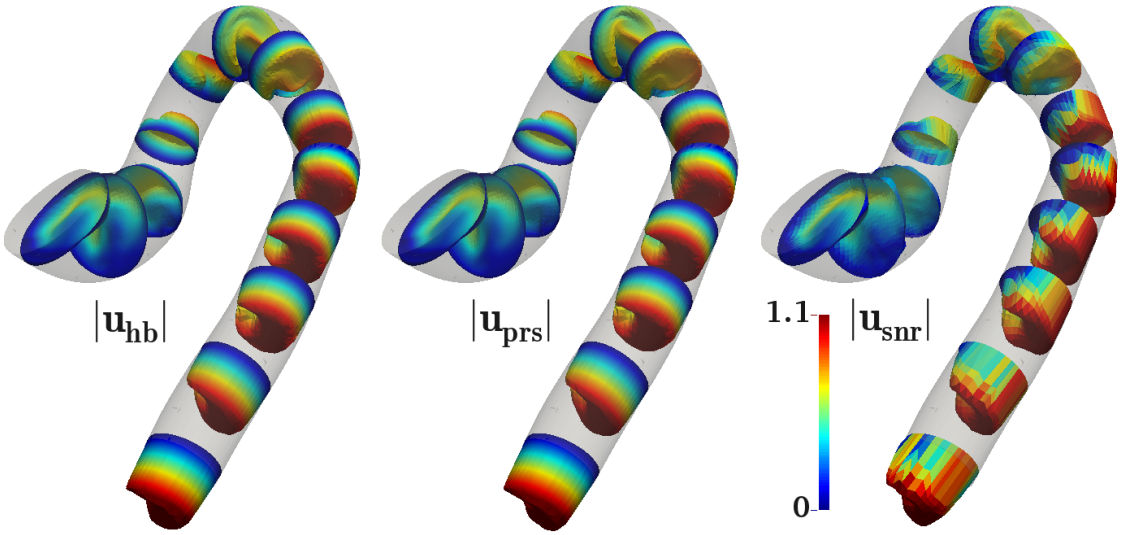

Figure 4.2: Warps and velocity magnitude (in [m/s] scaled to the same range) of the velocity fields at a set of cross-sectional slices corresponding to the systolic phase of the heart cycle. The fields are obtained from HB method (magnitude $|\boldsymbol{u}_{\mathbf{hb}}|$), PRS method (magnitude $|\boldsymbol{u}_{\mathbf{prs}}|$) and pre-processed 4D flow MRI acquisition (magnitude $|\boldsymbol{u}_{\mathbf{snr}}|$).

Finally, since no ground truth is available in the case of measured data, we quantitatively compared the velocity fields delivered by methods HB and PRS, resulting in a metric nRMSE($\boldsymbol{u}_{\mathbf{hb}}$,$\boldsymbol{u}_{\mathbf{prs}}$) of 8.56%. As the simulations were performed on $\mathbf{M_2}$, the computational efforts were the same as already reported for $\mathbf{M_2}$ in the previous sections.

Based on these results, we conclude that the HB numerical scheme reveals itself as a method with a tremendous potential in computational hemodynamics. The proposed approach enables pulsatile fluid flow simulations at a significantly smaller cost when compared with traditional methods, without exhibiting deterioration of the approximate solution.

4.5 Conclusion

This work has investigated the HB method as a novel approach to perform pulsatile fluid flow simulations in computational hemodynamics, facilitating the combination of CFD with data obtained from 4D flow MRI. The HB method has been described and compared with a traditional time-discretisation method to dynamically reconstruct observational boundary data defined at a sparse set of time instants. These methods have been compared in terms of accuracy and computational cost.

The first method, named as the "traditional method using penalized regression spline", is based on a traditional time discretisation scheme and, as such, proves to be a time consuming process. Penalized regression spline presents an inverse problem to continuously reconstruct the boundary velocity data at time instants where the observations are not available.

The second approach, named as the "harmonic balance" method, takes a different path and relies on a frequency-based temporal discretisation scheme. Thereby, the velocity field is decomposed into its Fourier series and the method operates in the frequency domain. Harmonic balance approach is being reported for the first time in a study combining CFD with 4D flow MRI and it shows a significant improvement regarding the trade-off between computational cost and accuracy for applications in computational hemodynamics. Based on our experiments, the harmonic balance method was about 15 times faster compared to the conventional transient simulations.

Our experience dictates that only a moderate number of harmonics is required to accurately resolve the periodic fluid flow problem. This makes the method extremely useful, for example, in data assimilation procedures based on 4D flow MRI acquisitions, where the fluid flow problem has to be solved many times. Regarding the number of time instants at which data is acquired per cardiac cycle, the method can be easily adjusted such that the discretised momentum equations are temporally registered with the measurements. In case of 4D flow MRI, our experience indicates that it requires observational data at a number of time instants between 17 and 25. This corresponds to a number of harmonics of at least 8, which is a region in which the method has proved to be satisfactorily accurate.

5 Fourier-Spectral Dynamic Data Assimilation: Interlacing CFD with 4D flow MRI

5.1 Introduction

In adjoint based data assimilation, the adjoint equations require the solution of the state variables from the original problem. This makes it to a challenge for especially the time dependent problems, where the solution of the state variables must be known at each infinitesimal time step. In time dependent problems, the adjoint equations posses a backward-in-time nature, thus, their solution require to follow a path starting from the last time and ending at the initial time of the considered problem. Hence, when attempting to perform dynamic (adjoint based) data assimilation, all the trajectories of the state variables must be solved and stored in the memory. This can be achieved, for example, using the traditional time-stepping schemes for the solution of the original state equations. However, the necessity for the storage of all trajectories of the state variables and the backward-in-time nature of the adjoint formulation rapidly make it to an extremely difficult problem to be solved. The space needed for the memory is proportional to the run-time of the forward solution. In spite of ever increasing memory capabilities of large clusters, the practical application of the traditional adjoint formulation is quite limited.

In order to manage the difficulties with the storage requirements, the application of certain algorithms have been proposed, usually known as checkpointing [Gri00; Cha01; Cao02]. In such algorithms, the direct problem is first solved to save the solution of the state variables at predefined number of checkpoints, instead of at each infinitesimal time instants. The checkpoints are usually equidistantly placed, however, extensions of such algorithms also consider dynamic checkpointing [Wan09; Aup17]. Thereafter, the direct problem is run for a second time between the two last available checkpoints, where the state variables are then saved at each infinitesimal time steps (between those points). In order to run backwards in time for the adjoint solution, the adjoint equations are solved between the successive checkpoints. Each time the adjoint solution reaches the next available checkpoint, the state variables between the last two checkpoints are then removed from the memory and the process is repeated until the adjoint equations are fully solved. In other words, the direct problem must be solved two times (dynamic forward solution) and the adjoint problem only once, in order to finish a single iteration of the optimisation process. For example, in chapter 4 and table 4.2, it

was reported that approximately 6.5 hours were needed for one forward solution (based on the experimental setup explained in chapter 4). Depending on the size of the computational mesh and the number of time steps needed for an accurate solution, several days might even be needed to accomplish one single iteration of the optimisation process. In addition, several hundreds of iterations are usually required to find an optimal solution (see chapter 2).

So far there has been an attempt to perform variational adjoint-based transient data assimilation in computational hemodynamics using 4D flow MRI measurements in 3D geometries by Funke *et al.* [Fun19]. However, in order to perform a dynamic data assimilation, the authors were forced to extremely reduce the size of the problem (in such a way, that no checkpointing algorithms were required) by considering a coarse mesh and a time step of 0.004625 s. Using such time steps, however, accurate flow simulations cannot be expected at the aortic root and the ascending aorta, where the Reynolds numbers grow large. This is due to the reason, that the blood is pumped by the heart with considerably high velocities. In addition, finer mesh sizes are required for reasonable evaluation of the WSSs. The size-related limitations were already mentioned by the authors in their work. Especially for convection dominated problems with large Reynolds numbers, using the traditional time-stepping schemes for dynamic data assimilation is absolutely impracticable and nearly impossible or difficult to be achieved.

In this work, a new method is proposed to perform variational (adjoint-based) dynamic data assimilation. In contrast to the traditional time-stepping schemes, the novel approach relies on the harmonically balanced equations (as described in chapter 4) expressed in the frequency domain for time discretisation. In what follows, the new method will be referred as the Fourier-spectral dynamic data assimilation.

This work enables accurate characterisation of the dynamic flow field in quite feasible wall clock times, which are otherwise difficult or impossible to be achieved using currently available DA strategies relying on traditional time-stepping schemes. The method naturally avoids storage related problems, and hence, the application of additional algorithms (such as checkpointing) are not required. Further, the work addresses the limited resolution of MR velocity encoding in shear layers and aims to interlace 4D flow MRI with CFD to enable accurate quantification of WSSs. Compared to the raw measurements, the proposed approach significantly improves the reconstructed flow field at the aortic root, which is one of the most important clinically relevant locations where flow disturbances can easily lead to pathological modifications of the arterial wall. Thus the new method has a great potential for revealing clinically relevant hemodynamic phenomena.

5.2 Mathematical Optimisation

An unsteady incompressible flow of a Newtonian fluid is considered in the time interval $\mathbb{T} := [0;T]$ through an open set Ω with boundary $\partial\Omega = \Gamma_i \cup \Gamma_o \cup \Gamma_w$ as illustrated in figure 2.1(a). Let $\Omega_s \subset \Omega$ be a contracted subdomain with boundary $\partial\Omega_s = \Gamma_{si} \cup \Gamma_{so} \cup \Gamma_{sw}$, where $\Gamma_{si} \subset \Gamma_i$

and $\Gamma_{so} \subset \Gamma_o$. Figure 2.1(b) illustrates the contracted domain Ω_s and its formal definition is provided in (2.4.5). The fluid flow is stimulated by some T-periodic inflow data prescribed at Γ_i, which is characterized by the function $\boldsymbol{g} = \boldsymbol{g}(t, \boldsymbol{x}) = \boldsymbol{g}(t + mT, \boldsymbol{x}) : \mathbb{T} \times \Gamma_i \to \mathbb{R}^3$ with $m \in \mathbb{N}$. The blood flow velocity $\boldsymbol{u} \in \boldsymbol{\mathcal{U}}$ with $\boldsymbol{\mathcal{U}} = \left\{ \boldsymbol{v} \in \boldsymbol{H}^1(\Omega) \mid \boldsymbol{v}|_{\Gamma_w} = \boldsymbol{0} \right\}$ is a solution of the incompressible Navier-Stokes equations expressed in the following variational formulation:

$$\begin{aligned}
&\mathscr{P}_{\mathbb{T}\times\Omega}: \text{ Find } (\boldsymbol{u}, p, \boldsymbol{r}) \in \boldsymbol{\mathcal{U}} \times L^2(\Omega) \times \boldsymbol{H}^{-\frac{1}{2}}(\Gamma_i) \text{ such that,} \\
&\int_{\mathbb{T}} \int_{\Omega} \left[\rho \Big(\frac{\partial \boldsymbol{u}}{\partial t} + (\nabla \boldsymbol{u}) \boldsymbol{u} \Big) \cdot \hat{\boldsymbol{u}} + 2\mu \nabla^s \boldsymbol{u} \cdot \nabla^s \hat{\boldsymbol{u}} - p \operatorname{div} \hat{\boldsymbol{u}} - \hat{p} \operatorname{div} \boldsymbol{u} \right] d\Omega dt \qquad (5.2.1) \\
&= \int_{\mathbb{T}} \int_{\Gamma_i} \hat{\boldsymbol{r}} \cdot (\boldsymbol{u} - \boldsymbol{g}) \, d\Gamma dt + \int_{\mathbb{T}} \int_{\Gamma_i} (\boldsymbol{r} \cdot \hat{\boldsymbol{u}}) \, d\Gamma dt \quad \forall \, (\hat{\boldsymbol{u}}, \hat{p}, \hat{\boldsymbol{r}}) \in \boldsymbol{\mathcal{U}} \times L^2(\Omega) \times \boldsymbol{H}^{-\frac{1}{2}}(\Gamma_i) \ .
\end{aligned}$$

The spaces $(\boldsymbol{H}^1(\Omega), L^2(\Omega), \boldsymbol{H}^{-\frac{1}{2}}(\Gamma_i))$, the fluid parameters (ρ, μ) and the strain rate tensor ∇^s are as defined in sections 4.3 and 4.3.1.

Let us assume, that some T-periodic observations $\boldsymbol{u_{obs}} \in \Omega$ are available. The optimal control problem aims at finding the velocity field $\boldsymbol{u}$, such that the sum of the misfits between $\boldsymbol{u_{obs}}$ and $\boldsymbol{u}$ is minimised based on some user defined cost function $\mathscr{O}_{\mathbb{T}\times\Omega}$. At the same time, the problem is constrained such that $\boldsymbol{u}$ is a solution of Problem $\mathscr{P}_{\mathbb{T}\times\Omega}$. In what follows, $\nabla_{\boldsymbol{\tau}}$ denotes the surface gradient, whereas β and β_1 are arbitrary parameters for a Tikhonov regularization, and α is a positive real number. The flow-matching problem reads

$$\begin{aligned}
&\mathscr{P}_O: \text{ Find } \boldsymbol{g} \text{ which minimises } \mathscr{O}_{\mathbb{T}\times\Omega}(\boldsymbol{u}(\boldsymbol{g}), \boldsymbol{g}, \boldsymbol{u_{obs}}) \text{ such that } \mathscr{P}_{\mathbb{T}\times\Omega} \text{ holds, where} \\
&\mathscr{O}_{\mathbb{T}\times\Omega}(\boldsymbol{u}(\boldsymbol{g}), \boldsymbol{g}, \boldsymbol{u_{obs}}) = \frac{\alpha}{2} \left(\int_{\mathbb{T}} \int_{\Omega_s} |\boldsymbol{u}(\boldsymbol{g}) - \boldsymbol{u_{obs}}|^2 \, d\Omega dt + \int_{\mathbb{T}} \int_{\Gamma_{si} \cup \Gamma_{so}} |\boldsymbol{u}(\boldsymbol{g}) - \boldsymbol{u_{obs}}|^2 \, d\Gamma dt \right) + \\
&\quad + \left(\frac{\beta}{2} \int_{\mathbb{T}} \int_{\Gamma_i} |\boldsymbol{g}|^2 \, d\Gamma dt + \frac{\beta_1}{2} \int_{\mathbb{T}} \int_{\Gamma_i} |\nabla_{\boldsymbol{\tau}} \, \boldsymbol{g}|^2 \, d\Gamma dt \right) \ . \qquad (5.2.2)
\end{aligned}$$

The flow-matching metric is defined on Ω_s, Γ_{si} and Γ_{so}, which are considered as the trust region of experimental observations (see figure 2.1(b)). The motivation for the choice of such an objective function, along with the choices of each term, has been provided in section 2.2.1, with the difference that, in the chapter 2, a steady-state fluid flow was considered without the integration over time. The time-dependent problem $\mathscr{P}_O$ defines a regularized optimisation, whose well-posedness has been addressed by Guerra *et al.* [Gue15].

In what follows, we recast the problem of constrained optimisation as a saddle point problem by introducing a Lagrangian functional to relax the dependence of $\boldsymbol{u}$ on $\boldsymbol{g}$. Denoting $\frac{\partial \boldsymbol{u}}{\partial t} = \partial_t \boldsymbol{u}$, the Lagrangian functional reads

$$\begin{aligned}
&\mathscr{L}_{\mathbb{T}\times\Omega}(\boldsymbol{g}, \boldsymbol{u}, p, \boldsymbol{r}, \boldsymbol{\lambda_u}, \boldsymbol{\lambda}_p, \boldsymbol{\lambda_r}) = \mathscr{O}_{\mathbb{T}\times\Omega}(\boldsymbol{u}, \boldsymbol{g}, \boldsymbol{u_{obs}}) - \int_{\mathbb{T}} \int_{\Gamma_i} \boldsymbol{\lambda_r} \cdot (\boldsymbol{u} - \boldsymbol{g}) \, d\Gamma dt - \int_{\mathbb{T}} \int_{\Gamma_i} \boldsymbol{r} \cdot \boldsymbol{\lambda_u} \, d\Gamma dt \\
&\quad + \int_{\mathbb{T}} \int_{\Omega} \left[\rho \Big(\partial_t \boldsymbol{u} + (\nabla \boldsymbol{u}) \boldsymbol{u} \Big) \cdot \boldsymbol{\lambda_u} + 2\mu \nabla^s \boldsymbol{u} \cdot \nabla^s \boldsymbol{\lambda_u} - p \operatorname{div} \boldsymbol{\lambda_u} - \lambda_p \operatorname{div} \boldsymbol{u} \right] d\Omega dt \ , \qquad (5.2.3)
\end{aligned}$$

with $(\boldsymbol{g}, \boldsymbol{u}, p, \boldsymbol{r}, \boldsymbol{\lambda_u}, \lambda_p, \boldsymbol{\lambda_r}) \in \boldsymbol{H}_{00}^{\frac{1}{2}}(\Gamma_i) \times \boldsymbol{\mathcal{U}} \times L^2(\Omega) \times \boldsymbol{H}^{-\frac{1}{2}}(\Gamma_i) \times \boldsymbol{\mathcal{U}} \times L^2(\Omega) \times \boldsymbol{H}^{-\frac{1}{2}}(\Gamma_i)$, where $\boldsymbol{H}_{00}^{\frac{1}{2}}(\Gamma_i)$ is the space of traces over Γ_i of $\boldsymbol{H}^1(\Omega)$ functions that are zero over the boundary γ_i of surface Γ_i. Its noteworthy to highlight the fact that the function $\boldsymbol{g}$ is such that $\boldsymbol{g}|_{\gamma_i} = 0$.

The evaluation of the Gâteaux derivative of $\mathscr{O}_{\mathbb{T}\times\Omega}$ (see equation (2.2.15)), with respect to perturbation in $\boldsymbol{g}$, provides information about the necessary condition to have a minimum at $\boldsymbol{g}$. On the other hand, the critical points of the Lagrangian (5.2.3) contain information on the aforementioned Gâteaux derivative (2.2.15), and are characterised by

$$\left\langle \frac{\partial \mathscr{L}_{\mathbb{T}\times\Omega}}{\partial(\boldsymbol{\lambda_u}, \boldsymbol{\lambda}_p, \boldsymbol{\lambda_r})}, \begin{pmatrix} \hat{\boldsymbol{\lambda}}_{\boldsymbol{u}} \\ \hat{\boldsymbol{\lambda}}_p \\ \hat{\boldsymbol{\lambda}}_{\boldsymbol{r}} \end{pmatrix} \right\rangle = \boldsymbol{0} \ , \quad \left\langle \frac{\partial \mathscr{L}_{\mathbb{T}\times\Omega}}{\partial(\boldsymbol{u}, p, \boldsymbol{r})}, \begin{pmatrix} \hat{\boldsymbol{u}} \\ \hat{p} \\ \hat{\boldsymbol{r}} \end{pmatrix} \right\rangle = \boldsymbol{0} \ , \quad \left\langle \frac{\partial \mathscr{L}_{\mathbb{T}\times\Omega}}{\partial \boldsymbol{g}}, \hat{\boldsymbol{g}} \right\rangle = 0 \ , \tag{5.2.4a–c}$$

where the perturbations $\hat{(\cdot)}$ to the fields $(\cdot)$ are as defined in (2.2.7)–(2.2.13).

The evaluation of the equations (5.2.4a–c) yields the state system of equations, the adjoint equations and the optimality conditions respectively. Similar sets of equations have been derived and solved in the chapter 2 without the presence of the time integration. The discretisation presented in the chapter 2 was only performed spatially, since a time derivative term was not present in the equations, whereas the followed strategy was named as "optimise-then-discretise" approach. In contrast, this chapter presents a transient problem, which makes it necessary to consider an additional discretisation process in time (in addition to the spatial discretisation), in order to solve the equations (5.2.4a–c) numerically.

In what follows, a slightly different strategy will be considered for the adoption of the temporal discretisation, which will be denoted as the "temporally-discretise-then-optimise-then-spatially-discretise" approach.

5.2.1 Temporal Discretisation using the Harmonic Balance Approach

In section 4.3.4, the temporally discretised and harmonically balanced momentum equations (4.3.25) have already been derived based on the Fourier-spectral collocation approach, where n was the number of harmonics and $N = 2n+1$. The application of the HB method in (5.2.3) yields the following temporally discretised Lagrangian functional:

$$\begin{aligned} \mathscr{L}_\Omega(\boldsymbol{g}, \boldsymbol{u}, p, \boldsymbol{r}, \boldsymbol{\lambda_u}, \boldsymbol{\lambda}_p, \boldsymbol{\lambda_r}) = \mathscr{O}_\Omega(\boldsymbol{u}, \boldsymbol{g}, \boldsymbol{u_{obs}}) - \sum_j \int_{\Gamma_i} \boldsymbol{\lambda}_{\boldsymbol{r}}^j \cdot (\boldsymbol{u}^j - \boldsymbol{g}^j)\, d\Gamma - \sum_j \int_{\Gamma_i} \boldsymbol{r}^j \cdot \boldsymbol{\lambda}_{\boldsymbol{u}}^j \, d\Gamma \\ + \sum_j \int_\Omega \Big[\rho \Big(\sum_{i=1}^N \boldsymbol{u}^i c_{ij} + (\nabla \boldsymbol{u}^j)\boldsymbol{u}^j \Big) \cdot \boldsymbol{\lambda}_{\boldsymbol{u}}^j + 2\mu \nabla^s \boldsymbol{u}^j \cdot \nabla^s \boldsymbol{\lambda}_{\boldsymbol{u}}^j - p^j \operatorname{div} \boldsymbol{\lambda}_{\boldsymbol{u}}^j - \lambda_p^j \operatorname{div} \boldsymbol{u}^j \Big] \, d\Omega \ , \end{aligned} \tag{5.2.5}$$

where $\mathscr{O}_\Omega$ is the temporally discretised cost function (provided in (5.2.7)) and $(\cdot)^j$ represent the fields $(\cdot)$ at time instants

$$t_j := \frac{j\,T}{N}, \quad j = 1, 2, \cdots, N. \tag{5.2.6}$$

Furthermore, $c_{ij} = \frac{2\omega}{N}\sum_{k=1}^{n} k\sin(k\omega(t_i - t_j))$ is as derived in section 4.3.4 (see equation (4.3.24)), where $\omega = \frac{2\pi}{T}$ is the angular frequency.

Assuming that some observations $\boldsymbol{u}^j_{\mathbf{obs}} \in \Omega$ are available at discrete and equidistantly spaced time instants t_j (in case of 4D flow MRI, such data are actually gathered from T-periodic averaging of the measurements to obtain $\boldsymbol{u}^j_{\mathbf{obs}}$ at time instants t_j for $j = 1, \cdots, N$). The constratined optimal control problem now aims at finding the velocity fields $\boldsymbol{u}^j$, such that the sum of the misfits between each $\boldsymbol{u}^j_{\mathbf{obs}}$ and $\boldsymbol{u}^j$ is minimised based on the temporally discretised cost function

$$\begin{aligned}\mathscr{O}_\Omega(\boldsymbol{u}(\boldsymbol{g}), \boldsymbol{g}, \boldsymbol{u}_{\mathbf{obs}}) = \frac{\alpha}{2}\sum_j \left(\int_{\Omega_s} |\boldsymbol{u}^j(\boldsymbol{g}) - \boldsymbol{u}^j_{\mathbf{obs}}|^2\, d\Omega + \int_{\Gamma_{si}\cup\Gamma_{so}} |\boldsymbol{u}^j(\boldsymbol{g}) - \boldsymbol{u}^j_{\mathbf{obs}}|^2\, d\Gamma\right) + \\ + \sum_j \left(\frac{\beta}{2}\int_{\Gamma_i} |\boldsymbol{g}^j|^2\, d\Gamma + \frac{\beta_1}{2}\int_{\Gamma_i} |\nabla_{\boldsymbol{\tau}}\, \boldsymbol{g}^j|^2\, d\Gamma\right)\ .\end{aligned} \tag{5.2.7}$$

Finally, we are now interested in computing the Gâteaux derivatives of the temporally discretised Lagrangian functional, as follows:

$$\left\langle \frac{\partial \mathscr{L}_\Omega}{\partial(\boldsymbol{\lambda}^j_{\boldsymbol{u}}, \boldsymbol{\lambda}^j_p, \boldsymbol{\lambda}^j_{\boldsymbol{r}})}, \begin{pmatrix} \hat{\boldsymbol{\lambda}}^j_{\boldsymbol{u}} \\ \hat{\boldsymbol{\lambda}}^j_p \\ \hat{\boldsymbol{\lambda}}^j_{\boldsymbol{r}} \end{pmatrix} \right\rangle = \mathbf{0}\ , \quad \left\langle \frac{\partial \mathscr{L}_\Omega}{\partial(\boldsymbol{u}^j, p^j, \boldsymbol{r}^j)}, \begin{pmatrix} \hat{\boldsymbol{u}}^j \\ \hat{p}^j \\ \hat{\boldsymbol{r}}^j \end{pmatrix} \right\rangle = \mathbf{0}\ , \quad \left\langle \frac{\partial \mathscr{L}_\Omega}{\partial \boldsymbol{g}^j}, \hat{\boldsymbol{g}}^j \right\rangle = 0\ . \tag{5.2.8a–c}$$

For $j = 1, 2, \cdots, N$, the first and second equations in (5.2.8a–c) describe the direct and the so-called adjoint equations to solve for the state variables $(\boldsymbol{u}^j, p^j, \boldsymbol{r}^j)$ and the adjoint variables $(\boldsymbol{\lambda}^j_{\boldsymbol{u}}, \boldsymbol{\lambda}^j_p, \boldsymbol{\lambda}^j_{\boldsymbol{r}})$ respectively. Finally, the last equation in (5.2.8a–c) provides the optimality conditions of the cost functional with respect to perturbations in $\boldsymbol{g}^j$. In particular, it can be observed that the Gâteaux derivatives of the objective functional are contained in the Gâteaux derivatives of the Lagrangian functional as follows:

$$\left\langle \frac{\partial \mathscr{O}_\Omega}{\partial \boldsymbol{g}^j}, \hat{\boldsymbol{g}}^j \right\rangle = \left\langle \frac{\partial \mathscr{L}_\Omega}{\partial \boldsymbol{g}^j}, \hat{\boldsymbol{g}}^j \right\rangle \Bigg|_{\substack{(\boldsymbol{u}^j, p^j, \boldsymbol{r}^j) \text{ solution of direct problem} \\ (\boldsymbol{\lambda}^j_{\boldsymbol{u}}, \lambda^j_p, \boldsymbol{\lambda}^j_{\boldsymbol{r}}) \text{ solution of adjoint problem}}}\ , \quad j = 1, 2, \cdots, N\ . \tag{5.2.9}$$

5.2.2 Optimality Conditions

Derivation of the Direct Problem

Let us now compute the Gâteaux derivatives (5.2.8a–c). We first obtain the direct problem by taking the derivative with respect to the variables $(\boldsymbol{\lambda}_{\boldsymbol{u}}^j, \lambda_p^j, \boldsymbol{\lambda}_{\boldsymbol{r}}^j)$. Then, the following state problems are obtained for $j = 1, 2, \cdots, N$:

$\mathscr{P}_{\text{sta}}^j(\boldsymbol{g}^j, \boldsymbol{u}^i)$: For $\boldsymbol{g}^j \in \boldsymbol{H}_{00}^{\frac{1}{2}}(\Gamma_i)$ and $\boldsymbol{u}^i \in \boldsymbol{\mathcal{U}}$, where $i = 1, 2, \cdots, N$ with $i \neq j$, determine $(\boldsymbol{u}^j, p^j, \boldsymbol{r}^j) \in \boldsymbol{\mathcal{U}} \times L^2(\Omega) \times \boldsymbol{H}^{-\frac{1}{2}}(\Gamma_i)$ such that

$$\left\langle \frac{\partial \mathscr{L}_\Omega}{\partial \boldsymbol{\lambda}_{\boldsymbol{u}}^j}, \hat{\boldsymbol{\lambda}}_{\boldsymbol{u}}^j \right\rangle = \int_\Omega \Big[\rho\Big(\sum_{i=1}^N \boldsymbol{u}^i c_{ij} + (\nabla \boldsymbol{u}^j)\boldsymbol{u}^j\Big) \cdot \hat{\boldsymbol{\lambda}}_{\boldsymbol{u}}^j + 2\mu \nabla^s \boldsymbol{u}^j \cdot \nabla^s \hat{\boldsymbol{\lambda}}_{\boldsymbol{u}}^j - p^j \operatorname{div} \hat{\boldsymbol{\lambda}}_{\boldsymbol{u}}^j\Big] d\Omega - \int_{\Gamma_i} \boldsymbol{r}^j \cdot \hat{\boldsymbol{\lambda}}_{\boldsymbol{u}}^j \, d\Gamma = 0 \qquad \forall\, \hat{\boldsymbol{\lambda}}_{\boldsymbol{u}}^j \in \boldsymbol{\mathcal{U}} \ , \tag{5.2.10}$$

$$\left\langle \frac{\partial \mathscr{L}_\Omega}{\partial \lambda_p^j}, \hat{\lambda}_p^j \right\rangle = -\int_\Omega \hat{\lambda}_p^j \operatorname{div} \boldsymbol{u}^j \, d\Omega = 0 \qquad \forall\, \hat{\lambda}_p^j \in L^2(\Omega) \ , \tag{5.2.11}$$

$$\left\langle \frac{\partial \mathscr{L}_\Omega}{\partial \boldsymbol{\lambda}_{\boldsymbol{r}}^j}, \hat{\boldsymbol{\lambda}}_{\boldsymbol{r}}^j \right\rangle = -\int_{\Gamma_i} \hat{\boldsymbol{\lambda}}_{\boldsymbol{r}}^j \cdot (\boldsymbol{u}^j - \boldsymbol{g}^j) \, d\Gamma = 0 \qquad \forall\, \hat{\boldsymbol{\lambda}}_{\boldsymbol{r}}^j \in \boldsymbol{H}^{-\frac{1}{2}}(\Gamma_i) \ . \tag{5.2.12}$$

Integrating by parts in equation (5.2.10) yields

$$\left\langle \frac{\partial \mathscr{L}_\Omega}{\partial \boldsymbol{\lambda}_{\boldsymbol{u}}^j}, \hat{\boldsymbol{\lambda}}_{\boldsymbol{u}}^j \right\rangle = \int_\Omega \Big[\rho\Big(\sum_{i=1}^N \boldsymbol{u}^i c_{ij} + (\nabla \boldsymbol{u}^j)\boldsymbol{u}^j\Big) \cdot \hat{\boldsymbol{\lambda}}_{\boldsymbol{u}}^j + -\mu \Delta \boldsymbol{u}^j \cdot \hat{\boldsymbol{\lambda}}_{\boldsymbol{u}}^j + \nabla p^j \cdot \hat{\boldsymbol{\lambda}}_{\boldsymbol{u}}^j\Big] d\Omega + \int_{\partial\Omega} \Big[-p^j \boldsymbol{n} + 2\mu(\nabla^s \boldsymbol{u}^j)\boldsymbol{n}\Big] \cdot \hat{\boldsymbol{\lambda}}_{\boldsymbol{u}}^j \, d\Gamma - \int_{\Gamma_i} \boldsymbol{r}^j \cdot \hat{\boldsymbol{\lambda}}_{\boldsymbol{u}}^j \, d\Gamma = 0 \qquad \forall\, \hat{\boldsymbol{\lambda}}_{\boldsymbol{u}}^j \in \boldsymbol{\mathcal{U}}, \tag{5.2.13}$$

The Euler-Lagrange equations associated with the variational problem $\mathscr{P}_{\text{sta}}^j$ are the following Navier-Stokes equations, discretised in time based on the HB method:

$$\rho \textstyle\sum_{i=1}^N \boldsymbol{u}^i c_{ij} + \rho(\nabla \boldsymbol{u}^j)\boldsymbol{u}^j - \mu \Delta \boldsymbol{u}^j + \nabla p^j = \boldsymbol{0} \quad \text{in } \Omega \ , \tag{5.2.14}$$

$$\operatorname{div} \boldsymbol{u}^j = 0 \quad \text{in } \Omega \ , \tag{5.2.15}$$

$$\boldsymbol{u}^j = \boldsymbol{0} \quad \text{on } \Gamma_w \ , \tag{5.2.16}$$

$$\boldsymbol{u}^j = \boldsymbol{g}^j \quad \text{on } \Gamma_i \ , \tag{5.2.17}$$

$$(-p^j \boldsymbol{I} + 2\mu \nabla^s \boldsymbol{u}^j)\boldsymbol{n} = \boldsymbol{r}^j \quad \text{on } \Gamma_i \ , \tag{5.2.18}$$

$$(-p^j \boldsymbol{I} + 2\mu \nabla^s \boldsymbol{u}^j)\boldsymbol{n} = \boldsymbol{0} \quad \text{on } \Gamma_o \ , \tag{5.2.19}$$

$$j = 1, \cdots, N \ .$$

Derivation of the Adjoint Problem

Second, the adjoint problem is obtained by taking the derivative of the Lagrangian (5.2.5) with respect to the state variables $(\boldsymbol{u}^j, p^j, \boldsymbol{r}^j)$ for $j = 1, 2, \cdots, N$. That is, the critical points

in the second equation in (5.2.8a–c) are evaluated and the adjoint problem then reads as

$$\mathscr{P}^j_{\text{adj}}(\boldsymbol{u}^j, \boldsymbol{u}^j_{\mathbf{obs}}): \text{ For } \boldsymbol{u}^j_{\mathbf{obs}}, \text{ and } \boldsymbol{u}^j, \text{ solution of (5.2.14)–(5.2.19)},$$

$$\text{determine } (\boldsymbol{\lambda}^j_{\boldsymbol{u}}, \lambda^j_p, \boldsymbol{\lambda}^j_{\boldsymbol{r}}) \in \boldsymbol{\mathcal{U}} \times L^2(\Omega) \times \boldsymbol{H}^{-\frac{1}{2}}(\Gamma_i), \text{ such that}$$

$$\begin{aligned}\left\langle \frac{\partial \mathscr{L}_\Omega}{\partial \boldsymbol{u}^j}, \hat{\boldsymbol{u}}^j \right\rangle &= \int_{\Gamma_o \cup \Gamma_i} \left[\alpha\,(\chi_{\Gamma_{so}} + \chi_{\Gamma_{si}})(\boldsymbol{u}^j - \boldsymbol{u}^j_{\mathbf{obs}}) \cdot \hat{\boldsymbol{u}}^j\right] d\Gamma - \int_{\Gamma_i} \left(\boldsymbol{\lambda}^j_{\boldsymbol{r}} \cdot \hat{\boldsymbol{u}}^j\right) d\Gamma \\ &+ \int_\Omega \Big[\alpha\,\chi_{\Omega_s}(\boldsymbol{u}^j - \boldsymbol{u}^j_{\mathbf{obs}}) \cdot \hat{\boldsymbol{u}}^j + \rho\Big(\sum_{i=1}^N c_{ji}\hat{\boldsymbol{u}}^j + (\nabla \hat{\boldsymbol{u}}^j)\boldsymbol{u}^j + (\nabla \boldsymbol{u}^j)\hat{\boldsymbol{u}}^j\Big) \cdot \boldsymbol{\lambda}^j_{\boldsymbol{u}} + \\ &+ 2\mu \nabla^s \hat{\boldsymbol{u}}^j \cdot \nabla^s \boldsymbol{\lambda}^j_{\boldsymbol{u}} - \lambda^j_p \operatorname{div} \hat{\boldsymbol{u}}^j\Big]\, d\Omega = 0 \qquad \forall\, \hat{\boldsymbol{u}}^j \in \boldsymbol{\mathcal{U}}\ , \end{aligned} \tag{5.2.20}$$

$$\left\langle \frac{\partial \mathscr{L}_\Omega}{\partial p^j}, \hat{p}^j \right\rangle = -\int_\Omega \hat{p}^j \operatorname{div} \boldsymbol{\lambda}^j_{\boldsymbol{u}}\, d\Omega = 0 \qquad \forall\, \hat{p}^j \in L^2(\Omega)\ , \tag{5.2.21}$$

$$\left\langle \frac{\partial \mathscr{L}_\Omega}{\partial \boldsymbol{r}^j}, \hat{\boldsymbol{r}}^j \right\rangle = -\int_{\Gamma_i} \hat{\boldsymbol{r}}^j \cdot \boldsymbol{\lambda}^j_{\boldsymbol{u}}\, d\Gamma = 0 \qquad \forall\, \hat{\boldsymbol{r}}^j \in \boldsymbol{H}^{-\frac{1}{2}}(\Gamma_i)\ , \tag{5.2.22}$$

where we considered the indicator functions χ_{Ω_s}, $\chi_{\Gamma_{si}}$ and $\chi_{\Gamma_{so}}$ as defined in (2.2.32a–c). Applying standard variational arguments for (5.2.20)-(5.2.21)-(5.2.22) delivers the associated Euler-Lagrange equations, as follows:

$$\rho\Big[\Big(\textstyle\sum_{i=1}^N c_{ji} + (\nabla \boldsymbol{u}^j)^T\Big)\boldsymbol{\lambda}^j_{\boldsymbol{u}} - (\nabla \boldsymbol{\lambda}^j_{\boldsymbol{u}})\boldsymbol{u}^j\Big] - \mu\Delta\boldsymbol{\lambda}^j_{\boldsymbol{u}} + \nabla\lambda^j_p = \alpha\,\chi_{\Omega_s}(\boldsymbol{u}^j_{\mathbf{obs}} - \boldsymbol{u}^j) \quad \text{in } \Omega\ , \tag{5.2.23}$$

$$\operatorname{div} \boldsymbol{\lambda}^j_{\boldsymbol{u}} = 0 \qquad \text{in } \Omega\ , \tag{5.2.24}$$

$$\boldsymbol{\lambda}^j_{\boldsymbol{u}} = \mathbf{0} \qquad \text{on } \Gamma_w\ , \tag{5.2.25}$$

$$\boldsymbol{\lambda}^j_{\boldsymbol{u}} = \mathbf{0} \qquad \text{on } \Gamma_i\ , \tag{5.2.26}$$

$$(2\mu\nabla^s\boldsymbol{\lambda}^j_{\boldsymbol{u}} - \lambda^j_p\boldsymbol{I})\boldsymbol{n} - \boldsymbol{\lambda}^j_{\boldsymbol{r}} = \alpha\,\chi_{\Gamma_{si}}(\boldsymbol{u}^j_{\mathbf{obs}} - \boldsymbol{u}^j) \qquad \text{on } \Gamma_i\ , \tag{5.2.27}$$

$$\rho(\boldsymbol{u}^j \cdot \boldsymbol{n})\boldsymbol{\lambda}^j_{\boldsymbol{u}} + (2\mu\nabla^s\boldsymbol{\lambda}^j_{\boldsymbol{u}} - \lambda^j_p\boldsymbol{I})\boldsymbol{n} = \alpha\,\chi_{\Gamma_{so}}(\boldsymbol{u}^j_{\mathbf{obs}} - \boldsymbol{u}^j) \qquad \text{on } \Gamma_o\ . \tag{5.2.28}$$

$$j = 1, \cdots, N\ .$$

Derivation of the Optimality Condition

Finally, let us compute the optimality condition by taking the derivative of the Lagrangian (5.2.5) with respect to the control variables $\boldsymbol{g}^j$. That is, the critical points in the last equation in (5.2.8a–c) are evaluated and results in the problem

$$\mathscr{P}^j_{\text{opt}}(\boldsymbol{\lambda}^j_{\boldsymbol{r}}): \text{ For } \boldsymbol{\lambda}^j_{\boldsymbol{r}}, \text{ solution of (5.2.23)–(5.2.28)}, \text{ determine } \boldsymbol{g}^j \in \boldsymbol{H}^{\frac{1}{2}}_{00}(\Gamma_i), \text{ such that}$$

$$\left\langle \frac{\partial \mathscr{L}_\Omega}{\partial \boldsymbol{g}^j}, \hat{\boldsymbol{g}}^j \right\rangle = \int_{\Gamma_i} \left[\beta \boldsymbol{g}^j \cdot \hat{\boldsymbol{g}}^j + \beta_1 \nabla_{\boldsymbol{\tau}} \boldsymbol{g}^j \cdot \nabla_{\boldsymbol{\tau}} \hat{\boldsymbol{g}}^j + \boldsymbol{\lambda}^j_{\boldsymbol{r}} \cdot \hat{\boldsymbol{g}}^j\right] d\Gamma = 0 \quad \forall\, \hat{\boldsymbol{g}}^j \in \boldsymbol{H}^{\frac{1}{2}}(\Gamma_i)\ . \tag{5.2.29}$$

The Euler-Lagrange equations associated with (5.2.29) are the following:

$$\beta \boldsymbol{g}^j - \beta_1 \triangle_{\boldsymbol{\tau}} \boldsymbol{g}^j = -\boldsymbol{\lambda}_{\boldsymbol{r}}^j \qquad \text{on } \Gamma_i \ , \tag{5.2.30}$$

$$\boldsymbol{g}^j = \boldsymbol{0} \qquad \text{on } \gamma_i \ , \tag{5.2.31}$$

$$j = 1, \cdots, N \ .$$

5.2.3 Gradient Descent Algorithm for Dynamic Data Assimilation

The procedure to solve the optimality conditions at once amounts to solving the nonlinear system of coupled variational equations $\mathscr{P}^j_{\text{sta}}$, $\mathscr{P}^j_{\text{adj}}$ and $\mathscr{P}^j_{\text{opt}}$ (or their corresponding Euler-Lagrange equations (5.2.14)–(5.2.19), (5.2.23)–(5.2.28) and (5.2.30)–(5.2.31)). This problem is nonlinear and a possible way to find the stationary point for the optimisation problem $\mathscr{P}_O$ is to evaluate the Gâteaux derivatives (5.2.9) to drive a descent-like iterative algorithm. In this case, first, given the guesses $\boldsymbol{g}^j$ for $j = 1, 2, \cdots, N$, the forward problem $\mathscr{P}^j_{\text{sta}}$ is solved to obtain the state variables, $(\boldsymbol{u}^j, p^j, \boldsymbol{r}^j)$. Second, the adjoint problem, $\mathscr{P}^j_{\text{adj}}$, is evaluated using the solutions, $\boldsymbol{u}^j$, from the direct problem. At this stage, in order to achieve a faster computation of the adjoint states, the summation term $\sum_{i=1}^{N} c_{ji}$ in the adjoint momentum equation (5.2.23) has been suppressed in the implementation, since the final solution was not remarkably affected by this term. Then, using the adjoint variables, $\boldsymbol{\lambda}_{\boldsymbol{r}}^j$, obtained from the adjoint problem, the gradients of the objective function with respect to the parameters $\boldsymbol{g}^j$ can be calculated from (5.2.29) as follows:

$$\frac{D\mathscr{O}_\Omega}{D\boldsymbol{g}^j} = \beta \boldsymbol{g}^j - \beta_1 \triangle_{\boldsymbol{\tau}} \boldsymbol{g}^j + \boldsymbol{\lambda}_{\boldsymbol{r}}^j \quad \text{on } \Gamma_i \ . \tag{5.2.32}$$

To ensure an acceptable converging solution of the algorithm, it is usual to start by solving the forward problem based on some initial guesses, $(\boldsymbol{u}^j)^{\{0\}}$, for the flow fields at time instats t_j. Therefore, we introduce a proper linearisation, $\mathscr{P}^j_{\text{sta-lin}}$, of the forward problem, $\mathscr{P}^j_{\text{sta}}$, as

$\mathscr{P}^j_{\text{sta-lin}}(\tilde{\boldsymbol{u}}^j, \tilde{\boldsymbol{g}}^j, \boldsymbol{u}^i)$: For $\tilde{\boldsymbol{u}}^j, \tilde{\boldsymbol{g}}^j$ and $\boldsymbol{u}^i$, where $i = 1, 2, \cdots, N$ with $i \neq j$,
determine $(\boldsymbol{u}^j, p^j, \boldsymbol{r}^j)$ such that

$$\left\langle \frac{\partial \mathscr{L}_\Omega}{\partial \boldsymbol{\lambda}_{\boldsymbol{u}}^j}, \hat{\boldsymbol{\lambda}}_{\boldsymbol{u}}^j \right\rangle = \int_\Omega \left[\rho \sum_{i=1}^{N} \boldsymbol{u}^i c_{ij} \cdot \hat{\boldsymbol{\lambda}}_{\boldsymbol{u}}^j + \rho (\nabla \boldsymbol{u}^j) \tilde{\boldsymbol{u}}^j \cdot \hat{\boldsymbol{\lambda}}_{\boldsymbol{u}}^j + 2\mu \nabla^s \boldsymbol{u}^j \cdot \nabla^s \hat{\boldsymbol{\lambda}}_{\boldsymbol{u}}^j \right] d\Omega$$

$$- \int_\Omega p^j \operatorname{div} \hat{\boldsymbol{\lambda}}_{\boldsymbol{u}}^j - \int_{\Gamma_i} \boldsymbol{r}^j \cdot \hat{\boldsymbol{\lambda}}_{\boldsymbol{u}}^j \, d\Gamma = 0 \qquad \forall \, \hat{\boldsymbol{\lambda}}_{\boldsymbol{u}}^j \in \boldsymbol{\mathcal{U}} \ , \tag{5.2.33}$$

$$\left\langle \frac{\partial \mathscr{L}_\Omega}{\partial \lambda_p^j}, \hat{\lambda}_p^j \right\rangle = - \int_\Omega \hat{\lambda}_p^j \operatorname{div} \boldsymbol{u}^j \, d\Omega = 0 \qquad \forall \, \hat{\lambda}_p^j \in L^2(\Omega) \ , \tag{5.2.34}$$

$$\left\langle \frac{\partial \mathscr{L}_\Omega}{\partial \boldsymbol{\lambda}_{\boldsymbol{r}}^j}, \hat{\boldsymbol{\lambda}}_{\boldsymbol{r}}^j \right\rangle = - \int_{\Gamma_i} \hat{\boldsymbol{\lambda}}_{\boldsymbol{r}}^j \cdot (\boldsymbol{u}^j - \tilde{\boldsymbol{g}}^j) \, d\Gamma = 0 \qquad \forall \, \hat{\boldsymbol{\lambda}}_{\boldsymbol{r}}^j \in \boldsymbol{H}^{-\frac{1}{2}}(\Gamma_i) \ . \tag{5.2.35}$$

The optimality conditions (5.2.29) ensure that the derivatives of the objective functional

Algorithm 3 Multiple steepest descent optimisation with dynamic step sizes

Given : $\alpha, \beta, \beta_1 > 0$ ▷ Set optimisation parameters
Input : $N = 2n + 1$ ▷ Provide number of harmonics n
$j = 1, 2, \cdots, N$ ▷ Indices of equidistantly placed time instants t_j
$(\boldsymbol{u}^j)^{\{0\}}, (\boldsymbol{g}^j)^{\{0\}}, \boldsymbol{u}^j_{\mathbf{obs}}$ ▷ Provide initial guesses $(\cdot)^{\{0\}}$ and target fields
Output : $\boldsymbol{u}^{\{k\}}$ ▷ Flow field at last iteration k

procedure DynamicDataAssimilation($\boldsymbol{u}^{\{0\}}, \boldsymbol{g}^{\{0\}}, \boldsymbol{u}_{\mathbf{obs}}, N$)
  $\xi \leftarrow 10^{-8}$, $k \leftarrow 0$ and $\sigma^j \leftarrow 1$ for $j = 1, 2, \cdots, N$
  for $j \leftarrow 1, N$ **do**
    $((\boldsymbol{u}^j)^{\{k\}}, \cdot, \cdot) \leftarrow \mathscr{P}^j_{\text{sta-lin}}((\boldsymbol{u}^j)^{\{0\}}, (\boldsymbol{g}^j)^{\{0\}}, \boldsymbol{u}^i)$ ▷ Evaluate (5.2.33)–(5.2.35)
    update $\boldsymbol{u}^i$ using new $(\boldsymbol{u}^j)^{\{k\}}$ for $i = j$
  end for
  $cost^{\{k\}} \leftarrow \mathscr{O}_\Omega(\boldsymbol{u}^{\{k\}}, \boldsymbol{g}^{\{0\}}, \boldsymbol{u}_{\mathbf{obs}})$ ▷ Evaluate cost function (5.2.7)
  for $k \leftarrow 1, \infty$ **do**
    $converged \leftarrow$ **true**
    for $j \leftarrow 1, N$ **do**
      $(\cdot, \cdot, (\boldsymbol{\lambda}^j_{\boldsymbol{r}})^{\{k\}}) \leftarrow \mathscr{P}^j_{\text{adj}}((\boldsymbol{u}^j)^{\{k-1\}}, \boldsymbol{u}^j_{\mathbf{obs}})$ ▷ Evaluate problem (5.2.23)–(5.2.28)
      $(\boldsymbol{s}^j)^{\{k\}} \leftarrow \beta_1 \triangle_{\boldsymbol{r}} (\boldsymbol{g}^j)^{\{k-1\}} - \beta (\boldsymbol{g}^j)^{\{k-1\}} - (\boldsymbol{\lambda}^j_{\boldsymbol{r}})^{\{k\}}$ ▷ Set steepest descent (5.2.32)
      repeat
        $(\boldsymbol{g}^j)^{\{k\}} \leftarrow (\boldsymbol{g}^j)^{\{k-1\}} + \sigma^j (\boldsymbol{s}^j)^{\{k\}}$ ▷ Update control, using step size σ^j
        $((\boldsymbol{u}^j)^{\{k\}}, \cdot, \cdot) \leftarrow \mathscr{P}^j_{\text{sta-lin}}((\boldsymbol{u}^j)^{\{k-1\}}, (\boldsymbol{g}^j)^{\{k\}}, \boldsymbol{u}^i)$
        $cost^{\{k\}} \leftarrow \mathscr{O}_{\mathbb{T}}(\boldsymbol{u}^{\{k\}}, \boldsymbol{g}^{\{k\}}, \boldsymbol{u}_{\mathbf{obs}})$
        if $cost^{\{k\}} \geq cost^{\{k-1\}}$ **then**
          $\sigma^j \leftarrow 0.5\sigma^j$
        end if
      until $cost^{\{k\}} < cost^{\{k-1\}}$
      if $(\left|cost^{\{k\}} - cost^{\{k-1\}}\right|)/(cost^{\{k\}}) > \xi$ **then**
        $\sigma^j \leftarrow 1.5\sigma^j$
        $converged \leftarrow$ **false**
      end if
      update $\boldsymbol{u}^i$ using new $(\boldsymbol{u}^j)^{\{k\}}$ for $i = j$
    end for
    if $(converged)$ **then**
      return $\boldsymbol{u}^{\{k\}}$
    end if
  end for
end procedure

with respect to the control parameters vanish at the critical points. In the gradient descent algorithm, however, the optimality conditions are not satisfied until the algorithm converges. That procedure is described in algorithm 3. The fields $(\cdot)^{\{k\}}$ correspond to the fields $(\cdot)$ at the k-th iteration. The parameters σ^j, being adjusted dynamically, represent the step sizes for the j-th harmonic balance iteration of each optimisation procedure. To test the convergence, a tolerance parameter ξ is prescribed to exit the algorithm, if necessary.

It should be noted, that the spatial discretisation of the equations described in the present chapter and the numerical methods applied to solve the aforementioned problems are the same as presented in the chapter 2 in section 2.2.4.

5.3 Results

Numerical computations are performed using the same computational mesh geometries $\mathbf{M_2}$, $\mathbf{M_4}$ and $\mathbf{M_7}$ introduced in section 4.2.2. The combination of the HB method with the inverse problem proposed in section 5.2, is analysed in terms of accuracy and computational effort.

The ground truth data are available flow fields, which have been numerically manufactured as detailed in section 4.4.1. First, the validation is performed relying on two quantitative error evaluations between the ground truth data and the computed solutions based on different mesh sizes. The first quantity for the error computation is the root mean square error (normalised against the reference solution),

$$\mathrm{nRMSE}^X(\boldsymbol{u}_c, \boldsymbol{u}_r) = \left(\frac{100}{\underset{\mathbb{T},X}{\mathrm{avr}} |\boldsymbol{u}_r|} \right) \sqrt{\frac{1}{V_X \cdot T} \int_{\mathbb{T}} \int_X |\boldsymbol{u}_c - \boldsymbol{u}_r|^2 \, dX \, dt} \ , \tag{5.3.1}$$

where T is the period, X is the domain with volume V_X, in which the error is being evaluated, $\boldsymbol{u}_c$ is some computed field and $\boldsymbol{u}_r$ is the reference solution. The second quantity for the error computation is the flow direction error

$$\mathrm{FDE}^X(\boldsymbol{u}_c, \boldsymbol{u}_r) = \sqrt{\frac{1}{V_X \cdot T} \int_{\mathbb{T}} \int_X \left(1 - \frac{\boldsymbol{u}_c \cdot \boldsymbol{u}_r}{|\boldsymbol{u}_c||\boldsymbol{u}_r|} \right)^2 dX dt} \ . \tag{5.3.2}$$

The flow fields obtained from the HB method combined with the proposed inverse problem will be denoted as $\boldsymbol{u}_{\mathbf{hb}}^{\mathbf{opt}}$ (in the sense of adopting the HB method in the optimisation process). In addition, the HB approach is also evaluated as a conventional forward method without considering the inverse problem, whereas the flow fields obtained in that way will be denoted as $\boldsymbol{u}_{\mathbf{hb}}^{\mathbf{for}}$ (in the sense of adopting the HB method only for a single conventional forward solution). Both fields are compared with the same ground truth data in terms of (5.3.1) and (5.3.2).

Furthermore, the proposed inverse problem and the forward problem are applied along with some observations, which have been obtained from real 4D flow MRI measurements (as described in section 4.2.1). The flow field, $\boldsymbol{u}_{\mathbf{hb}}^{\mathbf{opt}}$, obtained from the assimilation process against

the real acquisitions, and the field, $\boldsymbol{u}_{\mathbf{hb}}^{\mathbf{for}}$, obtained from the forward solution, are both compared with the measured flow field by visual inspection. In addition to such qualitative analysis, the fields $\boldsymbol{u}_{\mathbf{hb}}^{\mathbf{opt}}$ and $\boldsymbol{u}_{\mathbf{hb}}^{\mathbf{for}}$ are also quantitatively compared with each other to demonstrate the extent of their differences.

Finally, it is worth to note that all the preprocessing steps, as described in section 2.3, were also applied in this chapter to the corresponding observations.

5.3.1 Validation

Based on some artificially generated flow MRI data, the proposed approach is first validated by comparing its solution against a numerical reference solution, which represents the ground truth. For the purpose of realistically mimicking an experimental set-up of a conventional CFD-MRI based study, three different domains are considered, which will be labeled as the world domain, the MRI domain and the CFD domain. In a real-case scenario, the world domain would represent the patient-specific and infinitely resolved flow field in a human aorta, whereas the MRI domain represents the measured noisy flow field in a coarsely resolved grid (usually with a voxel-size of 2 mm isotrop as described in section 2.5.2). Finally, the CFD domain corresponds to a computational mesh for the numerical simulations, which is conceivably finer than the grid in the MRI domain (but of course much coarser than the resolution of the world domain). Since an infinite resolution can not be afforded, the finest available mesh, $\mathbf{M_7}$, is used in the present section as a representative of the world domain. In addition, the meshes $\mathbf{M_2}$ and $\mathbf{M_4}$ are used to represent the MRI and CFD domain respectively.

Preparations for the Validation of the Dynamic Data Assimilation

A reference numerical solution was manufactured in $\mathbf{M_7}$ (as described in 4.4.1) with periodic flow rates based on the two-peaks sinusoidal function h(t) (4.4.2) with a period of 0.8 s. The obtained solution was sampled at $2n+1$ equidistantly placed time instants, where $n = 12$ is the number of harmonics, which was chosen according to the findings of the chapter 4. The first sample is the reference flow field at time $\frac{0.8}{2n+1} = 0.032$ s, whereas the last sample is the reference flow field at time 0.8 s.

The samples in the world domain (mesh $\mathbf{M_7}$) were all mapped into the MRI domain (mesh $\mathbf{M_2}$) using a linear interpolation. This process is illustrated in figure 5.1 by the mapping from $\mathbf{M_7}$ (on the top) into $\mathbf{M_2}$ (on the left-bottom corner). An artificial noise with an isotropic VENC of 0.75 m/s and an SNR of 10 (see section 2.4.3 for more details) was added on top of the interpolated flow fields in the MRI domain.

A noise detection algorithm, as described in section 2.3.1, was employed to detect the potential spurious vectors in the noisy flow fields. Thereafter, the samples in the MRI domain are mapped from $\mathbf{M_2}$ into the CFD domain $\mathbf{M_4}$. This is illustrated on the bottom left and right corners of figure 5.1.

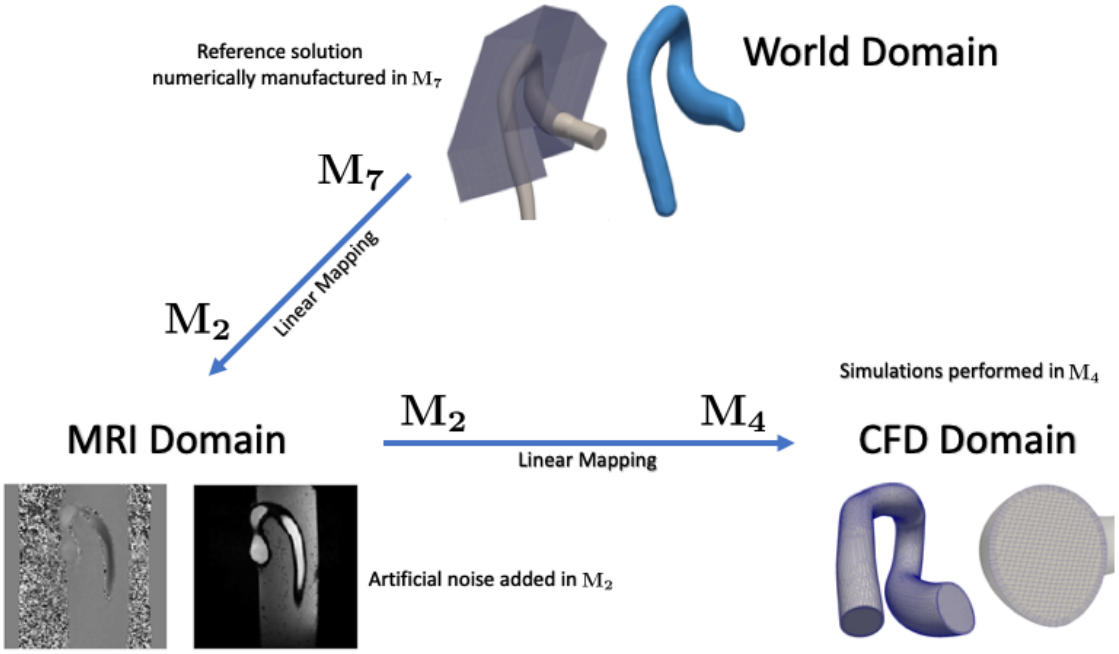

Figure 5.1: Preparations for the validation of the proposed approach, prior to performing the dynamic data assimilation.

Having mapped the flow fields into the CFD domain, the proposed approach was employed based on the artificially generated observations in $\mathbf{M_4}$ using the algorithm 3. For a proper evaluation of the proposed method, an additional reference solution was also generated in $\mathbf{M_4}$, which was used as the ground truth. The errors nRMSE^X and FDE^X were then computed between the flow fields obtained from the inverse problem and the ground truth. These steps can be summarised as follows:

- Generate the reference solution (see section 4.4.1) in the finest mesh $\mathbf{M_7}$ (world domain)
- Sample the reference solution at $2n+1$ equidistantly placed time instants
- Linearly map the sampled solution from $\mathbf{M_7}$ into the coarsest mesh $\mathbf{M_2}$ (MRI domain)
- Add some artificial noise (see section 2.4.3) to the flow fields in the MRI domain $\mathbf{M_2}$.
- Apply the noise detection scheme (see section 2.3.1) to the noisy flow fields in $\mathbf{M_2}$
- Map the denoised flow fields from $\mathbf{M_2}$ into the fine mesh $\mathbf{M_4}$ (CFD domain).
- Run the CFD simulations in $\mathbf{M_4}$ using both the HB method computing a single forward solution described in the chapter 4 and the HB method combined with the inverse problem computing an optimised solution described in the present chapter, denoting the obtained flow fields by $\boldsymbol{u}_{\mathbf{hb}}^{\mathbf{for}}$ and $\boldsymbol{u}_{\mathbf{hb}}^{\mathbf{opt}}$ respectively.

- Additionally generate a reference solution in $\mathbf{M_4}$, denoting it by $\boldsymbol{u}_{\mathbf{ext}}$
- Evaluate the errors $\text{nRMSE}^X(\boldsymbol{u}_{\mathbf{hb}}^{\mathbf{for}}, \boldsymbol{u}_{\mathbf{ext}})$ and $\text{nRMSE}^X(\boldsymbol{u}_{\mathbf{hb}}^{\mathbf{opt}}, \boldsymbol{u}_{\mathbf{ext}})$ (see equation (5.3.1))
- Evaluate the errors $\text{FDE}^X(\boldsymbol{u}_{\mathbf{hb}}^{\mathbf{for}}, \boldsymbol{u}_{\mathbf{ext}})$ and $\text{FDE}^X(\boldsymbol{u}_{\mathbf{hb}}^{\mathbf{opt}}, \boldsymbol{u}_{\mathbf{ext}})$ (see equation (5.3.2))

Numerical Results

In what follows, the noisy observations available in $\mathbf{M_4}$ will be represented by $\boldsymbol{u}_{\mathbf{snr}}$ in Ω. For the dynamic data assimilation procedure, algorithm 3 was executed with the input parameters $(\boldsymbol{u}_{\mathbf{snr}}, \boldsymbol{g}_{\mathbf{snr}}, \boldsymbol{u}_{\mathbf{snr}}, 25)$, where $\boldsymbol{g}_{\mathbf{snr}} = \boldsymbol{u}_{\mathbf{snr}}$ on Γ_i. Thus, the initial guesses were $\boldsymbol{u}_{\mathbf{snr}}$ and $\boldsymbol{g}_{\mathbf{snr}}$, whereas the target flow field for the flow-matching term in the objection function (5.2.7) was set to the same flow field $\boldsymbol{u}_{\mathbf{snr}}$ (this corresponds to the application of MRI data as the observations for the flow-matching and as the initial guesses). The flow field obtained from the dynamic data assimilation process will be denoted by $\boldsymbol{u}_{\mathbf{hb}}^{\mathbf{opt}}$. The flow matching was performed in Ω_s with $s = 2$. That is, the flow-matching domain Ω_s is a contracted domain of Ω such that the distance to Γ_w is at least 2 mm. Motivated by the findings of chapter 2 in table 2.1, optimisation parameters β and β_1 were set to 10^{-5} and 10^{-8} respectively. Parameter α was set to 1. Furthermore, using the same data,$\boldsymbol{u}_{\mathbf{snr}}$, the HB method was also employed as a single forward simulation without adopting the assimilation process (and the obtained flow field is denoted by $\boldsymbol{u}_{\mathbf{hb}}^{\mathbf{for}}$).

For the evaluation of the errors nRMSE^X and FDE^X (equations (5.3.1) and (5.3.2)), the domain $X = E_2^4$ (as described in (2.5.1)) will be considered in what follows. Thus, $\text{nRMSE}^{E_2^4}$ and $\text{FDE}^{E_2^4}$ evaluate the normalised root-mean square error and the flow direction error in the domain E_2^4, which corresponds to the domain in near-wall regions (within a distance of 2 mm from the wall boundary) at the aortic root in the close proximity of the inlet (within a distance of 4 cm from the inlet boundary). This choice of the error evaluation in the domain E_2^4 is motivated by the fact that, the aortic root is a clinically relevant place, where the arterial walls are prone to pathological modification. This is due to the flow disturbances in the close proximity of the inlet. In addition, the errors were also evaluated in the whole domain Ω. Under these conditions, the numerical results are summarised in table 5.1.

It can be observed that, compared with the results obtained from the HB method as a forward simulation only, there is a significant improvement in the outcome provided by the assimilation (against the noisy solution) in the close proximity of the inlet. This is a remarkable finding for the improvement of the flow field, especially at the aortic root.

5.3.2 Dynamic Data Assimilation in Different Mesh Resolutions

For the purpose of further validation of the proposed approach, different mesh geometries are considered for the assimilation procedure. In addition to the assimilation in mesh $\mathbf{M_4}$ presented as the CFD domain in the previous section, the other two meshes $\mathbf{M_2}$ and $\mathbf{M_7}$ are

$(\boldsymbol{x}, \boldsymbol{y})$	$\text{nRMSE}^{E_2^4}(\boldsymbol{x}, \boldsymbol{y})$	$\text{FDE}^{E_2^4}(\boldsymbol{x}, \boldsymbol{y})$	$\text{nRMSE}^{\Omega}(\boldsymbol{x}, \boldsymbol{y})$	$\text{FDE}^{\Omega}(\boldsymbol{x}, \boldsymbol{y})$
$(\boldsymbol{u}_{\mathbf{snr}}, \boldsymbol{u}_{\mathbf{ext}})$	16.76%	0.367	6.90%	0.166
$(\boldsymbol{u}_{\mathbf{hb}}^{\mathbf{for}}, \boldsymbol{u}_{\mathbf{ext}})$	3.75%	0.095	1.66%	0.042
$(\boldsymbol{u}_{\mathbf{hb}}^{\mathbf{opt}}, \boldsymbol{u}_{\mathbf{ext}})$	2.39%	0.055	1.59%	0.027

Table 5.1: Root mean square errors and flow direction errors evaluated in the domains E_2^4 and Ω. The errors are evaluated against the ground truth $\boldsymbol{u}_{\mathbf{ext}}$ for the noisy flow field $\boldsymbol{u}_{\mathbf{snr}}$ and the flow fields $\boldsymbol{u}_{\mathbf{hb}}^{\mathbf{for}}$ and $\boldsymbol{u}_{\mathbf{hb}}^{\mathbf{opt}}$, obtained from the harmonic balance and the dynamic data assimilation methods respectively.

also considered for performing the assimilation in the present section. Since the observations with the artificial noise were already available in $\mathbf{M_2}$, there is no need for additional mappings of the flow fields and the assimilation can be performed based on the available observations in $\mathbf{M_2}$. However, since a ground truth was missing in $\mathbf{M_2}$, and additional reference solution is manufactured for the purpose of error evaluations using a ground truth in $\mathbf{M_2}$. In addition, the noisy observations are mapped from $\mathbf{M_2}$ into $\mathbf{M_7}$, where a ground truth was already available as described in the previous section. The assimilation is then performed also in $\mathbf{M_7}$, the finest mesh available. The numerical results using mesh geometries with different numbers of cells are summarised in table 5.2.

	$(\boldsymbol{x}, \boldsymbol{y})$	$\text{nRMSE}^{E_2^4}(\boldsymbol{x}, \boldsymbol{y})$	$\text{FDE}^{E_2^4}(\boldsymbol{x}, \boldsymbol{y})$	$\text{nRMSE}^{\Omega}(\boldsymbol{x}, \boldsymbol{y})$	$\text{FDE}^{\Omega}(\boldsymbol{x}, \boldsymbol{y})$
$\mathbf{M_2}$	$(\boldsymbol{u}_{\mathbf{snr}}, \boldsymbol{u}_{\mathbf{ext}})$	26.47%	0.488	10.40%	0.228
	$(\boldsymbol{u}_{\mathbf{hb}}^{\mathbf{for}}, \boldsymbol{u}_{\mathbf{ext}})$	8.15%	0.141	6.93%	0.157
	$(\boldsymbol{u}_{\mathbf{hb}}^{\mathbf{opt}}, \boldsymbol{u}_{\mathbf{ext}})$	3.50%	0.068	1.97%	0.035
$\mathbf{M_4}$	$(\boldsymbol{u}_{\mathbf{snr}}, \boldsymbol{u}_{\mathbf{ext}})$	16.76%	0.367	6.90%	0.166
	$(\boldsymbol{u}_{\mathbf{hb}}^{\mathbf{for}}, \boldsymbol{u}_{\mathbf{ext}})$	3.75%	0.095	1.66%	0.042
	$(\boldsymbol{u}_{\mathbf{hb}}^{\mathbf{opt}}, \boldsymbol{u}_{\mathbf{ext}})$	2.39%	0.055	1.59%	0.027
$\mathbf{M_7}$	$(\boldsymbol{u}_{\mathbf{snr}}, \boldsymbol{u}_{\mathbf{ext}})$	17.67%	0.381	7.40%	0.174
	$(\boldsymbol{u}_{\mathbf{hb}}^{\mathbf{for}}, \boldsymbol{u}_{\mathbf{ext}})$	3.87%	0.096	1.74%	0.044
	$(\boldsymbol{u}_{\mathbf{hb}}^{\mathbf{opt}}, \boldsymbol{u}_{\mathbf{ext}})$	2.49%	0.061	1.42%	0.027

Table 5.2: Root mean square errors and flow direction errors evaluated in the domains E_2^4 and Ω for the flow fields in computational mesh geometries $\mathbf{M_2}$, $\mathbf{M_4}$ and $\mathbf{M_7}$. The errors are evaluated against the ground truth $\boldsymbol{u}_{\mathbf{ext}}$ for the noisy flow field $\boldsymbol{u}_{\mathbf{snr}}$ and the flow fields $\boldsymbol{u}_{\mathbf{hb}}^{\mathbf{for}}$ and $\boldsymbol{u}_{\mathbf{hb}}^{\mathbf{opt}}$, obtained from the harmonic balance and the dynamic data assimilation methods respectively.

The feasibility and accuracy of the proposed dynamic data assimilation method combined with the harmonic balance approach was shown using different mesh geometries. It was observed that the assimilation procedure is unbiased against meshes with different number of cells, most importantly also in the close proximity of the inlet.

5.3.3 Dynamic Data Assimilation using 4D flow MRI Acquisition

For the optimal control problem, the proposed approach was tested in a realistic scenario using flow data gathered from 4D flow MRI scans. The same flow data presented in section 4.2.1 were used, and hence, the details of the experimental set-up and the description of the applied preprocessing steps are skipped in the present section.

Simulations were performed with both methods, HB as a forward simulation only and HB combined with data assimilation, and compared with the MRI data or with each other. Flow patterns obtained from both methods were first compared with the MRI data by visual inspection. Figure 5.2 shows two slices illustrating the magnitude of the velocities inside of the domain Ω, obtained from the noisy MRI measurements, denoted as $\boldsymbol{u}_{\mathbf{snr}}$ (in the middle of the figure), and from the computations using the data assimilation, denoted as $\boldsymbol{u}_{\mathbf{hb}}^{\mathbf{opt}}$ (on the left side), and using the HB method as a forward simulation, denoted as $\boldsymbol{u}_{\mathbf{hb}}^{\mathbf{for}}$ (on the right side) respectively. The presented slices correspond to the time instant at peak systole, where the velocities reach their highest magnitudes. One slice was placed at the aortic root and was oriented such that the velocity profiles in the close proximity of the inlet are clearly visible. Another slice was placed at the aortic arch to additionally illustrate the obtained flow patterns at a moderate distance from the inlet.

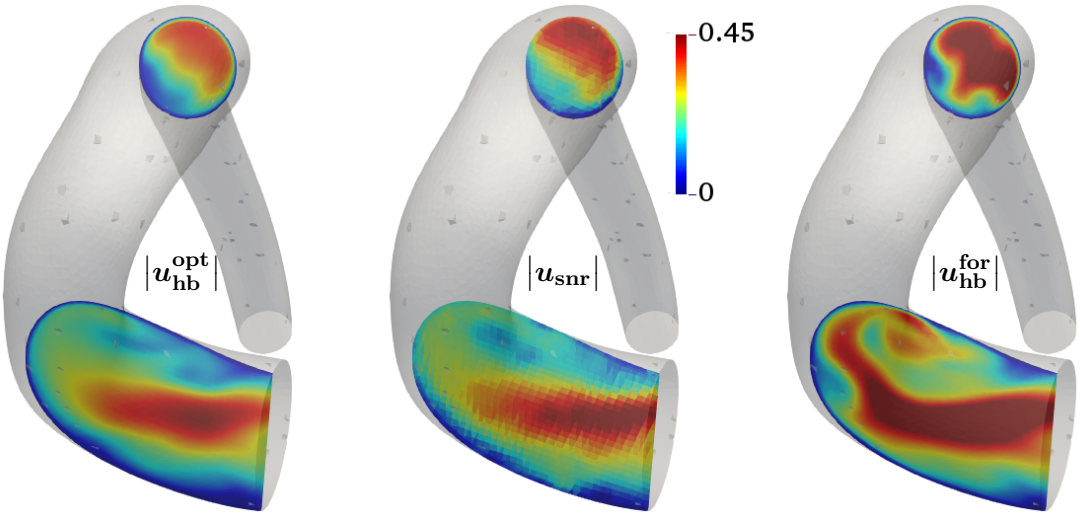

Figure 5.2: Slices for the magnitudes of different velocity fields at the aortic root and arch.

Furthermore, figure 5.3 illustrates the streamlines of the flow fields in the whole domain. Both the slices and the streamlines obviously show that the noise-free flow field obtained from the assimilation process is fairly close to the noisy flow field measured with 4D flow MRI, whereas the flow field obtained from a conventional forward simulation, without the optimisation of the velocities, is largely different compared to the measurements.

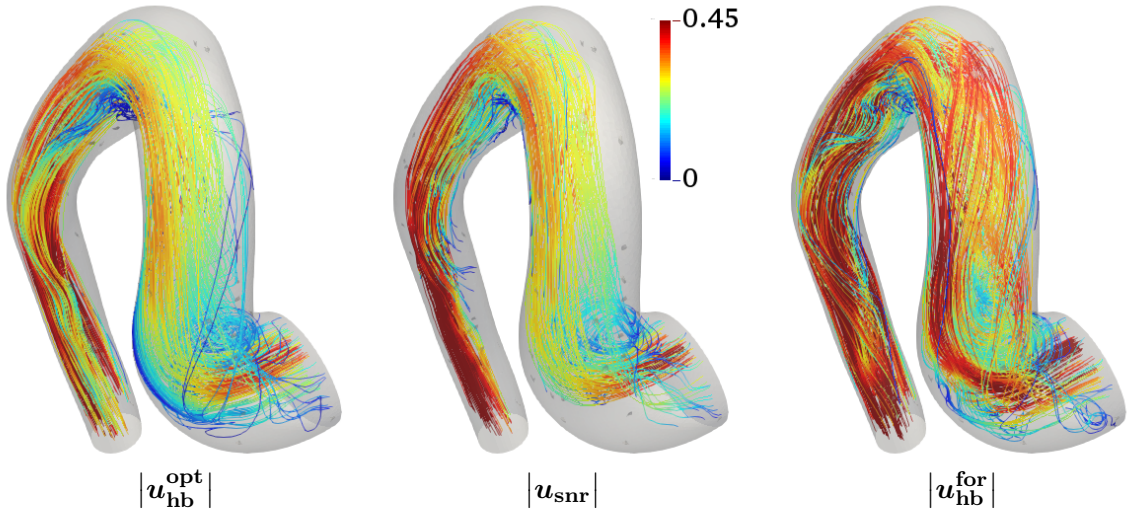

Figure 5.3: Streamlines for the magnitudes of different velocity fields.

Since there is no ground truth available in this case, the flow fields obtained from both methods were quantitatively compared with each other to demonstrate the extent of their difference from each other. In the whole domain, Ω, evaluation of the errors yielded $\mathrm{nRMSE}^{\Omega}(\boldsymbol{u}_{\mathbf{hb}}^{\mathbf{for}}, \boldsymbol{u}_{\mathbf{hb}}^{\mathbf{opt}}) = 21.66\%$ and $\mathrm{FDE}^{\Omega}(\boldsymbol{u}_{\mathbf{hb}}^{\mathbf{for}}, \boldsymbol{u}_{\mathbf{hb}}^{\mathbf{opt}}) = 0.229$, whereas in the close proximity of the inlet, the errors were $\mathrm{nRMSE}^{E_2^4}(\boldsymbol{u}_{\mathbf{hb}}^{\mathbf{for}}, \boldsymbol{u}_{\mathbf{hb}}^{\mathbf{opt}}) = 30.08\%$ and $\mathrm{FDE}^{E_2^4}(\boldsymbol{u}_{\mathbf{hb}}^{\mathbf{for}}, \boldsymbol{u}_{\mathbf{hb}}^{\mathbf{opt}}) = 0.314$.

Notably, the better qualitative agreement between the observations and the optimised solution, and quantitatively significant differences between the optimised solution and the predictions from conventional forwards CFD simulation, support the fact that the optimisation delivers a better solution when compared with the conventional CFD approach.

5.4 Conclusion

In this work, a novel approach was developed for dynamic data assimilation, interlacing computational fluid dynamics with phase-contrast magnetic resonance imaging. The proposed approach follows a temporally-discretise-then-optimise-then-spatially-discretise strategy, whereas a Fourier-spectral method was employed for the temporal discretisation, which was then integrated in an inverse problem.

The methodology was validated against a manufactured numerical solution as well as against experimental 4D flow MRI measurements performed in a glass replica of a human aorta. The

proposed algorithm was examined in detail to estimate the efficiency of the methodology for reconstructing the blood flow at the aortic root and in near-wall regions.

The new method proved to deliver physically consistent flow fields, with substantial reduction of noise present in the 4D flow MRI measurements, outperforming the predictive capabilities of conventional CFD approaches. The novel approach provides a systematic strategy to improve the model predictions regarding clinically relevant hemodynamic data, such as the wall shear stresses.

The proposed approach considerably improves the flow field at the aortic root, which is one of the most important clinically relevant locations for the development of pathological alterations of the anatomical structures underlying the arterial wall. Hence, the new method reveals a great potential for predicting clinically relevant hemodynamic phenomenology.

6 Summary of Findings

In this work, a new and efficient method has been introduced to perform transient data assimilation in computational hemodynamics. The proposed approach (also named as the Fourier-spectral dynamic data assimilation), relies on harmonically balanced equations expressed in the frequency domain, which are incorporated into the assimilation process. The frequency domain equations result in a time discretisation, which differentiates the proposed approach from conventional methods based on traditional time-stepping schemes. Concerning the assimilation process, the variational approach has been followed to compute the gradient of an objective function (with respect to control) based on the harmonically balanced adjoint equations expressed in the frequency domain.

The methodology has been validated against numerically generated solutions (which serve as a reference flow) and against experimental 4D flow MRI measurements performed in a glass replica of a human aorta. The proposed algorithms have been examined in detail to estimate the efficiency of the methodology for reconstructing the blood flow at the aortic root and in near-wall regions. The new method has proven to deliver physically consistent flow fields, with substantial reduction of noise present in the 4D flow MRI measurements, outperforming the predictive capabilities of conventional CFD approaches. The novel approach provides a systematic strategy to improve the model predictions regarding clinically relevant hemodynamic data, such as the wall shear stresses.

In order to achieve a full control over the flow being reconstructed using the new approach, a few simplification assumptions have been made. First of all, the flow has been considered to be Newtonian. Secondly, in the experimental setup, the physical phantom (made from glass) was rigid and hence there has been no wall motion to be considered. Performing fluid-structure interaction studies based on the proposed approach would be very appealing as a matter of future research. Another limitation of the experimental setup is the lack of additional branches at the aortic arch. However, for studies with the aim to evaluate the WSSs at the aortic root, it needs investigation whether or not the integration of the locations around the aortic arch is required in the assimilation process. In the presented experiments, the centrifugal pump in the control room had to be connected with the physical phantom in the scanner room using long pipes. This resulted in the fact, that the backflow effect (which can be generated by the pump) could not be observed (due to long pipes) in the physical phantom. Finally, owing to these capabilities and limitations of the experimental setup, the inflow considered at the inlet did not contain the backflow of the R-wave.

Based on the presented results, it can be concluded that the harmonic balance numerical scheme reveals itself as a method with a tremendous potential in computational hemodynamics. The proposed approach enables pulsatile fluid flow simulations at a significantly smaller cost when compared with traditional methods, without exhibiting deterioration of the approximate solution. The method shows a significant improvement regarding the trade-off between computational cost and accuracy for applications in computational hemodynamics. Based on the present experiments, the harmonic balance method was about 15 times faster compared to the conventional transient simulations.

The experience dictates that only a moderate number of harmonics is required to accurately resolve the periodic fluid flow problem. Regarding the number of time instants at which (4D flow MRI) data is acquired per cardiac cycle, the method can be easily adjusted such that the discretised momentum equations are temporally registered with the measurements. In case of 4D flow MRI, the experience indicates that it requires observational data at a number of time instants between 17 and 25. This corresponds to a number of harmonics of at least 8, which is a region in which the method has proved to be satisfactorily accurate.

In addition, the harmonic balance approach has been efficiently incorporated into a variational adjoint-based optimal flow control. For large, convection dominated problems, Fourier-spectral dynamic data assimilation (the new method) performs within very affordable and feasible wall clock times, which are otherwise nearly impossible or quite difficult to be achieved using the conventional methods.

The work considerably improves the flow field at the aortic root, which is one of the most important clinically relevant locations for the development of pathological alterations of the anatomical structures underlying the arterial wall. Hence, the new method reveals a great potential for predicting clinically relevant hemodynamic phenomenology.

References

[Aup17] G. Aupy and J. Herrmann. 'Periodicity in optimal hierarchical checkpointing schemes for adjoint computations'. In: *Optim. Methods Softw.* 32.3 (2017), pp. 594–624. (Cited on p. 69)
DOI: 10.1080/10556788.2016.1230612

[Bac05] F. Bachinger, U. Langer and J. Schöberl. 'Numerical analysis of nonlinear multiharmonic eddy current problems'. In: *Numer. Math.* 100.4 (2005), pp. 593–616. (Cited on p. 55)
DOI: 10.1007/s00211-005-0597-2

[Bel14] T. Bellsky, E. J. Kostelich and A. Mahalov. 'Kalman filter data assimilation: Targeting observations and parameter estimation'. In: *Chaos: An Interdisciplinary Journal of Nonlinear Science* 24.2 (2014), p. 024406. (Cited on p. 8)
DOI: 10.1063/1.4871916

[Ber14] L. Bertagna, M. D'Elia, M. Perego and A. Veneziani. 'Data Assimilation in Cardiovascular Fluid–Structure Interaction Problems: An Introduction'. In: *Fluid-Structure Interaction and Biomedical Applications*. Ed. by Tomáš Bodnár, Giovanni P. Galdi and Šárka Nečasová. Springer Basel, 2014, pp. 395–481. (Cited on p. 25)
DOI: 10.1007/978-3-0348-0822-4_6

[Bha13] H. Bhatia, G. Norgard, V. Pascucci and P. -T. Bremer. 'The Helmholtz-Hodge Decomposition – A Survey'. In: *IEEE Trans. Vis. Comput. Graph.* 19.8 (2013), pp. 1386–1404. (Cited on p. 20)
DOI: 10.1109/TVCG.2012.316

[Boc11] J. Bock, A. Frydrychowicz, R. Lorenz, D. Hirtler, A. J. Barker, K. M. Johnson, R. Arnold, H. Burkhardt, J. Hennig and M. Markl. 'In vivo noninvasive 4D pressure difference mapping in the human aorta: phantom comparison and application in healthy volunteers and patients'. In: *Magn. Reson. Med.* 66.4 (2011), pp. 1079–1088. (Cited on p. 34)
DOI: 10.1002/mrm.22907

[Bou18] P. Bouillot, B. M. Delattre, O. Brina, R. Ouared, M. Farhat, C. Chnafa, D. A. Steinman, V. M. Pereira K. O. Lovblad and M. I. Vargas. '3D phase contrast MRI: Partial volume correction for robust blood flow quantification in small intracranial vessels'. In: *Magn. Reson. Med.* 79.1 (2018), pp. 129–140. (Cited on p. 3)
DOI: 10.1002/mrm.26637

[Boy01] J. P. Boyd. *Chebyshev and Fourier Spectral Methods: Second Revised Edition*. Dover Books on Mathematics. Dover Publications, 2001. ISBN: 9780486411835. (Cited on p. 44)
URL: https://books.google.ch/books?id=i9UoAwAAQBAJ

[Bre06] D. M. Bressoud. *A Radical Approach to Real Analysis: Second Edition (Classroom Resource Material)*. The Mathematical Association of Americaa, 2006. ISBN: 0883857472. (Cited on p. 45)

[Bré18] F. Bréhard, N. Brisebarre and M. Joldes. 'Validated and numerically efficient Chebyshev spectral methods for linear ordinary differential equations'. In: *ACM Trans. Math. Softw.* 44.4 (2018), pp. 1–42. (Cited on p. 44)
DOI: 10.1145/3208103

[Bue14] A. Bueno-Orovio, D. Kay and K. Burrage. 'Fourier spectral methods for fractional-in-space reaction-diffusion equations'. In: *BIT Num. Math.* 54.4 (2014), pp. 937–954. (Cited on p. 44)
DOI: 10.1007/s10543-014-0484-2

[Cal16a] F. M. Callaghan and S. M. Grieve. 'Spatial resolution and velocity field improvement of 4D-flow MRI'. In: *Magn. Reson. Med.* 78.5 (2016), pp. 1959–1968. (Cited on p. 34)
DOI: 10.1002/mrm.26557

[Cal16b] F. M. Callaghan, R. Kozor, A. G. Sherrah, M. Vallely, D. Celermajer, G. A. Figtree and S. M. Grieve. 'Use of multi-velocity encoding 4D flow MRI to improve quantification of flow patterns in the aorta'. In: *J. Magn. Reson. Imaging* 43.2 (2016), pp. 352–363. (Cited on p. 34)
DOI: 10.1002/jmri.24991

[Cam12] I. C. Campbell, J. Ries, S. S. Dhawan, A. A. Quyyumi, W. R. Taylor and J. N. Oshinski. 'Effect of inlet velocity profiles on patient-specific computational fluid dynamics simulations of the carotid bifurcation'. In: *J. Biomech. Eng.* 134.5 (2012), p. 051001. (Cited on p. 4)
DOI: 10.1115/1.4006681

[Can06] C. Canuto, M. Y. Hussaini, A. Quarteroni and T. A. Zang. *Spectral Methods – Fundamentals in Single Domains*. Springer, Berlin, Heidelberg, 2006. (Cited on p. 45)
DOI: 10.1007/978-3-540-30726-6

[Can07] C. Canuto, M. Y. Hussaini, A. Quarteroni and T. A. Zang. *Spectral Methods – Evolution to Complex Geometries and Applications to Fluid Dynamics*. Springer, Berlin, Heidelberg, 2007. (Cited on p. 44)
DOI: 10.1007/978-3-540-30728-0

[Can15] P. Cannarsa and T. D'Aprile. *Introduction to Measure Theory and Functional Analysis*. Springer International Publishing, 2015. ISBN: 9783319170183. (Cited on p. 43)

[Can88] C. Canuto, M. Y. Hussaini, A. Quarteroni and T. A. Zang. *Spectral Methods in Fluid Dynamics*. Springer, Berlin, Heidelberg, 1988. (Cited on pp. 43, 44, 58)
DOI: 10.1007/978-3-642-84108-8

[Cao02] Y. Cao, S. Li and L. Petzold. 'Adjoint sensitivity analysis for differential-algebraic equations: algorithms and software'. In: *J. Comput. Appl. Math.* 149.1 (2002), pp. 171–191. ISSN: 0377-0427. (Cited on p. 69)
DOI: 10.1016/S0377-0427(02)00528-9

[Cha01] I. Charpentier. 'Checkpointing Schemes for Adjoint Codes: Application to the Meteorological Model Meso-NH'. In: *SIAM J. Sci. Comput.* 22.6 (2001), pp. 2135–2151. (Cited on p. 69)
DOI: 10.1137/S1064827598343735

[Cha07] Y. S. Chatzizisis, A. Ü. Coskun, M. Jonas, E. R. Edelman, C. L. Feldman and P. H. Stone. 'Role of endothelial shear stress in the natural history of coronary atherosclerosis and vascular remodeling: molecular, cellular, and vascular behavior'. In: *Journal of the American College of Cardiology* 49.25 (2007), pp. 2379–2393. (Cited on p. 2)
DOI: 10.1016/j.jacc.2007.02.059

[Cha13] D. Chapelle, M. Fragu, V. Mallet and P. Moireau. 'Fundamental principles of data assimilation underlying the Verdandi library: applications to biophysical model personalization within euHeart'. In: *Med. Biol. Eng. Comput.* 51.11 (2013), pp. 1221–1233. (Cited on p. 8)
DOI: 10.1007/s11517-012-0969-6

[Che98] L. Q. Chen and J. Shen. 'Applications of semi-implicit Fourier-spectral method to phase field equations'. In: *Comput. Phys. Commun.* 108.2 (1998), pp. 147–158. (Cited on p. 44)
DOI: 10.1016/S0010-4655(97)00115-X

[Chi11] J-J. Chiu and S. Chien. 'Effects of Disturbed Flow on Vascular Endothelium: Pathophysiological Basis and Clinical Perspectives'. In: *Physiol Rev.* 91.1 (2011), pp. 327–387. (Cited on p. 2)
DOI: 10.1152/physrev.00047.2009

[Cib15] M. Cibis, K. Jarvis, M. Markl, M. Rose, C. Rigsby, A. J. Barker and J. J. Wentzela. 'The effect of resolution on viscous dissipation measured with 4D flow MRI in patients with Fontan circulation: Evaluation using computational fluid dynamics'. In: *J. Biomech.* 48.12 (2015), pp. 2984–2989. (Cited on p. 34)
DOI: 10.1016/j.jbiomech.2015.07.039

[Cin15] N. Cindea, A. Imperiale and P. Moireau. 'Data assimilation of time under-sampled measurements using observers, the wave-like equation example'. In: *ESAIM Contr. Optim. CA.* (2015), p. 35. (Cited on p. 8)
DOI: 10.1051/cocv/2014042

[Cit14] S. Cito, J. Pallarés and A. Vernet. 'Sensitivity Analysis of the Boundary Conditions in Simulations of the Flow in an Aortic Coarctation under Rest and Stress Conditions'. In: *Statistical Atlases and Computational Models of the Heart. Imaging and Modelling Challenges: STACOM 2013. Lecture Notes in Computer Science*. Ed. by O. Camara, T. Mansi, M. Pop, K. Rhode, M. Sermesant and A. Young. Vol. 8330. Springer Berlin Heidelberg, 2014, pp. 74–82. (Cited on p. 4)
DOI: 10.1007/978-3-642-54268-8_9

[Coe05] R. V. Coetzee. 'Volume weighted interpolation for unstructured meshes in the finite volume method'. PhD thesis. North-West University, 2005. (Cited on p. 66)

[Col02] S. S. Collis and M. Heinkenschloss. *Analysis of the Streamline Upwind/Petrov Galerkin Method Applied to the Solution of Optimal Control Problems*. Tech. rep. TR02–01. Rice University, Houston, TX 77005–1892: Department of Computational and Applied Mathematics, 2002. (Cited on p. 8)

[Col18] G. J. Collier, M. Kim, Y. Chung and J. M. Wild. '3D phase contrast MRI in models of human airways: Validation of computational fluid dynamics simulations of steady inspiratory flow'. In: *J. Magn. Reson. Imaging* 48.5 (2018), pp. 1400–1409. (Cited on p. 50)
DOI: 10.1002/jmri.26039

[Cou91] National Research Council. *Four-Dimensional Model Assimilation of Data: A Strategy for the Earth System Sciences*. The National Academies Press, 1991. (Cited on p. 4)
DOI: 10.17226/1830

[Cra56] S. H. Crandall. *Engineering Analysis: A Survey of Numerical Procedures*. Engineering societies monographs. McGraw-Hill, 1956. (Cited on p. 43)

[Cvi16] G. Cvijetić, H. Jasak and V. Vukčević. 'Finite Volume Implementation of the Harmonic Balance Method for Periodic Non-Linear Flows'. In: *4th AIAA Aerospace Sciences Meeting* (2016). (Cited on p. 55)
DOI: 10.2514/6.2016-0070

[DEl10a] M. D'Elia and A. Veneziani. 'A data assimilation technique for including noisy measurements of the velocity field into Navier-Stokes simulations'. In: *Proc. of V European Conference on Computational Fluid Dynamics*. Ed. by J. C. F. Pereira and A. Sequeira. 1. ECCOMAS CFD, 2010. (Cited on p. 7)

[DEl10b] M. D'Elia and A. Veneziani. 'Methods for assimilating blood velocity measures in hemodynamics simulations: Preliminary results'. In: *Procedia. Comput. Sci.* 1.1 (2010), pp. 1231–1239. (Cited on pp. 7, 8)
DOI: 10.1016/j.procs.2010.04.137

[DEl12a] M. D'Elia, L. Mirabella, T. Passerini, M. Perego, M. Piccinelli, C. Vergara and A. Veneziani. 'Applications of variational data assimilation in computational hemodynamics'. In: *Modeling of Physiological Flows*. Ed. by D. Ambrosi, A. Quarteroni and G. Rozza. Vol. 5. Springer Milan, 2012, pp. 363–394. (Cited on pp. 8, 25)
DOI: 10.1007/978-88-470-1935-5_12

[DEl12b] M. D'Elia, M. Perego and A. Veneziani. 'A Variational Data Assimilation Procedure for the Incompressible Navier-Stokes Equations in Hemodynamics'. In: *J. Sci. Comput.* 52.2 (2012), pp. 340–359. (Cited on p. 8)
DOI: 10.1007/s10915-011-9547-6

[Den03] F. M. Denaro. 'On the application of the Helmholtz-Hodge decomposition in projection methods for incompressible flows with general boundary conditions'. In: *Int. J. Numer. Meth. Fluids* 3 (2003), pp. 43–69. (Cited on p. 20)
DOI: 10.1002/fld.598

[Fin13] B. A. Finlayson. *The Method of Weighted Residuals and Variational Principles*. Society for Industrial and Applied Mathematics, 2013. (Cited on p. 44)
DOI: 10.1137/1.9781611973242

[Fin66] B. A. Finlayson and L.E. Scriven. 'The method of weighted residuals - A review'. In: *Appl. Mech. Rev.* 19.9 (1966), pp. 735–748. (Cited on pp. 43, 44)

[Fin72] B. A. Finlayson. *The Method of Weighted Residuals and Variational Principles: With Application in Fluid Mechanics, Heat and Mass Transfer*. Educational Psychology. Academic Press, 1972. ISBN: 9780122570506. (Cited on p. 44)

[For08] L. Formaggia, A. Veneziani and C. Vergara. 'A New Approach to Numerical Solution of Defective Boundary Value Problems in Incompressible Fluid Dynamics'. In: *SIAM J. Numer. Anal.* 46.6 (2008), pp. 2769–2794. (Cited on p. 7)
DOI: 10.1137/060672005

[For10] L. Formaggia, A. Veneziani and C. Vergara. 'Flow rate boundary problems for an incompressible fluid in deformable domains: Formulations and solution methods'. In: *Comput. Methods Appl. Mech. Engrg.* 199.9–12 (2010), pp. 677–688. (Cited on p. 7)
DOI: 10.1016/j.cma.2009.10.017

[Fri10] K. Friston, K. Stephan, B. Li and J. Daunizeau. 'Generalised Filtering'. In: *Math. Probl. Eng.* 2010.1 (2010), p. 34. (Cited on p. 8)
DOI: 10.1155/2010/621670

[Fun19] S. W. Funke, M. Nordaas, Ø. Evju, M. S. Alnæs and K. A. Mardal. 'Variational data assimilation for transient blood flow simulations: Cerebral aneurysms as an illustrative example'. In: *Int. J. Numer. Method. Biomed. Eng.* 35.1 (2019), e3152. (Cited on p. 70)
DOI: 10.1002/cnm.3152

[Fur98] A. V. Fursikov, M. D. Gunzburger and L. S. Hou. 'Boundary Value Problems and Optimal Boundary Control for the Navier–Stokes System: the Two-Dimensional Case'. In: *SIAM J. Control Optim.* 36.3 (1998), pp. 852–894. (Cited on p. 25)
DOI: 10.1137/S0363012994273374

[Gar11] D. Garcia. 'A fast all-in-one method for automated post-processing of PIV data'. In: *Exp. Fluids* 50.5 (2011), pp. 1247–1259. (Cited on p. 18)
DOI: 10.1007/s00348-010-0985-y

[Gar13] J. D. García-Saldaña and A. Gasull. 'A theoretical basis for the Harmonic Balance method'. In: *J. Differ. Equ.* 254.1 (2013), pp. 67–80. (Cited on p. 55)
DOI: 10.1016/j.jde.2012.09.011

[Ges73] F. B. Gessner. 'Brief reviews: Hemodynamic theories of atherogenesis'. In: *Circulation Research* 33.3 (1973), pp. 259–266. (Cited on p. 2)
DOI: 10.1161/01.RES.33.3.259

[Gha16] H. Gharahi, B. A. Zambrano, D. C. Zhu, J. K. DeMarco and S. Baek. 'Computational fluid dynamic simulation of human carotid artery bifurcation based on anatomy and volumetric blood flow rate measured with magnetic resonance imaging'. In: *Int. J. Adv. Eng. Sci. Appl. Math.* 8.1 (2016), pp. 40–60. (Cited on p. 50)
DOI: 10.1007/s12572-016-0161-6

[Gom16] H. Gomez and L. De Lorenzis. 'The variational collocation method'. In: *Comput. Methods Appl. Mech. Eng.* 309.1 (2016), pp. 152–181. (Cited on p. 45)
DOI: 10.1016/j.cma.2016.06.00

[Gri00] A. Griewank and A. Walther. 'Algorithm 799: Revolve: An Implementation of Checkpointing for the Reverse or Adjoint Mode of Computational Differentiation'. In: *ACM Trans. Math. Softw.* 26.1 (2000), pp. 19–45. (Cited on p. 69)
DOI: 10.1145/347837.347846

[Gud95] H. Gudbjartsson and S. Patz. 'The Rician Distribution of Noisy MRI Data'. In: *Magn. Reson. Med.* 34.6 (1995), pp. 910–914. (Cited on p. 22)
DOI: 10.1002/mrm.1910340618

[Gue14] T. Guerra, J. Tiago and A. Sequeira. 'Optimal control in blood flow simulations'. In: *Int. J. Nonlin. Mech.* 64 (2014), pp. 57–69. (Cited on pp. 8, 25)
DOI: 10.1016/j.ijnonlinmec.2014.04.005

[Gue15] T. Guerra, A. Sequeira and J. Tiago. 'Existence of optimal boundary control for the Navier–Stokes equations with mixed boundary conditions'. In: *Port. Math.* 72.1 (2015), pp. 267–283. (Cited on pp. 11, 14, 25, 71)
DOI: 10.4171/PM/1968

[Gun00] M. D. Gunzburger and S. Manservisi. 'The Velocity Tracking Problem for Navier–Stokes Flows With Boundary Control'. In: *SIAM J. Control Optim.* 39.2 (2000), pp. 594–634. (Cited on p. 11)
DOI: 10.1137/S0363012999353771

[Gun02] M. D. Gunzburger. *Perspectives in Flow Control and Optimization*. Society for Industrial and Applied Mathematics, 2002. (Cited on p. 8)
DOI: 10.1137/1.9780898718720

[Hal02] K. C. Hall, P. T. Jeffrey and W. S. Clark. 'Computation of Unsteady Nonlinear Flows in Cascades Using a Harmonic Balance Technique'. In: *AIAA Journal* 40.5 (2002), pp. 879–886. (Cited on pp. 55, 58)
DOI: 10.2514/2.1754

[Hal13] K. C. Hall, K. Ekici, P. T. Jeffrey and H. D. Earl. 'Harmonic balance methods applied to computational fluid dynamics problems'. In: *Int. J. Comput. Fluid Dynam.* 27.2 (2013), pp. 52–67. (Cited on pp. 55, 58)
DOI: 10.1080/10618562.2012.742512

[Har12] S. K. Harouna and V. Perrier. 'Helmholtz-Hodge decomposition on $[0,1]^d$ by divergence-free and curl-free wavelets'. In: *Curves and Surfaces: 7th International Conference, Avignon, France, June 24 - 30, 2010, Revised Selected Papers*. Ed. by J. D. Boissonnat, P. Chenin, A. Cohen, C. Gout, T. Lyche, M. -L. Mazure and L. Schumaker. Springer Berlin Heidelberg, 2012, pp. 311–329. (Cited on p. 20)
DOI: 10.1007/978-3-642-27413-8_20

[Har13] D. Hardman, S. I. Semple, J. M. Richards and P. R. Hoskins. 'Comparison of patient-specific inlet boundary conditions in the numerical modelling of blood flow in abdominal aortic aneurysm disease'. In: *Int. J. Numer. Method Biomed. Eng.* 29.2 (2013), pp. 165–178. (Cited on p. 4)
DOI: 10.1002/cnm.2535

[Hes07] J. S. Hesthaven, S. Gottlieb and D. Gottlieb. *Spectral Methods for Time-Dependent Problems*. Cambridge Monographs on Applied and Computational Mathematics. Cambridge University Press, 2007. (Cited on p. 44)
DOI: 10.1017/CBO9780511618352

[Hoc04] P. Hochareon, K. B. Manning, A. A. Fontaine, J. M. Tarbell and S. Deutsch. 'Wall shear-rate estimation within the 50cc Penn State artificial heart using particle image velocimetry'. In: *Journal of Biomechanical Engineering* 126.4 (2004), pp. 430–437. (Cited on pp. 2, 49)
DOI: 10.1115/1.1784477

[Hu12] Z. Hu, H. Liu and P. Shi. 'Concurrent bias correction in hemodynamic data assimilation'. In: *Medical Image Analysis* 16.7 (2012), pp. 1456–1464. (Cited on p. 8)
DOI: 10.1016/j.media.2012.05.006

[Ide97] K. Ide, P. Courtier, M. Ghil and A. C. Lorenc. 'Unified Notation for Data Assimilation : Operational, Sequential and Variational'. In: *J. Meteor. Soc. Japan.* 75.1B (1997), pp. 181–189. (Cited on p. 4)
DOI: 10.2151/jmsj1965.75.1B_181

[Iso10] H. Isoda, Y. Ohkura, T. Kosugi, M. Hirano, M. T. Alley, R. Bammer, N. J. Pelc, H. Namba and H. Sakahara. 'Comparison of hemodynamics of intracranial aneurysms between MR fluid dynamics using 3D cine phase-contrast MRI and MR-based computational fluid dynamics'. In: *Neuroradiology* 52.10 (2010), pp. 913–920. (Cited on p. 50)
DOI: 10.1007/s00234-009-0634-4

[Iss86] R. I. Issa. 'Solution of the Implicitly Discretised Fluid Flow Equations by Operator-splitting'. In: *J. Comput. Phys.* 62.1 (1986), pp. 40–65. (Cited on p. 60)
DOI: 10.1016/0021-9991(86)90099-9

[Jas96] H. Jasak. 'Error Analysis and Estimation for the Finite Volume Method with Applications to Fluid Flows'. PhD thesis. Imperial College, University of London, 1996. (Cited on pp. 60, 61)

[Joh13] H. J. Johnson, M. McCormick, L. Ibáñez and The Insight Software Consortium. *The ITK Software Guide*. Third. Kitware Inc. 2013. (Cited on p. 20)
URL: http://www.itk.org/ItkSoftwareGuide.pdf

[Kar14] S. Karkar, B. Cochelin and C. Vergez. 'A comparative study of the harmonic balance method and the orthogonal collocation method on stiff nonlinear systems'. In: *J. Sound Vib.* 333.12 (2014), pp. 2554–2567. (Cited on p. 55)
DOI: 10.1016/j.jsv.2014.01.019

[Kat07] D. Katritsis, L. Kaiktsis, A. Chaniotis, J. Pantos, E. P. Efstathopoulos and V. Marmarelis. 'Wall shear stress: theoretical considerations and methods of measurement'. In: *Progress in Cardiovascular Diseases* 49.5 (Mar. 2007), pp. 307–329. (Cited on pp. 2, 49)
DOI: 10.1016/j.pcad.2006.11.001

[Kol16] A. Kolipaka, V. S. P. Illapani, P. Kalra, J. Garcia, X. Mo, M. Markl and R. D. White. 'Quantification and Comparison of 4D-Flow MRI-Derived Wall Shear Stress and MRE-Derived Wall Stiffness of the Abdominal Aorta'. In: *J. Magn. Reson. Imaging* 45.3 (2016), pp. 771–778. (Cited on pp. 3, 49)
DOI: 10.1002/jmri.25445

[Kol18] T. S. Koltukluoğlu and P. J. Blanco. 'Boundary control in computational haemodynamics'. In: *J. Fluid Mech.* 847 (2018), pp. 329–364. (Cited on pp. 7, 53)
DOI: 10.1017/jfm.2018.329

[Kön03] K. Königsberger. *Analysis 1*. Springer-Lehrbuch. Springer Berlin Heidelberg, 2003. ISBN: 9783540403715. (Cited on pp. 43, 47)

[Kön06] K. Königsberger. *Analysis 2*. Springer-Lehrbuch v. 2. Physica-Verlag, 2006. ISBN: 9783540350774. (Cited on p. 43)

[Ku85] David N. Ku, Don P. Giddens, Christopher K. Zarins and Seymour Glagov. 'Pulsatile flow and atherosclerosis in the human carotid bifurcation. Positive correlation between plaque location and low oscillating shear stress'. In: *Arteriosclerosis, Thrombosis, and Vascular Biology* 5.3 (May 1985), pp. 293–302. (Cited on p. 2)
DOI: 10.1161/01.ATV.5.3.293

[Lal17] R. Lal, B. Mohammadi and F. Nicoud. 'Data assimilation for identification of cardiovascular network characteristics'. In: *Int. J. Numer. Method. Biomed. Eng.* 33.5 (2017), e2824. (Cited on p. 8)
DOI: 10.1002/cnm.2824

[Lar17] D. Larsson, J. H. Spuhler, S. Petersson, T. Nordenfur, M. Colarieti-Tosti, J. Hoffman, R. Winter and M. Larsson. 'Patient-Specific Left Ventricular Flow Simulations From Transthoracic Echocardiography: Robustness Evaluation and Validation Against Ultrasound Doppler and Magnetic Resonance Imaging'. In: *IEEE Trans. Med. Imaging* 36.11 (2017), pp. 2261–2275. (Cited on p. 34)
DOI: 10.1109/TMI.2017.2718218

[Lee11] H. Lee. 'Optimal control for quasi-Newtonian flows with defective boundary conditions'. In: *Comput. Methods Appl. Mech. Engrg.* 200.33–36 (2011), pp. 2498–2506. (Cited on p. 25)
DOI: 10.1016/j.cma.2011.04.019

[Lee90] H. Lee-Wing and A. T. Patera. 'A Legendre spectral element method for simulation of unsteady incompressible viscous free-surface flows'. In: *Comput. Methods Appl. Mech. Eng.* 80.1 (1990), pp. 355–366. (Cited on p. 44)
DOI: 10.1016/0045-7825(90)90040-S

[Mad81] Y. Maday and A. Quarteroni. 'Legendre and Chebyshev spectral approximations of Burgers' equation'. In: *Num. Math.* 37.3 (1981), pp. 321–332. (Cited on p. 44)
DOI: 10.1007/BF01400311

[Mal85] M.R Malik, T.A Zang and M.Y Hussaini. 'A spectral collocation method for the Navier-Stokes equations'. In: *J. Comput. Phys.* 61.1 (1985), pp. 64–88. (Cited on p. 45)
DOI: 10.1016/0021-9991(85)90061-0

[Mal99] A. M. Malek, S. L. Alper and S. Izumo. 'Hemodynamic shear stress and its role in atherosclerosis'. In: *The Journal of the American Medical Association* 282.21 (Dec. 1999), pp. 2035–2042. (Cited on p. 2)
DOI: 10.1001/jama.282.21.2035

[Mar04] I. Marshall, S. Zhao, P. Papathanasopoulou, P. Hoskins and X. Y. Xu. 'MRI and CFD studies of pulsatile flow in healthy and stenosed carotid bifurcation models'. In: *J. Biomech.* 37.5 (2004), pp. 679–687. (Cited on p. 50)
DOI: 10.1016/j.jbiomech.2003.09.032

[Mar12] M. Markl, A. Frydrychowicz, S. Kozerke, M. Hope and O. Wieben. '4D flow MRI'. In: *Magn. Reson. Im.* 36.5 (2012), pp. 1015–1036. (Cited on pp. 3, 19, 49, 52)
DOI: 10.1002/jmri.23556

[Mic03] C. Michiels. 'Endothelial cell functions'. In: *J. Cell. Physiol.* 196.3 (2003), pp. 430–443. (Cited on p. 1)
DOI: 10.1002/jcp.10333

[Miy17] S. Miyazaki, K. Itatani, T. Furusawa, T. Nishino, M. Sugiyama, Y. Takehara and S. Yasukochi. 'Validation of numerical simulation methods in aortic arch using 4D Flow MRI'. In: *Heart and Vessels* 32.8 (2017), pp. 1032–1044. (Cited on p. 50)
DOI: 10.1007/s00380-017-0979-2

[Mor13] U. Morbiducci, R. Ponzini, D. Gallo, C. Bignardi and G. Rizzo. 'Inflow boundary conditions for image-based computational hemodynamics: impact of idealized versus measured velocity profiles in the human aorta'. In: *J. Biomech.* 46.1 (2013), pp. 102–109. (Cited on p. 4)
DOI: 10.1016/j.jbiomech.2012.10.012

[Mus14] J. Muscat. *Functional Analysis: An Introduction to Metric Spaces, Hilbert Spaces, and Banach Algebras*. Springer, 2014. ISBN: 9783319067292. (Cited on p. 43)

[Pan17] S. Pant, C. Corsini, C. Baker, T.-Y. Hsia, G. Pennati and I. E. Vignon-Clementel. 'Inverse problems in reduced order models of cardiovascular haemodynamics: aspects of data assimilation and heart rate variability'. In: *J. R. Soc. Interface* 14.126 (2017), p. 20160513. (Cited on p. 8)
DOI: 10.1098/rsif.2016.0513

[Pap03] P. Papathanasopoulou, S. Zhao, U. Köhler, M. B. Robertson, Q. Long, P. Hoskins, X. Y. Xu and I. Marshall. 'MRI measurement of time-resolved wall shear stress vectors in a carotid bifurcation model, and comparison with CFD predictions'. In: *J. Magn. Reson. Imaging* 17.2 (2003), pp. 153–162. (Cited on p. 50)
DOI: 10.1002/jmri.10243

[Pat72] S. V. Patankar and D. B. Spalding. 'A Calculation Procedure for Heat, Mass and Momentum Transfer in Three-Dimensional Parabolic Flows'. In: *J. Heat Mass Transfer* 15 (1972), pp. 1787–1806. (Cited on pp. 15, 60)
DOI: 10.1016/0017-9310(72)90054-3

[Pel91] N. J. Pelc, R. J. Herfkens, A. Shimakawa and D. R. Enzmann. 'Phase contrast cine magnetic resonance imaging'. In: *Magn. Reson. Q.* 7.4 (1991), pp. 229–254. (Cited on p. 22)

[Pir17] S. Pirola, Z. Cheng, O. A. Jarral, D. P. O'Regan, J. R. Pepper, T. Athanasiou and X. Y. Xu. 'On the choice of outlet boundary conditions for patient-specific analysis of aortic flow using computational fluid dynamics'. In: *J. Biomech.* 60.1 (2017), pp. 15–21. (Cited on p. 4)
DOI: 10.1016/j.jbiomech.2017.06.005

[Raf07] M. Raffel, C. E. Willert, S. T. Wereley and J. Kompenhans. 'Post-Processing of PIV Data'. In: *Particle Image Velocimetry: A Practical Guide*. Springer Berlin Heidelberg, 2007, pp. 177–208. (Cited on p. 18)
DOI: 10.1007/978-3-540-72308-0_6

[Ray08] V. L. Rayz, L. Boussel, G. Acevedo-Bolton, A. J. Martin, W. L. Young, M. T. Lawton, R. Higashida and D. Saloner. 'Numerical Simulations of Flow in Cerebral Aneurysms: Comparison of CFD Results and In Vivo MRI Measurements'. In: *ASME. J. Biomech. Eng.* 130.5 (2008), pp. 40–65. (Cited on p. 50)
DOI: 10.1115/1.2970056

[Ren06] R. S. Reneman, T. Arts and A. P. G. Hoeks. 'Wall shear stress–an important determinant of endothelial cell function and structure–in the arterial system in vivo. Discrepancies with theory'. In: *J. Vasc. Res.* 43.3 (2006), pp. 251–269. (Cited on pp. 2, 49)
DOI: 10.1159/000091648

[Rus02] H. Rusche. 'Computational Fluid Dynamics of Dispersed Two-Phase Flows at High Phase Fractions'. PhD thesis. Imperial College of Science, Technology & Medicine, 2002. (Cited on p. 61)

[Sax01] K. Saxe. *Beginning Functional Analysis*. Springer New York, 2001. ISBN: 9780387952246. (Cited on p. 43)

[Sch16] S. Schmitter, S. Schnell, K. Uğurbil, M. Markl and P. F. Van de Moortele. 'Towards high-resolution 4D flow MRI in the human aorta using kt-GRAPPA and B1+ shimming at 7 tesla'. In: *J. Magn. Reson. Imaging* 44.2 (2016), pp. 486–499. (Cited on p. 34)
DOI: 10.1002/jmri.25164

[Sha00] A. M. Shaaban and A. J. Duerinckx. 'Wall shear stress and early atherosclerosis: a review'. In: *AJR Am. J. Roentgenol.* 174.6 (2000), pp. 1657–1665. (Cited on p. 3)
DOI: 10.2214/ajr.174.6.1741657

[Sto72] A. Stokes. 'On the approximation of nonlinear oscillations'. In: *J. Differ. Equ.* 12.3 (1972), pp. 535–558. (Cited on p. 55)
DOI: 10.1016/0022-0396(72)90024-1

[Sun16] Y. Sun, J. Ma, B. Li and Z. Guo. 'Predication of nonlinear heat transfer in a convective-radiative fin with temperature-dependent properties by the collocation spectral method'. In: *Numer. Heat Transfer, Part B* 69.1 (2016), pp. 68–83. (Cited on p. 45)
DOI: 10.1080/10407782.2015.1081043

[Tex65] Meyer Texon, Anthony M. Imparato and Milton Helpern. 'The role of vascular dynamics in the development of atherosclerosis'. In: *The Journal of the American Medical Association* 194.11 (Dec. 1965), pp. 1226–1230. (Cited on p. 2)
DOI: 10.1001/jama.1965.0309024006001

[Tha95] C. Thang, D. D. Blatter and D. L. Parker. 'Correction of partial-volume effects in phase-contrast flow measurements'. In: *J. Magn. Reson. Imaging* 5.2 (1995), pp. 175–180. (Cited on pp. 3, 49)
DOI: 10.1002/jmri.1880050212

[Tia16] J. Tiago, T. Guerra and A. Sequeira. 'A velocity tracking approach for the data assimilation problem in blood flow simulations'. In: *Int. J. Numer. Method Biomed. Eng.* 33.10 (2016), e2856. (Cited on p. 8)
DOI: 10.1002/cnm.2856

[Vec16] A. de Vecchi, A. Gomez, K. Pushparajah, T. Schaeffter, G. P. Penney J. M. Simpson R. Razavi, N. P. Smith and D. A. Nordsletten. 'A novel methodology for personalized simulations of ventricular hemodynamics from noninvasive imaging data'. In: *Comput. Med. Imaging Graph.* 51.1 (2016), pp. 20–31. (Cited on p. 34)
DOI: 10.1016/j.compmedimag.2016.03.004

[Vor05] D. A. Vorp and J. P. Vande Geest. 'Biomechanical determinants of abdominal aortic aneurysm rupture'. In: *Arterioscler Thromb Vasc Biol.* 25.8 (2005), pp. 1558–1566. (Cited on p. 2)
DOI: 10.1161/01.ATV.0000174129.77391.55

[Vor96] D. A. Vorp, M. L. Raghavan, S. C. Muluk, M. S. Makaroun, D. L. Steed, R. Shapiro and M. W. Webster. 'Wall strength and stiffness of aneurysmal and nonaneurysmal abdominal aorta'. In: *Ann. N. Y. Acad. Sci.* 800.1 (1996), pp. 274–276. (Cited on p. 2)
DOI: 10.1111/j.1749-6632.1996.tb33330.x

[Wak09] A. K. Wake, J. N. Oshinski, A. R. Tannenbaum and D. P. Giddens. 'Choice of in vivo versus idealized velocity boundary conditions influences physiologically relevant flow patterns in a subject-specific simulation of flow in the human carotid bifurcation'. In: *J. Biomech. Eng.* 131.2 (2009). (Cited on p. 50)
DOI: 10.1115/1.3005157

[Wal93] P. L. Walpola, A. I. Gotlieb and B. L. Langille. 'Monocyte adhesion and changes in endothelial cell number, morphology, and F-actin distribution elicited by low shear stress in vivo'. In: *Am J Pathol.* 142.5 (1993), pp. 1392–1400. (Cited on p. 2)

[Wan09] Q. Wang, P. Moin and G. Iaccarino. 'Minimal Repetition Dynamic Checkpointing Algorithm for Unsteady Adjoint Calculation'. In: *SIAM J. Sci. Comput.* 31.4 (2009), pp. 2549–2567. (Cited on p. 69)
DOI: 10.1137/080727890

[Wel98] H. G. Weller, G. Tabor, H. Jasak and C. Fureby. 'A Tensorial Approach to Computational Continuum Mechanics Using Object-oriented Techniques'. In: *Comput. Phys.* 12.6 (Nov. 1998), pp. 620–631. (Cited on pp. 16, 20, 60)
DOI: 10.1063/1.168744

[Wes05] J. Westerweel and F. Scarano. 'Universal outlier detection for PIV data'. In: *Exp. Fluids* 39.6 (2005), pp. 1096–1100. (Cited on pp. 17, 18)
DOI: 10.1007/s00348-005-0016-6

[Yos90] Y. Yoshida, W. Sue, M. Okano, T. Oyama, T. Yamane and M. Mitsumata. 'The effects of augmented hemodynamic forces on the progression and topography of atherosclerotic plaques'. In: *Annals of the New York Academy of Sciences* 598.1 (Aug. 1990), pp. 256–273. (Cited on p. 2)
DOI: 10.1111/j.1749-6632.1990.tb42298.x

[Zan91] T. Zand, G. Majno, J. J. Nunnari, A. H. Hoffman, B. J. Savilonis, B. MacWilliams and I. Joris. 'Lipid deposition and intimal stress and strain. A study in rats with aortic stenosis'. In: *Am J Pathol.* 139.1 (1991), pp. 101–113. (Cited on p. 2)

[Zar87] C. K. Zarins, M. A. Zatina, D. P. Giddens, D. N. Ku and S. Glagov. 'Shear stress regulation of artery lumen diameter in experimental atherogenesis'. In: *J Vasc Surg.* 5.3 (1987), pp. 413–420. (Cited on p. 2)
DOI: 10.1016/0741-5214(87)90048-6

[Zha03] S. Z. Zhao, P. Papathanasopoulou, Q. Long, I. Marshall and X. Y. Xu. 'Comparative Study of Magnetic Resonance Imaging and Image-Based Computational Fluid Dynamics for Quantification of Pulsatile Flow in a Carotid Bifurcation Phantom'. In: *Ann. Biomed. Eng.* 31.8 (2003), pp. 962–971. (Cited on p. 50)
DOI: 10.1114/1.1590664